Optical Properties and Structural Characterization of Ceramic Crystals, Pellets, and Laser-Ablation-Deposited Thin Films

by

Mona P. Moret

Thesis submitted to the Faculty of the

Virginia Polytechnic Institute and State University

in partial fulfillment of the requirements for the degree of

MASTER OF SCIENCE

IN

APPLIED PHYSICS

APPROVED:

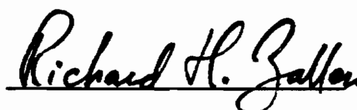

Richard H. Zallen, Chair

Seshu B. Desu

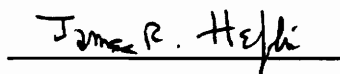

James R. Heflin

July, 1996

Blacksburg, Virginia

Key words: Strontium Bismuth Tantalate, Titanium Dioxide, Laser Ablation, Raman, Infrared, Thin Films

c.2

LD
5655
V855
1996
M674
c.2

Optical Properties and Structural Characterization of Ceramic Crystals, Pellets, and Laser-Ablation-Deposited Thin Films.

by

Mona P. Moret

[Richard Zallen, Chairman]

Physics Department

(ABSTRACT)

This study was divided into two main parts as there were two kind of films studied. The method of deposition, pulsed laser ablation, was common to both $SrBi_2Ta_2O_9$ and TiO_2 films. The methods of investigations were also the same.

There is an important race for the development of a practical ferroelectric memory. Among ferroelectrics that have attracted attention are the novel compounds with the Aurivillius layered structure. Ferroelectric films of $SrBi_2Ta_2O_9$, seem to have promising properties, low fatigue and good hysteresis.
In this thesis, structure and crystal vibrations in the films were investigated with Raman scattering, infrared absorption, and x-ray diffraction. Similar studies were carried out on powders and crystals of these materials also. The results obtained prove that the films have the orthorhombic $SrBi_2Ta_2O_9$ structure, and the Raman and IR measurements (the first reported for SBT films) are demonstrated to provide valuable tools for optimizing the deposition process.

TiO_2 is another important material in the domain of thin films. This work was undertaken to study its deposition with laser ablation.

The TiO_2 films deposited are very unusual; we discovered that they contain the rare brookite phase. This is the first time that brookite has been obtained in laser-ablation-deposited films. This opens up a new area in thin film development with new potential applications. The absorption edge of brookite was measured, using natural crystals. The optical bandgap was found to be lower than the bandgaps of the rutile and anatase forms of TiO_2, in contradiction of a recent theoretical calculation.

ACKNOWLEDGMENTS

During my research, I gained lots of experience and also among many things really enjoyed my work. This is indeed due to the persons that I had the opportunity to meet and to work with.

The first one is Prof. Richard Zallen, who was brave enough to accept me as a MS student. He gave me the opportunity to work with a very varied number of techniques and always helped me and encouraged me in my research. I thank him for his useful guidance for those first years of research.

Prof. Seshu B. Desu was always there to share his great expertise in thin films and guide me. I thank him also for providing funding, some of which permitted me to participate to the 1996 APS March Meeting.

I am grateful to Reinaldo Gonzalez for patiently helping me in the lab with all the equipment and for getting me started with my experiments.

I thank Dilip Vijay for the SBT films, and for sharing his expertise about them and for being a connection to the materials community at Virginia Tech.

I thank Prof. R. Bodnar [Geology] for making available his Dilor XY micro-Raman instrument and Frank Harrison for training me in its use.

I am also indebted to Profs. R.E. Newnham [Penn State] and S.C. Moss [U. of Houston] for providing respectively crystals of SBT and brookite TiO_2, to Prof. J.R. Heflin for serving on my committee, and to Prof. G.V. Gibbs for generously spending time with me on crystal structure analysis.

I also acknowledge the Physics Dept. for the Teaching Assistantship received during those two years.

I would also like to thank some other persons for more simple human reasons: Prof. Williams for his friendly welcome, and his help to get me started smoothly at Virginia Tech. Chris Thomas and Barbara Day for their constant cheerfulness and help with all the paperwork.

Without my friends, it would have not been the same. They helped me to maintain an equilibrium between work and leisure. I am indebted to Alex, Rollin, Kristen, and Charles. A very special thanks goes to Henrik.

My family has also been of a great support; I am grateful for all their understanding and their presence.

MERCI A TOUS

TABLE OF CONTENTS

	Page
Acknowledgments	iv
Table of Contents	vi
List of Figures	ix
List of Tables	xii
Chapter 1: Deposition Technique and Instrumentation.	1
1.1. Pulsed Laser Deposition.	1
1.1.1. Introduction.	1
1.1.2. Method used.	2
1.1.3. Note.	4
1.2. Optical Techniques.	5
1.2.1. Introduction.	5
1.2.2. Raman.	5
1.2.3. Infrared.	16
1.2.4. UV-Visible.	19
1.3. X-ray Diffraction.	22
Chapter 2: $SrBi_2Ta_2O_9$ Films Made by Pulse Laser Deposition.	35
2.1. Why $SrBi_2Ta_2O_9$ Thin Films?	35
2.2. Samples.	38
2.2.1. Crystals.	38
2.2.2. Pellets.	38
2.2.3. Films.	39
2.3. $A2_1am$ Space Group on Pellet and PLD $SrBi_2Ta_2O_9$ Films: Confirmation by X-ray.	40

2.4. Raman Verdict. 45
2.4.1. Pellet and Crystals Specimens - Comparison with Literature. 45
2.4.2. Tentative Assignment of Vibrational Modes. 49
2.4.3. Pulsed-Laser-Deposited Thin Films. 51
2.4.4. Raman and X-ray Measurements Combined: Evidence for a Lower Crystalline/Amorphous Ratio for PLD $SrBi_2Ta_2O_9$ Films Grown at Substrate Temperature Below 650 C. 53
2.5. LO and TO Modes from Infrared Measurements. 55
2.5.1. Infrared Measurements on the Pellet and the Crystal. 55
2.5.2. Crystal Infrared Reflectivity Data Fitted with Factorized Form of the Dielectric Function. 56
2.5.3. Infrared Measurements on the PLD SBT Films. 59
2.5.4. Infrared Measurements on Other Aurivillius Compounds. 62
2.5.5. Conclusions on Infrared Characterization. 63
2.6. Summary for PLD $SrBi_2Ta_2O_9$ Films and Possible Future Work. 64

Chapter 3: TiO_2 Films made by Pulse Laser Deposition. 98
3.1. Background on TiO_2. 98
3.1.1. Polymorphism. 100
3.1.2. Applications. 100
3.1.3. This study. 101
3.2. Observation for the First Time of the Brookite Phase in PLD Titania Thin Films. 102
3.2.1. Brookite Identification by X-ray and Raman Measurements. 102

3.2.2. Brookite in PLD films: Reproducibility? Substrate Dependence? Presence of New Phases? 108
3.2.3. Brookite: Film Homogeneity and Estimation of the Different Phases Present. 112
3.3 Measurements of the Optical Bandgap of Brookite 115
3.3.1. Thickness Estimation. 116
3.3.2. Bandgap Measurements from UV-Visible Optical Absorption. 119
3.4. Summary for PLD Titania Films and Future Directions. 122

References **143**

Appendix 1: Peaks Listing of the SBT Simulated X-ray Pattern. Input/Output Xtalpow. **148**
Appendix 2: Peaks Listing of Rutile, Anatase, and Brookite Simulated X-ray Patterns. Input/Output Xtalpow. **152**

Vita **157**

LIST OF FIGURES

Fig. 1.1 Schematic of the pulsed laser ablation system.

Fig. 1.2 Schematic of the SPEX 1403.

Fig. 1.3 Geometries used in Raman.

(a) Backscattering (Perkowitz, 1993).

(b) Near Backscattering (Holtz, 1987).

Fig. 1.4 Schematic of the foremonochromator for Dilor XY.

Fig. 1.5 Schematic of a Michelson interferometer.

Fig. 1.6 Schematic of the FTIR Bomem DA 3.02.

Fig. 1.7 Infrared spectra of three types of sample configurations. The sample is taken to have the idealized one-oscillator-mode structure given at the bottom of the figure with one TO frequency, one LO frequency, and a constant damping factor, (Palik, 1985).

Fig. 1.8 Schematic diagram of the UV-visible set-up, (Feng, 1989).

Fig. 1.9 Bragg reflection, (Burns, 1985).

(a) From a family of lattice planes.

(b) Bragg angle.

Fig. 1.10

(a) Bragg-Brentano configuration for x-ray measurements.

(b) Grazing incidence configuration for x-ray measurements.

(c) Schematic showing the receiving slits used in the grazing incidence configuration.

Fig. 2.1 $BaTiO_3$ structure.

Fig. 2.2 X-ray patterns of $SrBi_2Ta_2O_9$ (SBT) thin films in normal configuration.

Fig. 2.3 X-ray patterns of SBT and SBN powders at normal incidence.

Fig. 2.4 Schematic of the SBT structure using Newnham atom positions.

Fig. 2.5 Comparison of generated powder pattern with measured XRD patterns of SBT pellet and of SBT crystal.

Fig. 2.6 X-ray powder patterns of SBT crystals.

Fig. 2.7 Comparison of SBT powder at normal and grazing incidence 2°.

Fig. 2.8

(a) Near-grazing x-ray data on SBT thin film 750 C substrate temperature, 2nd set for various angles of incidence.

(b) Near-grazing x-ray data on SBT thin film 550 C substrate temperature, 2nd set for various angles of incidence.

(c) Near-grazing x-ray data on SBT thin film 750 C substrate temperature, 1st set for various angles of incidence.

(d) Near-grazing x-ray data on SBT thin film 500 C substrate temperature, 1st set for various angles of incidence.

Fig. 2.9 Pole figure on the 500 C 1st set SBT thin film at 29°.

Fig. 2.10 Raman spectra of the SBT pellet and the SBT crystal.

Fig. 2.11 Reported Raman spectra for n=1,2,3, and 4 Aurivillius phases for powder specimens at ambient temperature (Graves et al., 1995).

Fig. 2.12

(a)Raman spectra of the tantalum-compounds.

(b)Raman spectra of the niobium-compounds.

Fig. 2.13

(a)Raman spectra of the tantalum-compounds at low energy.

(b)Raman spectra of the niobium-compounds at low energy.

Fig. 2.14 Raman spectra of the PLD $SrBi_2Ta_2O_9$ films.

Fig. 2.15 Infrared reflectivity at normal incidence on SBT pellet and SBT crystal.

Fig. 2.16 Infrared reflectivity at grazing incidence on the SBT 1st set of films.

Fig. 2.17 Infrared reflectivity at grazing incidence on the SBT 2nd set of films.

Fig. 2.18 Factorized form of the dielectric function fit of the SBT crystal infrared reflectivity.

Fig. 2.19

(a) Dielectric constants extracted from the fit.

(b) Refractive index and extinction coefficient extracted from the fit.

Fig. 2.20 Simulation of the pellet reflectivity data using the results from crystal fit.

Fig. 2.21 Simulation of the film reflectivity data using the results from crystal fit.

Fig. 2.22

(a)Infrared reflectivity of the tantalum-compounds family.

(b)Infrared reflectivity of the niobium-compounds family.

Fig. 2.23 Infrared reflectivity of the films, for various bismuth concentrations.

Fig. 2.24 Infrared Reflectivity at near-grazing incidence on PLD SBT film and SBT pellet, and PLD $SrBi_2Ta_{1.6}Nb_{0.4}O_9$ film and $SrBi_2Ta_{1.6}Nb_{0.4}O_9$ pellet.

Fig. 3.1 Structure of rutile generated in the 100 plane with Xtaldraw.

Fig. 3.2 Structure of anatase generated in the 010 plane with Xtadraw.

Fig. 3.3 Structure of brookite generated in the 010 plane with Xtaldraw.

Fig. 3.4 Comparison between the x-ray powder patterns measured and simulated for the TiO_2 crystal phases.

Fig. 3.5 X-ray powder pattern of the first four TiO_2 films.

Fig. 3.6 X-ray powder pattern of the TiO_2 crystal phases and Sample 4 [S4].

Fig. 3.7 Raman data from the TiO_2 crystal phases and Sample 4.

Fig. 3.8 Raman data obtained on the first four TiO_2 samples.

Fig. 3.9 X-ray powder patterns obtained on the four film-samples deposited in the exact same conditions as S4.

Fig. 3.10 Raman data on the four film-samples deposited in the exact same conditions as S4.

Fig. 3.11 Raman data obtained at different locations on the surface of the film S6.

Fig. 3.12 Raman data obtained at different locations on the surface of the film S7.

Fig. 3.13 Raman data obtained at different locations on the surface of the film S10.

Fig. 3.14 Near-grazing x-ray pattern of S4 for various angles of incidence.

Fig. 3.15 Near-grazing x-ray pattern of S5 for various angles of incidence.

Fig. 3.16 Near-grazing x-ray pattern of S8 for various angles of incidence.

Fig. 3.17 Reflectivity measurements on S4 in the UV-visible region.

Fig. 3.18 Transmission measurements of the PLD TiO_2 films and brookite crystals.

Fig. 3.19 Absorption coefficients for rutile, anatase, and brookite.

LIST OF TABLES

Table 1.1 Regions of the electromagnetic spectrum.

Table 1.2 Semiconductor properties which can be characterized by optical methods such as photoluminescence [PL], Raman, or infrared (IR), (Perkowitz, 1993).

Table 1.3 Table comparing the Raman instruments used.

Table 1.4 Laser wavelengths (in vacuo), photon energies, frequencies, and maximum outputs powers for Coherent lasers, (Holtz, 1987).

Table 1.5 Elements used in the interferometer Bomem DA3.02.

Table 1.6 IR-near -UV spectrometer components, (Feng, 1989).

Table 2.1 List of the thin-film samples

Table 2.2 Comparison of the x-ray diffraction peaks present in the patterns observed for the thin films and the pellets.

Table 2.3 Raman lines in our powder and crystal specimens compared with data in literature (Graves et aL., 1995).

Table 2.4 Comparison with our $BaBi_2Nb_2O_9$ Raman results with those of (Graves et al., 1995).

Table 2.5 Raman lines detected at low frequencies in SBN and SBT compared to reported measurements (Liu et al., 1994).

Table 2.6 Raman peaks detected in the SBT films.

Table 2.7 The infrared reflectivity of the SBT crystal, fitted with the factorized form of the dielectric function.

Table 2.8 Infrared frequencies in the crystal and in four films of the second set.

Table 3.1 The three crystal structures of TiO_2.

Table 3.2 Atomic positions used to generate plot of the structures (Wyckoff, 1963).

Table 3.3 Deposition parameters for the first four TiO_2 films.

Table 3.4 Raman lines [cm-1] of: rutile, anatase, and brookite.

Table 3.5 Raman lines (cm-1) appearing in the first four TiO_2 films.

Table 3.6 List of the TiO_2 samples deposited.

Table 3.7 Reported data on the rutile, anatase, and brookite bandgaps from (Mo et al., 1995).

Table 3.8 List of the estimated thicknesses for S4 from reflectivity measurements.

Table 3.9 List of the estimated thicknesses for S8 and S10 from transmission measurements.

Chapter 1: Deposition Techniques and Instrumentation

1.1 Pulsed Laser Deposition

1.1.1. Introduction

This deposition method was started in 1962, the landmark of the appearance of the ruby laser. In 1965, the first report on laser deposition of thin films was published, but it is not until the eighties that it was commonly used, as the sputtering method gave films of better quality. The later development was, in part, due to materials science and engineering needs to investigate superconductor thin films. It is the work on the high-temperature superconductor thin films which led to the wide use of pulsed laser deposition (PLD); the high-Tc work proved that complex multi-element films can be reproduced under appropriate conditions of laser energy, density, and deposition angle relative to the target surface normal. Since then, electro-optic and ferroelectric materials have also been deposited by PLD.

Descriptions of the processes involved in laser ablation can be found in (Miller, 1994). Simply stated, the fundamental process is electron excitation by absorption of a photon. The interaction can be different in character depending on the material (metal, semiconductor, or insulator), but leads to the same overall effects: melting, evaporation, and plasma formation. The principal mechanism involved is called "primary interaction": the interaction of the photons with the surface. This creates electron-hole pairs and heats the free electrons. Laser ablation takes place when the initial electronic excitation is converted into driving energy for nuclear motion. Then follows the ejection of atoms, ions, and molecules from the surface. The rate of this energy conversion depends on the electron-lattice interactions.

1.1.2. Method used

The deposition was done with a Lambda Physik LPX excimer laser using KrF radiation (248 nm) which was focused onto a rotating target of the starting material with a 50-cm focal length UV graded plano convex lens. The beam was incident on the target at an angle of 45° and the target was rotated at 10-13 rpm [Fig 1.1]. The evaporated material is ejected in the forward direction under suitable background pressures of oxygen and suitable temperature. The common way of proceeding for the preparation and the deposition of a film by laser ablation for this study is as follows.

- **Preparation of a target pellet**

All the utensils are cleaned with methanol. Different masses of the different necessary powders [usually commercially available powders] are measured to yield the desired stoichiometry. They are ball ground together with some Methacel [commercial binder which acts with a few drops of water as a kind of glue].

A circular die of the size of the target holder is cleaned with some vaseline, to allow later extraction of the pellet after compression. It is then pressed for roughly 3 min at 5000 pounds. The pellet also needs to be heated to reach sintering [contact established between the grains in the pellet to reduce the total surface energy]. The time it takes to reach sintering is typically around 7 h. It is highly recommended to use sintered pellets with the laser ablation process, in order to avoid the incorporation of small particles or clusters during the deposition. Using a non-sintered pellet would increase the surface roughness and might also degrade the properties of the films. For the same reasons, the target is polished before being used.

- **Pre-ablation of the pellet**

The pellet is first entered in the chamber, as it needs to be pre-ablated. We used 1800 pulses at 10 pulses/sec. This is to avoid any kind of transition when starting the deposition on the substrate. It is also a good time to adjust the laser on the edge of the pellet. The deposition parameters depending on the laser are controlled from a computer which will turn on once the laser is turned on.
The parameters are the following:

- Energy of the beam
- Pulse (frequency)
- Exposure time (number of pulses)

There are three others parameters which can influence the deposition and which are changed externally:

- substrate-target distance: adjusted manually.
- temperature of the substrate: preprogrammed on the controller, as well as the cooling of the sample. The program is adjusted depending on the parameters chosen for the laser.
- O_2 pressure in the chamber: The main role of this factor is to ensure a stoichiometric film, and it is commonly kept at 200 mTorr. It enhances the deposition of oxides. Without the additional O_2, the materials deposited might have a lack of oxygen.

- **Substrate**

Once the substrate is chosen, a piece of roughly 1.5×3 cm^2 is cut. If the piece is larger it might extend beyond the plume generated by the laser, and no material will be deposited on the edges. The substrate is cleaned with acetone and isopropanol. A uniform layer of silver paint is put on the substrate holder and the substrate glued on top of it. It will ensure that the substrate stands in the vertical position during the deposition. No evidence of contamination by the silver paint has been noticed but efforts to design a new holder have been attempted in the lab by other students. Then the substrate holder is preheated before being carefully entered in the chamber. [Carefully, as the pressure difference might unglue the substrate and cause it to fall]. Once the pressure is obtained, the deposition can start.

Up to now no mention has been made about the rotation of the holders. They are rotated anticlockwise. The rotation of the pellet on the long pole might also affect the deposition, and there are vibrations which need to be checked regularly.

1.1.3. Note

It should be noted that it is very difficult to produce identical film samples. The energy of the beam fluctuates. The energy of the beam is indicative. If the KrF gas has just been reloaded, 600 mJ will not correspond to 600 mJ after a week of use. Once hitting the pellet, the beam might have lost a certain percentage of its initial energy. This is then the advantage of focusing the beam [Fig. 1.1] on the pellet to regain some energy lost during the path and through the windows.

1.2 Optical Techniques

1.2.1 Introduction

The following techniques which were used are non-destructive and complementary. They cover a wide part of the electromagnetic spectrum and intensity is measured versus wavelength. The different regions are summarized in Table 1.1 as different units are going to be used to display data.

The following techniques are materials oriented and are often encountered in characterization work. Table 1.2 summarizes the kind of information which can be extracted from these techniques. It is worth noting that these are non-destructive techniques, in-situ measurements are possible, and the measurement times are relatively short.

1.2.2. Raman

Raman scattering can be used for solid-state characterization, and a quantitative determination of each crystalline phase present can be done using the relative intensities among the lines. Stress information can also be extracted for thin films of some materials (such as semiconductors), and also microstructural parameters [grain size and disorder] using the lineshapes. In this work, Raman has mainly been used for phase characterization, especially for the TiO_2 films, in parallel with the x-ray measurements.

Table 1.1 **Regions of the electromagnetic spectrum.**

	X-Rays	UV	Visible	Near Infrared	Mid Infrared	FarInfared
Wavelength λ	10 Å	400 nm	750 nm	3 μm	30 μm	
Frequency ν [Hz]	$3\ 10^{17}$	$7.5\ 10^{14}$	$4\ 10^{14}$	10^{14}	10^{13}	
Wavenumber $\bar{\nu} = \frac{1}{\lambda}$ [cm-1]	10^{7}	$2.5\ 10^{4}$	$1.3\ 10^{4}$	$3.3\ 10^{3}$	$3.3\ 10^{2}$	
Energy [eV]	$1.2\ 10^{3}$	3.1	1.6	0.4	0.04	

Table 1.2 Semiconductor properties which can be characterized by optical methods such as photoluminescence (PL), Raman, or infrared (IR), (Perkowitz, 1993).

Semiconductor property	Optical method		
	PL	Raman	IR
Band			
Gap	•		•
Effective mass			•
Band offset	•		
Free carrier			
Concentration		•	•
Mobility		•	•
Scattering time		•	•
Resistivity		•	•
Lattice			
Alloy composition	•	•	•
Orientation		•	
Crystallinity	•	•	
Stress	•	•	
Impurity and defect			
Presence and type	•	•	•
Concentration	•	•	•
Microstrucsure			
Layer thickness			•
Surface behavior	•	•	
Interface behavior	•	•	•
Layer-by-layer behavior			•
Other			
Homogeneity mapping	•	•	•

* A bullet at the intersection of a method (column) and a property (row) indicates that method is especially useful to measure that property. Some measurements require auxiliary information. Where more than one method is available. other factors may determine the choice: see text. The discussions and case studies in this book present and illustrate most of the applications shown.

a) Theory.

The interaction between electromagnetic radiation and bound electrons results in a scattering process, because the time-varying field of the incident radiation can induce a dipole moment in the material. That is why Raman is different in character from infrared absorption or neutron diffraction, as the resulting inelastic scattering involves a modulation of the electronic polarizability caused by the atom displacements.
If there is absorption (or annihilation) of a phonon, it is called an anti-Stokes process; on the other hand if there is the emission (creation) of a phonon, it is a Stokes process. The latter is the stronger process since the former depends on the number of phonon available.

Raman spectroscopy determines the frequencies of the $k\cong0$ phonons. [The wavevector of the electromagnetic radiation is small, therefore only $k\cong0$ phonons have the proper k values for conservation of crystal momentum]. This is a weak phenomenon [five or six orders of magnitude weaker than Rayleigh scattering, and 10^{-6} to 10^{-8} the intensity of the incident radiation if the power ranges from 10^{-1} W to 1 W].

Find below the usual classical picture descriptive of the phenomena (Burns, 1985; Perkovitz, 1993; Hummel, 1995). The following model applies for a one-phonon process, but events can occur in which two phonons are emitted, and belongs to a higher order process [second order Raman process].

ω_i, ω_s, k_i, k_s represent the frequencies and the wave vectors of the incident and scattered light respectively. The time dependence of the incident light being given by

$$E(t)_i = E_i \cos(\omega_i t) \qquad (1.2.1)$$

From the classical macroscopic theory the polarization is given by

$$P(\omega,t) = \alpha(\omega,t)\times E(\omega,t) \qquad (1.2.2)$$

where $\alpha(w)$ is the polarizability due to the solid [sample].

This term can be simply expanded in Taylor's series:

$$\alpha(\omega) = \alpha_0 + (\frac{\partial \alpha}{\partial u})_0 \times u + (\frac{\partial^2 \alpha}{\partial u^2})_0 \times \frac{u^2}{2} + ... \qquad (1.2.3)$$

$$\equiv \alpha_0 + \alpha_1 + \alpha_2 ...$$

u is the atom's displacement from equilibrium due to the phonons. The displacement has also a time variation given by

$$u = u_0 \cos(\omega_0 t) \qquad (1.2.4)$$

The polarization is time varying and can be considered as a radiating system, and is a source of electromagnetic waves. The total power radiated is directly proportional to the square of the induced dipole moment (Jackson, 1975), section 9.2.

$$P = \frac{ck^4}{3} \times |p|^2 \qquad (1.2.5)$$

P being the total power, c the speed of light, p the electric dipole moment, and k is the wavenumber.

The first term in the expansion (1.2.3) of the polarizability gives a contribution that is not shifted in frequency with respect to the incident light and represents the Rayleigh scattering. But the higher order terms are shifted in frequency, giving rise to inelastic scattering. α_1 gives rise to the one-phonon process and α_2 gives rise to the two phonon process mentioned previously. Let's only consider the resulting polarization due to α_1.

$$P_1(\omega) = (\alpha_1 u_0 E_i)[\cos(\omega_i t)][\cos(\omega_0 t)] \qquad (1.2.6)$$

$$= (\frac{\alpha_1 u_0 E_i}{2})[\cos(\omega_i + \omega_0)t + \cos(\omega_i - \omega_0)t] \qquad (1.2.7)$$

The first term and the second term in 1.2.7 represents respectively the anti-Stokes and the Stokes processes.

What is analyzed in the Raman spectra is often referred as the normal mode analysis. Normal modes specify the types of atomic vibrations occurring in the crystal. Some normal modes can couple directly with electromagnetic waves and these lattice vibrations result in absorption lines in the infrared region. Other normal modes give rise to inelastic scattering producing Raman lines. The analysis is achieved by group theory, applied to crystals, (Burns, 1978).

Thirty-two crystallographic point groups have been developed by combining point symmetry elements together without redundancy. Point symmetry operation implies that the operation is performed with respect to a point which will stay fixed during the operation. There are five elements in this group: Identity, rotation, inversion, reflection across a plane, improper rotation. Their description can be found in (Burns, 1978).

The notion of space group is necessary to describe an entire crystal. The point group is not sufficient to define symmetry operations in 3 dimensions. Space groups have been defined by combining point groups and the Bravais lattices [combination of crystal systems forming 14 distinct lattices]. The combination forms a group according to the mathematical definition; it is defined by a set of geometrical operations that can take a 3-D object into itself. There are three additional operations in the space group compare to the point group: translation, screw operation, and the glide plane.

One selection rule is due to the presence of a center of symmetry. If there is a center of symmetry in the space group of the crystal, phonons that are infrared (IR) active cannot be Raman active and vice-versa; this is a mutual exclusion principle. In non-centrosymmetric crystals, modes may be simultaneously IR and Raman active. This analysis is more or less complicated depending on the number of atoms in the unit cells. A direct example is seen for $SrBi_2Ta_2O_9$, where the large number of atoms per unit cell implies a substantial complication.

b) Instrumentation.

Due to the small size of the frequency shift versus the visible light, the use of sharply defined monochromatic incident light is necessary in Raman scattering. Lasers are being used extensively in this field.

The Raman spectra (Stokes) were obtained with two instruments, which are in principle similar. The geometry of the spectrometers and the detection is different. Their advantages/disadvantages have been put in parallel in Table 1.3, and will illustrate the use of one instrument or the other depending on the sample. Below the two instruments are described separately in a bit more detail.

Table 1.3 **Table comparing the Raman instruments used.**

	Spex 1403	Dilor XY
Technical		
Laser plasma lines	Rejected	Not rejected
Shift from one scan to another	Insignificant on a daily basis	Could vary up to 5 wavenumbers in a few hours
Measurement time	Slow---> PMT detection	Fast---> Multichannel CCD
Sample damage risk	Low	High, increased due to focus possibility
Focus light on sample	Very difficult with thin films	Easy with thin films or ceramics
Advantages with respect to the type of sample		
Thin films	Poor, and time consuming	Good, and fast
Ceramic	Ok	Ok
Surface homogeneity	None	Very convenient

- The first one is a SPEX 1403 Raman spectrometer. This instrument has been described in (Holtz, 1987). Two cw [continuous-wave] ion laser sources, Innova 90 series from Coherent, were available; argon and krypton. The laser wavelengths and the associated photon energies are listed in Table 1.4. For the krypton laser the 647.1 nm wavelength was available due to high-pressure problems in the tube. The laser sources were automated from a portable control.

A schematic of the spectrometer is shown in Fig. 1.2. In between the laser source and the sample compartment there is also a small grating to discriminate against and reject the plasma lines, which is not indicated on the schematic. The plasma lines are not laser lines but transmission lines characteristic of electronic transitions. In the spectrometer the gratings are automated and only the initial position is entered by the operator. The two gratings are synchronized independently by two stepping motors. Coordinated with the slits, they allow one frequency to pass through the spectrometer. The slits were set up to obtain a resolution [bandpass] of 4 cm^{-1} [up to the 2nd order of dispersion], and for each source it corresponds to a certain slit width in μm. These values are read from a slit-width/spectral-band pass calibration chart.

The detector is a photomultiplier tube, which converts the received light into electrical current and amplifies that current. It is activated by a high voltage from the datamate. Datamate is the unit interfaced to the spectrometer for data acquisition and monochromator control.

One scan should not generally be setup to last more than an hour, and the 30,000 counts/sec maximum for the intensity for the PMT tube should be respected.
The files can be saved on a 51/4 floppy disk to be later converted to ASCII files and manipulated with data analysis software.

Table 1.4 Laser wavelengths (in vacuo), photon energies, frequencies, and maximum outputs powers for Coherent lasers, (Holtz, 1987).

λ (A)	$\hbar\omega_L$ (eV)	λ^{-1} (cm^{-1}) (meas)	Power (mW)
Argon-ion			
4579.	2.712	21838.8 (21834.6)	400
4658	2.666	21468.4	-
4727	2.628	21155.1	-
4765	2.607	20986.4	-
4880	2.545	20491.8 (20490.6)	2000
4965	2.502	20141.0	-
5017	2.476	19932.2	-
5145	2.414	19436.3 (19433.6)	2400
Krypton-ion			
5682	2.186	17599.4 (17598.7)	150
6471	1.919	15453.6 (15453.4)	600
6764	1.836	14784.2 (14782.7)	140
7525	1.651	13289.0 (13288.0)	150
7993	1.554	12510.9 (12509.0)	50

Two configurations have been used to mount the sample. The usual one is the backscattering configuration, and the other "near backscattering" was used for the films [Fig. 1.3]. It is more convenient to use the second method for the films as the scattering intensity is already weak, and this configuration discriminates against the primary reflection, (Holtz, 1987).

- The second instrument used is a Microprobe Dilor XY. Generally, the microprobe specifies that the laser excitation is imaged onto the sample at the microscope focal plane. The microscope is used to direct the light and to also collect and focus the scattered light onto entrance slits of the spectrophotometer. A monitor is used to focus the light at the surface of the sample and this is also very convenient to check the homogeneity in the response at the surface of the sample. It also helps to double check if the sample has not been damaged by the focused light, if used at too high powers [100 mW or higher on the studied thin films]. There is also the possibility to take a picture of the surface of the sample, as a camera is mounted with the monitor.

The laser was a cw argon ion laser from Selex; the argon 514.5 nm green line was used. The spectrometer is composed of a foremonochromator and a spectrograph. The principles are the same as for the Spex. The gratings are mounted in the same configuration but on the same shaft for a better synchronization purpose and the mirrors are shifted in a different plane [Fig. 1.4]. The detection is multichannel and performed by a CCD Peltier-cooled array. The multichannel detection usually reduces the acquisition times by nearly three orders of magnitude (Hummel, 1995).

A He-Ne laser could be used for calibration purposes. On the other hand, the argon plasma lines are not discriminated against and generally appear in the spectra.

Therefore they were used as references for calibration. The unit interfaced to the spectrometer is a PC, and the files can be directly saved as ASCII files. The samples were always mounted in a backscattered geometry with the DILOR.

1.2.3. Infrared

a) Theory

Infrared involves a different mechanism than Raman. It is not an inelastic scattering but a direct absorption. The wave character of the electric field implies that energy can be transferred to a transition involving a dipole: e.g. to an electronic or vibrational change. Therefore a photon is directly converted to a phonon, and the intensity versus the wavelength can be recorded and not versus a frequency shift. Raman mechanism is more complicated than IR mechanism, but the instrumentation associated with it is simpler than the one associated with Fourier Transform Infrared Spectroscopy (FTIR).

Similar principles using group theory can be applied to work out the infrared active modes in a crystal. In crystals with a center of symmetry, phonons that are IR active cannot be Raman active due to selection rules. Non-centrosymmetric crystal modes may be simultaneously IR and Raman active.

The instrument is a Michelson interferometer [Fig. 1.5]. The Michelson interferometer works with light wave interference. This device can divide a beam of radiation into two paths. The beamsplitter partially reflects the light to the fixed mirror and partially transmits to the movable mirror. There is a retardation phase difference between the two paths, and depending on the position of the movable mirror the beams can interfere destructively or constructively.

The amplitude of the interferogram is directly proportional to the intensity of the source. It also depends on instrumentation such as the efficiency of the beamsplitter, detector response, amplifier characteristics.

The simplest equation representing the interferogram is:

$$I(\delta) = B(\bar{\nu}) \times \cos(2\pi\bar{\nu}\delta) \qquad (1.2.8)$$

where $B(\bar{\nu})$ includes the source intensity and the instrumentation factors, and δ stands for the phase difference between the two paths. This technique is called Fourier transform infrared (FTIR) spectroscopy as the interferometer measures the Fourier transform of the spectrum $B(\bar{\nu})$ [interferogram], and software needs to be used to take the Fourier transform of the interferogram to provide the desired spectrum of intensity versus wavelength. Above, only the general principle of the Michelson interferometer has been outlined. In the FTIR system, the interferogram is taken as a function of time rather than as a function of retardation.

The Fourier transformation is achieved by software. The use of Fast Fourier Transform [FFT] is more time efficient than the conventional Fourier Transform. For the conventional method, a summation is performed at each wavenumber over all the points sampled. The FFT involves an algorithm which reduces computation time. The FFT is performed using the exponential rather than just the cosine, and the spectrum.

b) Instrumentation

The spectra were obtained with a Bomem DA 3.02 FTIR spectrometer. The general outline has been described above. The spectrometer is composed of two parts. Figure 1.6 shows a schematic of the spectrometer. The Michelson interferometer and the software to perform the Fourier Transform of the interferogram, as explained previously. Few specific descriptions will be outlined below. Find in Table 1.5 the configuration used for the studied samples.

Table 1.5 Elements used in the interferometer Bomem DA 3.02.

Element	Far Infrared Low Energy 100-700 cm^{-1}	Mid infrared High Energy 500-5000 cm^{-1}
Detector	DTGS/Poly	DTGS/KBr, LN_2 cooled
Beamsplitter	Mylar of 3μm	KBr or KCl
Source	Globar	Globar

One of the most important factors is the way the data are taken. There are several different ways a sample can be loaded in the sample compartment. The easiest one is transmission [or absorption], where the sample is directly loaded in between the output of the interferometer and the detector. For the reflectivity mode, the beam can be incident near normal incidence on the sample or around 80° [grazing incidence] with p-polarized light. This last method has been first highlighted by (Berreman, 1963) who explained that LO modes could be observed at oblique incidence with a p-polarized light. (Palik, 1985) summarized the kind of information which can be extracted from the different configurations. Figure 1.7 summarizes the three possibilities.

In this work, the reflectivity measurements were done at grazing incidence for the thin films. Infrared reflectivity at normal incidence did not give any signal for these very thin films. With bulk pellets or large crystal samples, any geometry could be used since the signal was strong. Normal incidence was naturally favored for bulk samples, since the analysis is more straightforward for normal incidence.

1.2.4. UV-Visible

Basically the same approach is used in the ultraviolet (UV) and visible part of the spectrum as in the infrared. The intensity of reflected or transmitted light is measured versus the energy. But UV-visible spectra were measured directly with conventional spectroscopy, not with an interferometer. From reflectivity measurements, interband transitions can be determined for semiconductor (Feng, 1989). Here it has mainly been used in the transmission configuration for absorption measurements to determine the optical bandgap. Some effects can arise as a result of interference within the sample, such as the dependence of transmittance on thickness and wavelength.

The instrumentation has been well described by (Feng, 1989) and will simply be summarized below. The instrument is composed of six main pieces, shown schematically in Fig. 1.8.

- Three types of source are available. A deuterium lamp working in the near UV region, a tungsten lamp for visible near IR, and a globar source for the IR region.
- Two stages are used in the monochromatic spectrometer. The first stage is a prism monochromator Model 160 Perkin Elmer or an optical filter depending on the region selected. Its role is to transmit light within a narrow wavelength bandwidth so that higher diffraction order in the second stage will be eliminated. The second stage is a grating monochromator, Model 16U Perkin Elmer, which will insure the spectral dispersion.

- Detectors.

  A Pyroelectric detector which is sensitive to IR heat radiation is available in the IR region. For the main range in the UV-visible, a PMT [photomultiplier tube] converts the optical signal into an electrical signal. An AC electrical signal is produced because a mechanical chopper is used which simulates a kind of optical pulse. The mirror system between the grating and the PMT is to focus the monochromatic light on the sample.

  Before being sent to the computer, the output signal of the PMT is sent to a Princeton EG&G lock-in amplifier to clean the signal from noise and additional frequencies.

- Automation.

  There are two motors which control the prism and the grating. They can be adjusted manually for tests but are controlled by the computer APCII during a scan; the proper coordination of both will give the right selected photon energy by the user in the program. There are therefore three serial interfaces to the computer; one for the amplifier and one for each motor.

The choice of the different above elements depends on the selected range; their combination is summarized in Table 1.6. In this study the instrument has only been used in the UV-visible region and not the IR region.

Before the use of the instrument a check of the calibration and the synchronization has been done. It was done using an external mercury source. The spectra from 1.5 to 3 eV was obtained, and the lines checked with a standard. The mercury yellow doublet was clearly resolved with a width of 1.7 meV. The positions of 2.1404 eV and 2.1482 eV compared well with the reference values of 2.1404 eV and 2.1481 eV respectively.

Table 1.6 IR-near-UV spectrometer components, (Feng, 1989).

Range λ (μ)	Range ħω (eV)	Source	1st stage	2nd stage (grating, lines/mm)	detector
0.20-0.39	6.20-3.20	D_2-lamp	Prism	2880	PMT
0.38-0.83	3.27-1.50	W-lamp	Prism	1440	PMT
0.77-1.03	1.60-1.20	W-lamp	Prism	1440	Pyro
0.88-1.24	1.40-1.00	W-lamp	Prism	640	Pyro
1.18-2.48	1.05-0.50	W-lamp	301-1308	640	Pyro
2.38-4.13	.520-.300	Globar	221-1787	240	Pyro
4.00-6.36	.310-.195	Globar	221-1788	240	Pyro
6.20-10.2	.200-.121	Globar	221-1789	101	Pyro
10.1-16.1	.122-.077	Globar	221-1790	101	Pyro

1.3 X-Ray Diffraction

This technique also uses electromagnetic radiation, but of much shorter wavelength [Å]. Though the mechanism involved is different, it is in many ways complementary to the optical techniques used in this study, especially Raman. Their small wavelength, on the order of the distance between atoms, enables us to study structure.

A general approach to x-ray diffraction can be found in (Cullity, 1978) and a more detailed one can be found in a book by one of the founders (Warren, 1969).
X-rays are produced by a beam of high-energy electrons hitting a metal target [anode]. The cathode is the source of electrons, and a high voltage is kept in between the electrodes to accelerate the electrons. Once the electrons hit the target they are decelerated and emit x-rays with different wavelengths.

The principle of x-ray diffraction can be schematically explained with geometric optics, as by Bragg & Bragg in 1913. In Figure 1.9 the incident electromagnetic wave is reflected at the same angle as the incident angle. The reconstruction of the beam after diffraction of all the planes needs constructive interference. The general Bragg law is:

$$2d\sin\theta = n\lambda \qquad (1.3.1)$$

d is the spacing between the planes, n the order of the reflection, and λ the X-Ray wavelength used. The other more systematic approach is to consider each atom as a scatterer. This was first approached by Laue, and described mathematically in (Warren, 1969).

a) Instrumentation.

A Scintag PTS [Polycrystalline, Texture, Stress] XDS 2000 was the diffractometer used. This instrument is tower built with a heavy duty x-ray protection cabinet

enclosing the tube, the detector, the goniometer, and the sample holder. At the bottom are the power supplies and the microprocessor. The microprocessor is connected to a MicroVax computer system which supports DMS software for diffraction data handling and analysis, but does not handle the diffractometer's functions, which are really operated by the microprocessor.

- Source.

  The x-ray tube is a standard Varian x-ray tube with a focal spot of 1×10 mm^2 and a copper target [$\lambda = 1.4517$Å], connected to a power supply to control the current and voltage applied to it. It was used at 40 kV and 30 mA. The incident slits used to collimate the incident beam were 0.3 mm and 0.5 mm wide.

- Sample.

  The sample holder was a vertical sample holder with the option of only loading one sample at a time. This is a very convenient instrument for sample of a relatively small size and films, or powders. Crystal diffraction should theoretically only be done with a Laue instrument to keep track of the position of the sample in the holder.

- Detector.

  The solid-state detector is an ionization chamber. It is a crystal sandwiched between two conducting electrodes and an electric field applied across the electrodes. Nuclear radiation passing through the crystal will produce electron-hole pairs which are collected by the electrodes so that charge is collected for incident radiation. The output is an electrical pulse proportional to the energy of the incident ionizing pulse. The detector crystal is high purity germanium [GSDHOO3]. An extra container is attached to the arm supporting to detector to contain the liquid nitrogen necessary to cool down the detector. There were also two receiving slits of 2 mm and 3 mm.

- DMS [Diffraction Management System] Software.
  It contains many options for data handling such as background correction, peak finder, etc.

The instrument is mainly used in the standard configuration theta/two-theta [Fig. 1.10 (a)], but several other configurations can also be used. These are for texture and stress measurements. One example is a pole figure. This is a stereographic projection relative to a specific orientation of the sample. It will show a variation of pole density with pole orientation for a selected set of crystal planes. For this configuration, just the sample holder will change on the Scintag, as it will allow the sample to be rotated along rolling and transverse directions. This is not a scan, therefore the angle is fixed, and chosen at the beginning. A low indices reflection is usually preferable, as these are the strongest and the pole figure is easier to interpret.

The other configuration, useful for thin films and thus also used in this study, is grazing incidence [Fig. 1.10 (b)]. The incident angle is small and kept constant during the scan. This can lead to a film surface study, since it partly compensates for the high penetration depth of x-rays. It is also convenient for getting rid of the substrate signal. To obtain such a configuration on the Scintag machine, the receiving slits needed to be replaced and the machine realigned. The new receiving slits consist of a stack of parallel thin metal plates. The set-up is the alignment of those plates to obtain a maximum intensity at "0 theta angle" [Fig. 1.10 (c)]. The analysis of this is subtle as the diffraction vector is moving during the scan, which is not the case for the Bragg-Brentano case. If there is the slightest orientation in the films, the depth analysis [comparing scans using different angles] is difficult, as we will see in comparing the SBT films versus the TiO_2 films.

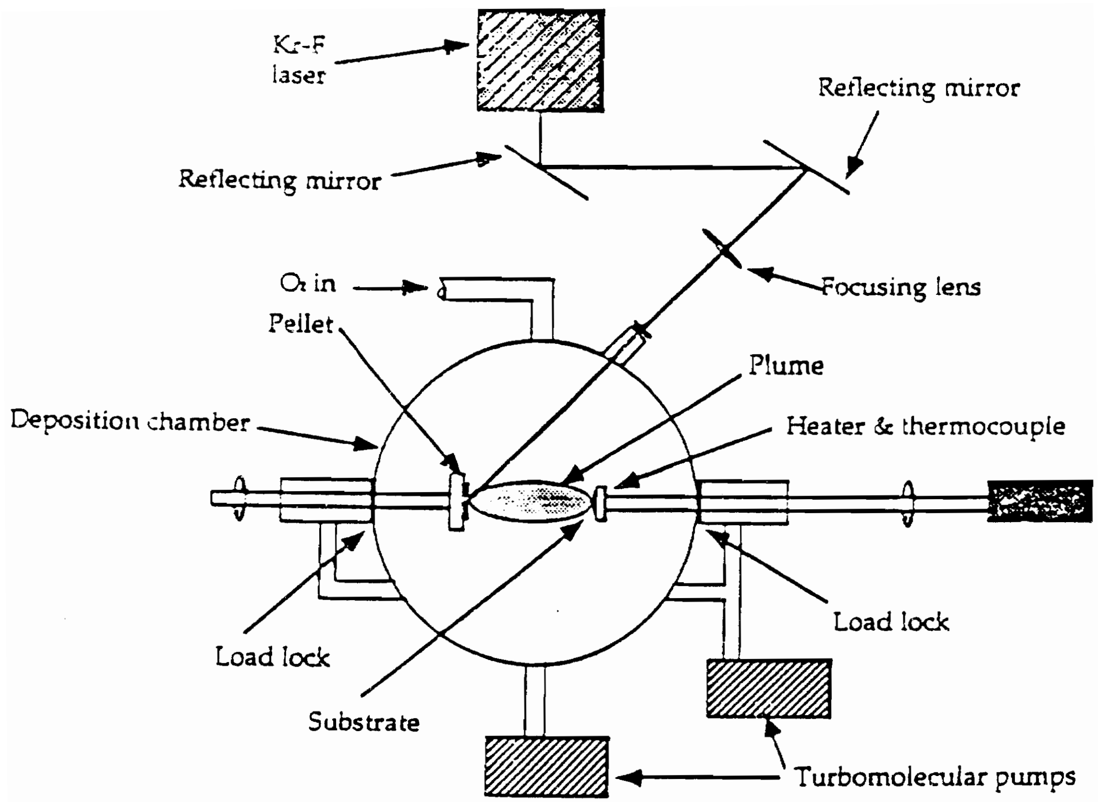

Fig. 1.1 Schematic of the pulsed laser ablation system.

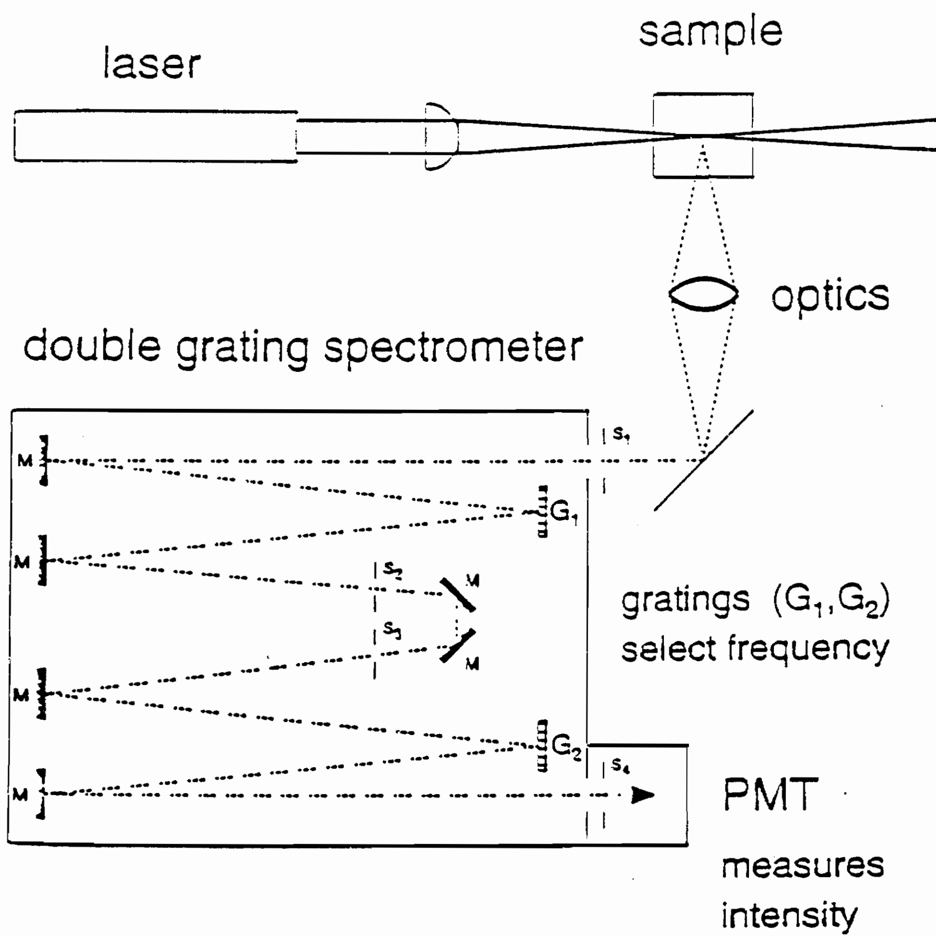

Fig. 1.2 Schematic of the SPEX 1403.

Raman scattering spectroscopy

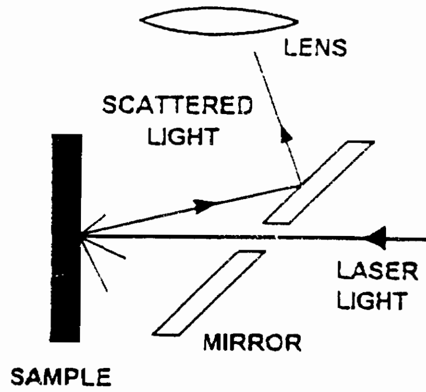

(a)

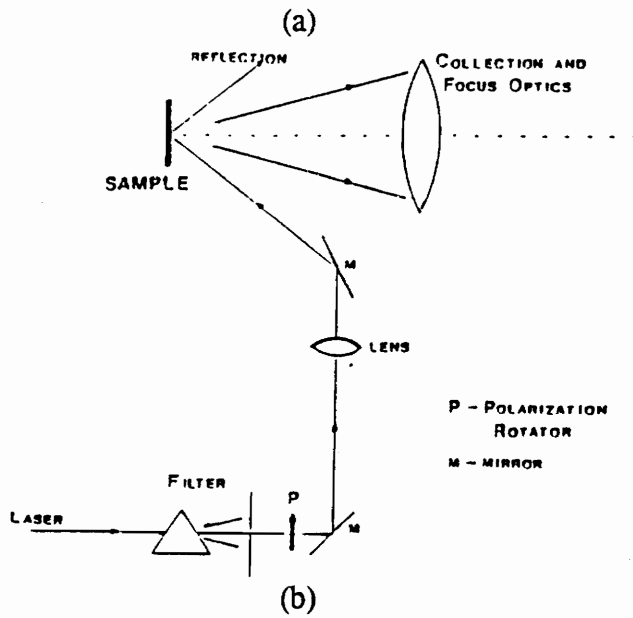

(b)

Fig. 1.3 Geometries used in Raman.
(a) Backscattering (Perkowitz, 1993).
(b) Near Backscattering (Holtz, 1987).

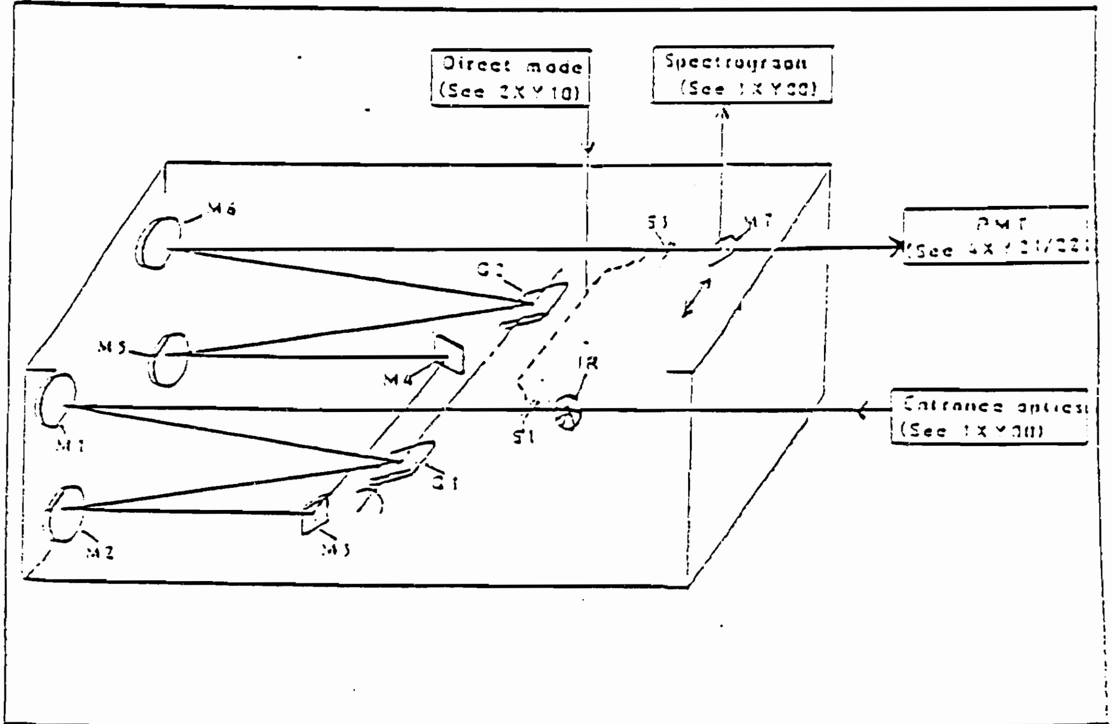

Fig. 1.4 Schematic of the foremonochromator for DILOR XY.

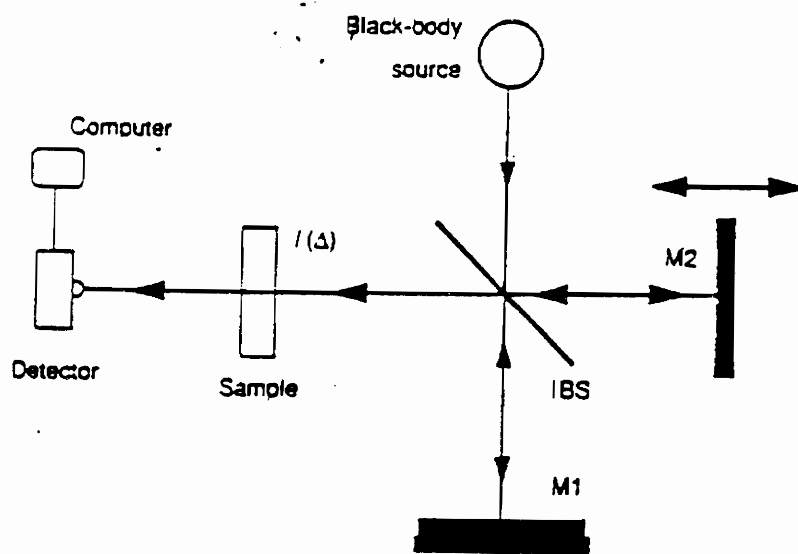

Fig. 1.5 Schematic of a Michelson interferometer.

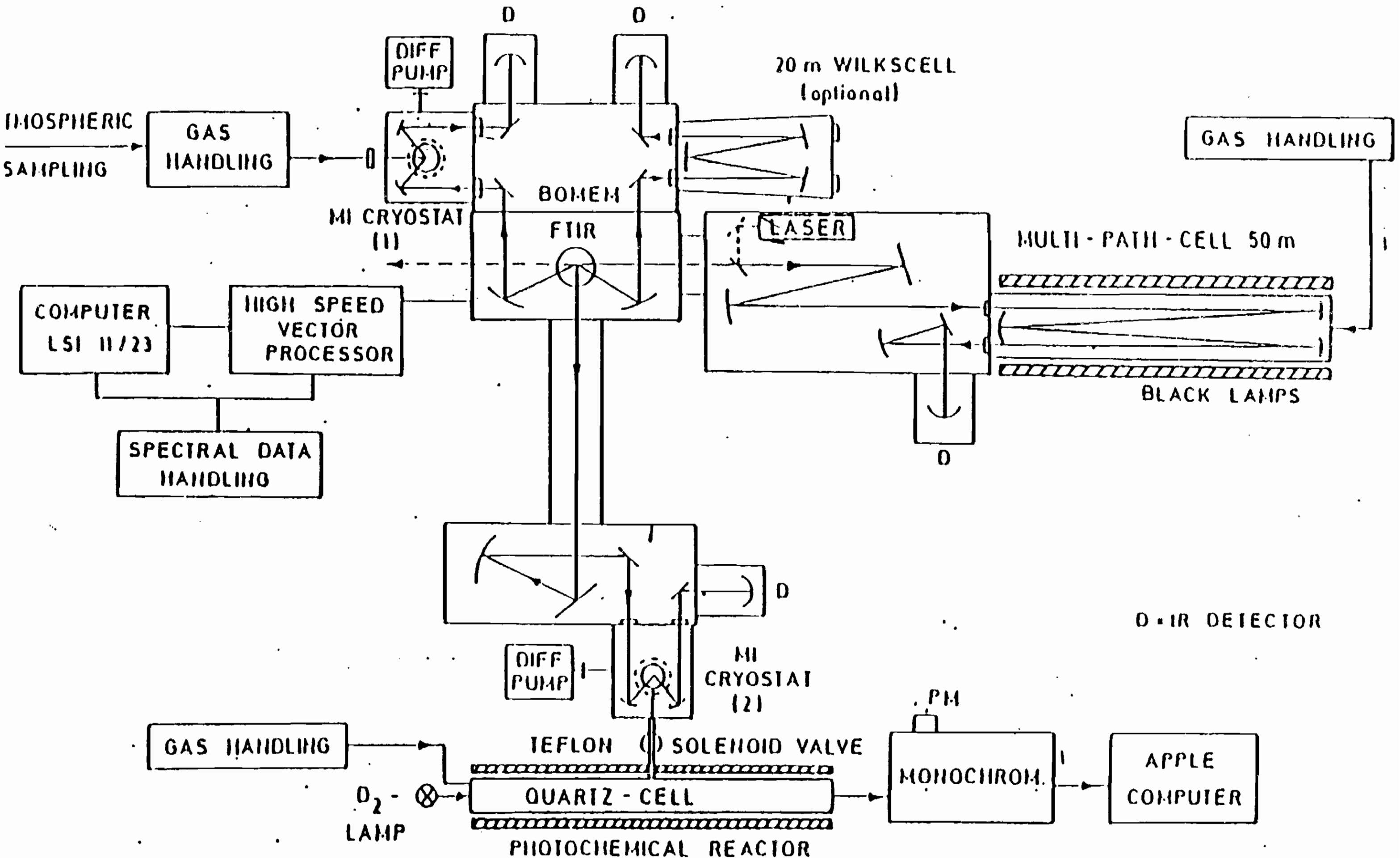

Fig. 1.6 Schematic of the FTIR Bomem DA 3.02.

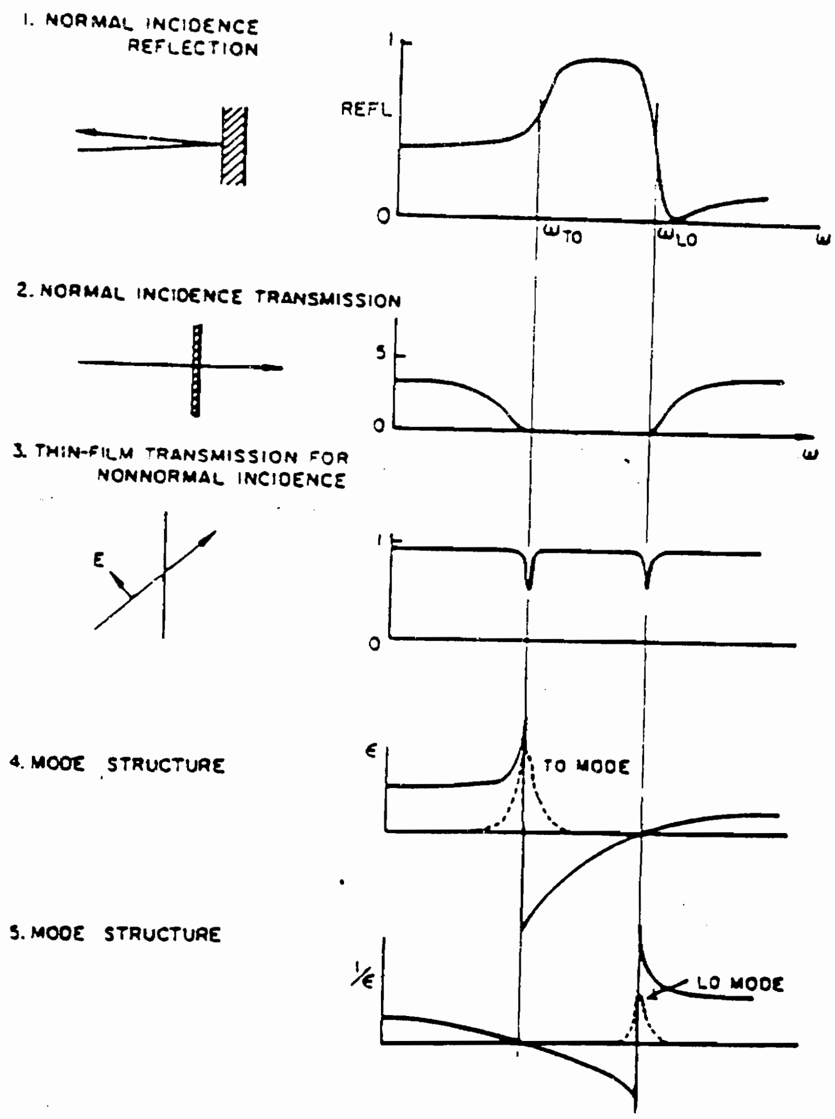

Fig. 1.7 Infrared spectra of three types of samples configurations. The sample is taken to have the idealized one-oscillator-mode structure given at the bottom of the figure with one TO frequency, one LO frequency, and a constant damping factor, (Palik, 1985).

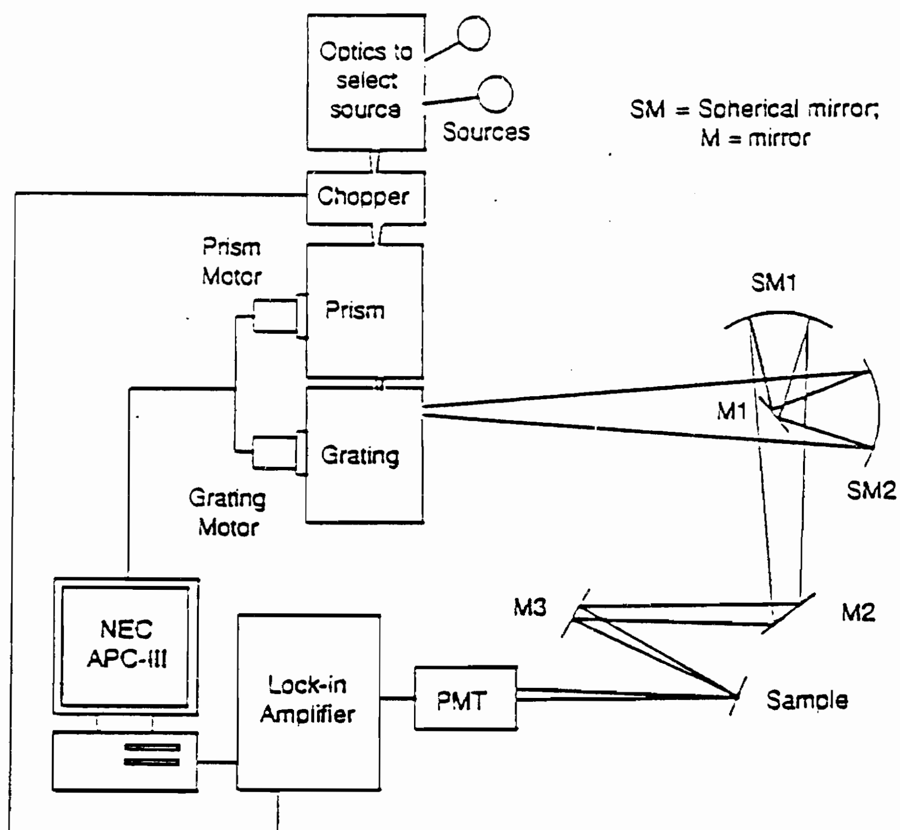

Fig. 1.8 Schematic diagram of the UV-visible set-up, (Feng, 1989).

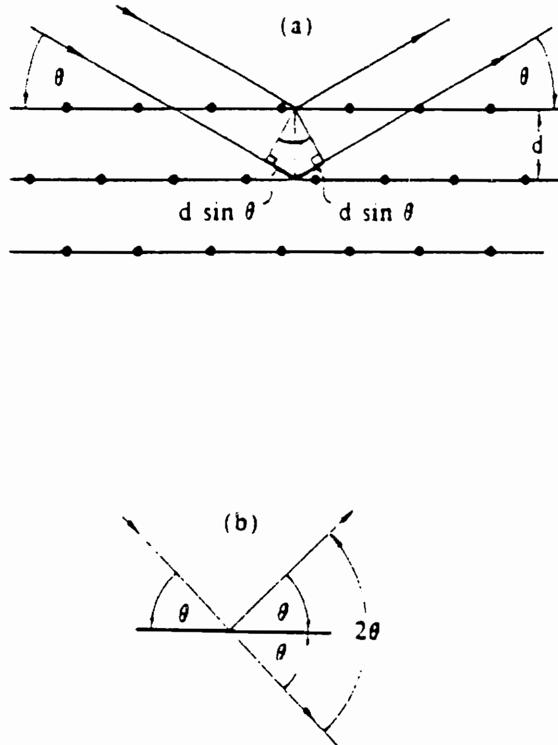

Fig. 1.9 Bragg reflection, (Burns, 1985).
(a) From a family of lattice planes.
(b) Bragg angle.

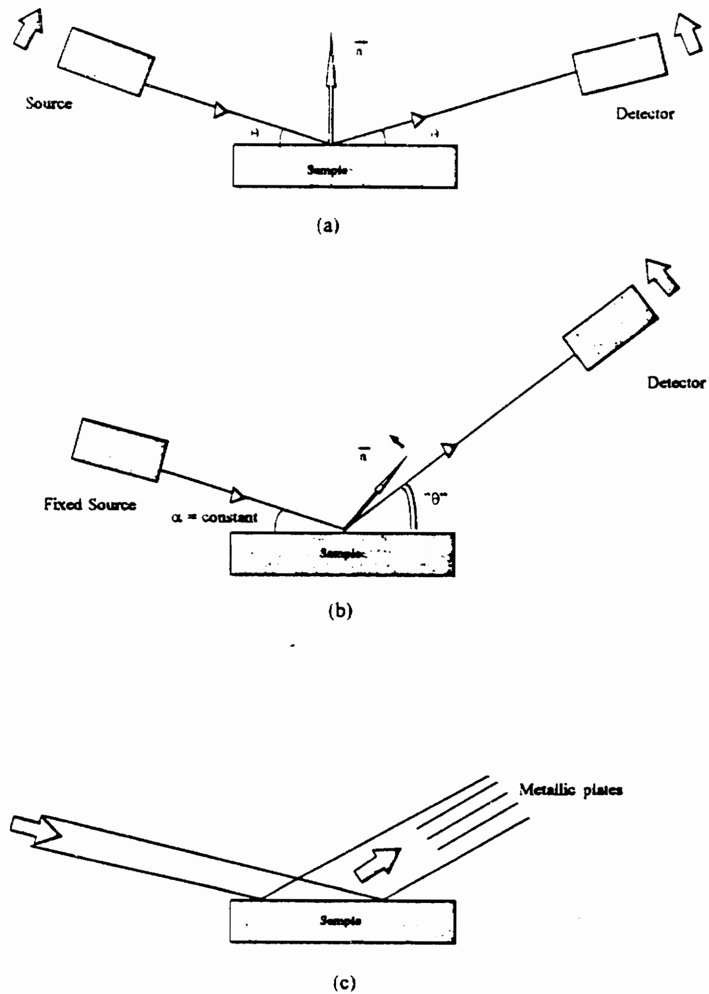

Fig. 1.10 Configurations for x-ray measurements.
(a) Bragg-Brentano configuration for x-ray measurements.
(b) Grazing incidence configuration for x-ray measurements.
(c) Schematic showing the receiving slits used in the grazing incidence configuration.

Chapter 2: $SrBi_2Ta_2O_9$ Films Made by Pulse Laser Deposition

2.1. Why $SrBi_2Ta_2O_9$ Thin Films?

The structures of the mixed bismuth-oxide layer-structure compounds were first investigated by the Swedish physicist Bengt Aurivillius in 1949, so they are called Aurivillius phases (Aurivillius, 1949). He examined their crystal structure using single crystals. But the ferroelectric nature of these materials was only revealed in 1958 for the compound $PbBi_2Nb_2O_9$ of this family (Smolenskii et al, 1984).
They can be described as consisting of Bi_2O_2+ layers in between which double perovskite layers are inserted. Other layer structure including one or three perovskite layers are respectively referred as the n=1 or n=3 phases. The n=2 structure will be discussed in more detail in section 2.3. Perovskite refers to a certain structure: most of the ABO_3 compounds have this structure. The most widely cited example is $BaTiO_3$, with a cubic perovskite structure [Fig. 2.1].

Ferroelectricity was reported first in 1921 for Rochelle Salt and in 1945 for $BaTiO_3$. For this last compound the origin of ferroelectricity can be briefly explained as follows. Above the Curie temperature [T_c], the material is paraelectric. Ferroelectricity takes place due to the lowered symmetry of the structure below T_c. Below T_c, a small shift along the axis in the position of the central Ti atom displaces the center for the positive charges relative to the center of negative charges. This displacement induces a dipole moment. The sum of all dipole moments induced in every unit cell adds up to form a spontaneous polarization below T_c. With no electric field applied, a certain number of unit cell with the same polarization form a domain. There are then several domains in a ferroelectric. When an electric field is applied, the domains are forced to line up with

the direction of the electric field. When they are all lined up, the ferroelectric is saturated. If the electric field is released, the polarization becomes the remanent polarization. If an external electric field is applied, it can reverse the polarization of the spontaneous polarization. The polarization can also be forced to zero with the coercive field. Brought to higher value, this field can force all the domains to a negative saturation. Continuing similarly as above will give a hysteresis loop. A reversible spontaneous polarization or hysteresis loop is characteristic of ferroelectric materials.

The origin of the ferroelectricity in the layer family of crystals is an active area of research. The most recent studies ((Whiters et al., 1991) and (Liu et al., 1994)) indicate that it is mostly due to a-axis displacement of the Bi^{+++} ions in the perovskite A sites relative to the chains of corner-connected TaO_6 octahedra. This evidence would indicate that it is not due to the displacement of the octahedrally coordinated cations away from the center of the surrounding octahedron of oxygen atoms, as suggested in (Newnham et al., 1971).

Ferroelectric materials are fashionable candidates for potential computer memories. (Araujo et al., 1995) report a fully functional 256-Kb FRAM [Ferroelectric Random Access Memory] manufactured with $SrBi_2Nb_xTa_{2-x}O_9$.
A memory chip consists of millions of memory cells to store information. This is integrated using the standard VLSI [Very Large Scale Integration] procedures: ion implantation, etching, photolithography. A standard memory cell would consists of a single transistor and a single capacitor. The role of the transistor is to convey a signal through the drain to the capacitor. The information is stored as a charge [0, no charge; 1, charged] in the capacitor. For the FRAM, the capacitor would be replaced by a ferroelectric in between two electrodes.

Their electric dipole orientation is the key to store "1" and "0" by applying a voltage. 0 is therefore encoded using the remanent polarization, due to their dielectric hysteresis loop. It is used as a memory element by itself. It also presents the advantage of retaining the information when the power is interrupted; it is a non-volatile memory. Moreover, their large dielectric constant make them also appealing as capacitors in DRAM (Dynamic Random Access Memory).

The possibility of using ferroelectric materials as storage element was discovered long ago. But recent developments in the technology of thin films have made it realizable. Smaller thickness means that a smaller voltage is necessary.

One of the main concerns is the fatigue; performance declines with use. This was recently investigated at Virginia Tech (Vijay, 1995) and is also the subject of numerous other studies. Laser ablation was the ideal solution for complex compound material such as the Aurivillius layered-structured; but the high cost of pulsed laser deposition is unappealing for an industrial process. Recent developments (Harshavardan et al., 1993) have reported the deposition of uniform, 16 inches PLD thin films. Commercialization might start in the near future for the ferroelectrics, due to the recent improvement in laser ablation systems.

This study really started because different films showed different hysteresis loops, and a characterization was necessary to determine why. The same materials are now deposited with other methods (Amanuma et al., 1995). These more "traditional" processes are also more predictable than the laser ablation which is a deposition method under study (AIP Confefence proceedings 288, 1993). The present work will also study some of its new aspects.

2.2 Samples

In addition to the thin films, crystals and pellets were also studied. The crystals and pellets provided spectroscopic standards that helped to characterize the films. They also turned out to be very interesting in their own right.

2.2.1. Crystal

$SrBi_2Ta_2O_9$ [SBT] crystals were obtained from Prof. R. E. Newnham, Penn State. They had been grown in 1972 for his study on $(SrCa)Bi_2Ta_2O_9$ crystal structure (Newnham et al., 1973). Their preparation is similar to the one described as follows in the article: "They were prepared from reagent-grade Bi_2O_3, TaO_2, $SrCO_3$, using excess Bi_2O_3 added as a flux. After mixing in a chemical shaker, the oxides were packed in Pt crucible containing a Pt mesh basket, and heated to 1250°C. The melt was held at this temperature for several hours, and then cooled to 900°C at about 2°/hour. Crystals were withdrawn before the melt solidified by raising the basket from the bottom of the crucible and then annealed."

The crystals were small, 1 mm edges and 50 μm thick and flaky of an orange-brown color with c-axis perpendicular to the surface. There are also composed of domains; a domain is a region of the crystal where all the dipoles are aligned in the same way. Therefore there might be some kind of averaging effect in the following studies.

2.2.2. Pellets

A pellet is a polycrystalline dense bulk of material. The targets used for the laser ablation were of the desired composition. $SrBi_2Ta_2O_9$ was prepared as described in section 1.1.2. Commercial powders of $SrCO_3$, Bi_2O_3, Ta_2O_5, Nb_2O_5 were mixed in stoichiometric ratio by ball milling, followed by calcination of the mixed powders at

10000 psi in a circular die and sintering of the pellets at 1100°C for 1 hr in a regular box furnace.

A set of small pellets was used:

$SrBi_2Ta_20_9$ (SBT)	$SrBi_2Nb_20_9$ (SBN)
$CaBi_2Ta_20_9$ (CBT)	$CaBi_2Nb_20_9$ (CBN)
$PbBi_2Ta_20_9$ (PBT)	$BaBi_2Nb_20_9$ (BBN)
	$PbBi_2Nb_20_9$ (PBN)

2.2.3. Films

There are many films and a range of parameters had to be chosen to narrow the study. They were numerous films prepared with various values of preparation parameters such as frequency, substrate, or chemical composition [e.g. Bismuth excess]. These films have been used to start the experiments but not to directly conclude on the results. The role of the different deposition parameters will be described in more detail in the TiO_2 part of the study.

For the sake of simplicity and brevity the most important and extensively studied ones are going to be presented. The common deposition parameters are the following: 10 Hz laser pulses rate, 200 mJ laser energy, 200 mTorr O_2 atmosphere. The first set of samples is much thinner, because the deposition time was different. Table 2.1 lists those thin samples.

Table 2.1 List of thin films.

	1st Set <24,000 pulses	2nd Set 24,000 pulses
Deposition Temperature(°C)	750	750
	700	700
	650	650
	600	600
	500	550

2.3 $A2_1am$ Space Group on Pellet and PLD SBT Films: Confirmation by X-rays

Figure 2.2 shows the results for the x-ray diffraction (XRD) patterns of different films at different substrate temperatures. As the patterns are rather complicated, a systematic indexing was necessary. A SBT pellet has been used as a reference, and is assumed to be non-oriented. Its XRD pattern is shown in Fig. 2.3. Another pellet of the same family has also been run for comparison, $SrBi_2Nb_2O_9$ (SBN). The XRD pattern is seen to be very similar to that of SBT. Therefore the same crystal structure can be expected for SBN and SBT, as also shown in earlier studies (Smolenskii et al., 1984). This may be general in this work. I found similar situation for some samples (studied by Raman and infrared) in which tantalum was partly substituted by niobium.

The XRD data obtained from the pellet, the peak positions and relative intensities, were compared to theoretical powder patterns generated by Crystalpow (program developed by Dr. G. V. Gibbs at Virginia Tech). The information needed for the programs were extracted from the literature search (Newnham et al., 1973), (Rae et al., 1992). These bismuth oxide layered structures were first described by Aurivillius as orthorhombic (or pseudotetragonal as $a \approx b$) with a Fmm space group (number 69 in standard listing), but these refinements obtained a different space group due to weak superlattice reflections not observed by (Aurivillius, 1949). The refinement of (Rae et al., 1992) is supposedly a more accurate refinement than (Newnham et al., 1973). However there is a complication with the conventions chosen for the crystal-axis. They were both working with different settings than the international setting for the space group 36 $A2_1am$ (-cba) instead of $Cmc2_1$ (abc). Moreover the origin in (Rae et al., 1992) is along a to coincide with the Bi at the perovskite B site, for convenience as the refinement starts with approximate structure of the parent structure Fmm.

After transforming the $A2_1am$ space group to the international one $Cmc2_1$, the programs Xtaldraw [which generates crystal structure], Metric [which generates bond length, angles], and Xtalpow[which generates powder pattern] were used. The easiest thing to do was to compare the powder patterns. In Figure 2.4, the unit cell of SBT is indicated using the (Newnham et al., 1972) refinement.

Figure 2.5 shows that the powder pattern generated with the data from (Newnham et al., 1973) matches with our results for the SBT pellet. The strongest peak at 2 theta = 29.08, as well as the other strong peaks, are correct. For reference, Appendix 1 contains the input and the output of Xtalpow. The input consists of the cell parameters and the atomic positions. The expected peaks positions and relative intensities of the XRD pattern for a randomly oriented powder is the output generated by Xtalpow.

The starting material was concluded to be orthorhombic with space group $A2_1am$ (36).

- **Crystals**

There were five crystals which have been run in the normal configuration. The results are shown in Fig. 2.6. Some of them gave better patterns than others. As they are pseudo single crystals, the way they are loaded on the holder is very important [The Scintag is not optimized to run single crystals]. It was obviously not the same position for every sample, and that might causes the difference. At low 2-theta values, there is broad diffraction which usually indicates the presence of an amorphous phase. Here this is simply due to the tape used to maintain the crystals, which is detected. Not all the peaks from the pellets are present in Fig. 2.5. This is normal as the pellet is a randomly oriented powder and the crystals are oriented with

the c-axis perpendicular to their surface. Though many peaks show up, it might simply be due to the domains. But once again the structure $A2_1am$ is confirmed in the crystals, consistent with (Newnham et al., 1973).

- **X-ray results on the thin Films**

The first runs for the films were also done in the normal configuration. The platinum substrate shows several peaks, which will need to be excluded from the pattern of the films. The peaks which come from the substrate will just be denoted Pt.

The two extreme samples of each set have been run [Fig. 2.2] but only set 2 will be detailed. The peaks have been indexed using the pellets and the Pt substrate. Only the major peaks are labeled; the others are listed in Appendix 1, and Table 2.2. Not all the peaks from the powder are present in the films, and the films do not show the same peaks among each other. Table 2.2, next page, lists the peaks observed in the patterns. It is clear that none of the films is an exact replica of the pellet. But they do not show any additional peaks which are not in the pellet. Some of the films peaks are not observable in the XRD pattern of the pellet. They are too weak to be seen, but they are present (with weak intensities) in the listing for the simulated XRD pattern of the pellet [Appendix 1]. Thus there is no indication of a phase in the films different from that of the pellet. A first quantitative approach shows that it is the 750 C sample from the second set which is most similar to the unoriented SBT powder specimen. The films at 750 C does not show the same texture (preferred orientation) than the film grown at 550 C. The texture seem also different from one set to another.

X-ray measurements on the thin films were also carried out at near-grazing incidence. This configuration probes a thin film (or near surface region) more effectively than

the normal configuration, i.e., it is more surface sensitive. Thus in our near-grazing results on the films, the signal from the Pt substrate was nearly absent and no longer a complicating factor.

Table 2.2. **Comparison of the x-ray diffraction peaks present in the patterns observed for the thin films and the pellets.**

Angle	Set1 750	Set1 500	Set2 750	Set2 550	Pellet	h k l
14.14	weak		weak	medium		0 0 4
17.9			weak	weak		Pt
21.27	weak		medium		weak	0 0 6
23.16					weak	1 1 1
25.28					weak	1 1 3
28.5			medium			0 0 8
29.08	medium	Very strong	medium	very strong	strongest	1 1 5
29.8			medium			0 1 7
32.5, 32.63			weak		medium	2 0 0/0 2 0
34			medium			1 1 7
35.8					medium	0 0 10
36	medium	weak	medium	weak		Pt
38	medium	medium	medium	medium		Pt
39	Very strong	Very strong	Very strong	Very strong		Pt
39.8					weak	1 1 9
44					weak	2 0 8/0 2 8
46.8			weak		medium	2 2 0
49.17,			weak		medium	2 0 10/0 2
51			medium		very weak	0 0 14
51.9					weak	2 2 6
53					weak	1 1 13
55.9, 56.06					medium	3 1 5/ 1 3 5
59		medium				3 1 7/ 1 3 7
60.27, 60.3			mini	very strong	small	2 2 10/ 1 1
67.8			weak			2 1 15?
69.05	strongest	Very strong			weak	0 2 16?

First, as a check, the pellet has been run in the grazing incidence to see any differences with the films. This is shown in Fig. 2.7 where no differences were observed except an attenuation in peak intensities, as expected.

Fig. 2.8 shows XRD results on the films obtained for various near-grazing angles of incidence from 2° to 6°. Four samples measured [(a), (b), (c), (d) of Fig. 2.8]; two each at two substrate temperatures. The peaks due to the substrate are very weak, thanks to the surface-sensitive nature of the near-grazing geometry. For the first

sample set at 750 C, there is a strong peak at 55.9° which does show also in the normal configuration. Though it was present in the 500 C sample, it is weaker in this case, and the peak at 29° is now very weak also. For the second set, same differences between the normal and grazing angle scan can be found. For the 750 C sample of the second set a medium intensity peak at 6° has appeared, and also one at 56°.

If an oriented sample is run at different grazing incidences, there will be different patterns as the diffraction vector is changing. The thin films have also been carefully mounted parallel to the holder and rotated in the sample plane to double check. The fact that the random-oriented powder did not show any significant differences between the normal scan or the scan at grazing angle reinforces the idea that there is a different orientation effect in the films at different temperatures.

A pole figure, as discussed in section 1.3, has also been measured. Figure 2.9 shows this measurement. The strongest peak at 29° on the first set 500 C sample has been chosen. The result leads to a strong texture. Texture is another word for preferred orientation.

- **Conclusions**

The x-ray patterns indicate that the same phase, with $A2_1am$ structure, is present in both the films and the target pellets.

The films are different from each others due to a preferred different orientation at different temperature deposition. There are also differences in texture from one set to another.

2.4 Raman

This study was carried out with the laser Raman microprobe DILOR XY and the SPEX 1403 Raman spectrometer, both described in chapter one. All measurements were taken at room temperature in the backscattering configuration, using the 514.5 nm argon green line. An article by (Graves et al., 1995), report Raman studies on various Aurivillius layer compounds. Through this entire section, a comparison is made to that work (Graves et al., 1995), which will be sometimes referred as "their work" or "their data".

2.4.1 Pellet and crystal Specimens - Comparison with literature

Fig. 2.10 shows the Raman spectra observed for SBT pellet and the SBT crystal. Several crystals have been scanned at different points on their surfaces; the spectrum was the same in all cases. The spectrum shown in the lower part of Fig. 2.10 was chosen because it is least contaminated with laser plasma lines (one is present at 515 cm-1).

The small broad peaks between 323 and 528 cm-1 match very well in both spectra. The strong bands on the other hand do not match as well. The strong features for the crystal are below 200 cm-1 at 167 and 182 cm-1, and for the pellet at 214 cm-1. The strong sharp band at 811 cm-1 in the crystal is shifted to 817 cm-1 in the pellet and is also broadened. Table 2.3 lists the observed Raman lines.

Raman data on the Aurivillius phases has been found in literature (Graves et al., 1995) reported by a group that included the scientists who worked on the SBT structural refinement mentioned in section 2.2. Their spectra on powder specimens are shown in Fig. 2.11. Table 2.3 also contains a comparison with their work.

Table 2.3 **Raman lines in our powder and crystal specimens compared with the data in literature (Graves et al., 1995).**

SBT crystal #4 spot 1 DILOR XY [cm-1]	SBT pellet-SPEX and DILOR data [cm-1]	Data from Graves et al. on Powder specimen [cm-1]	Shift in between our powder data and literature [cm-1]
167 strong sharp	164.7	?	
182.5 strong sharp			
215 shoulder	214.5 strong Sharp	202 strong sharp	13
250 medium/small	238 shoulder	227 shoulder	11
324 weak	323.5 broad	312 small	12
368 broad	368 broad	354 small	14
434 broad	434 broad	422 small	12
459 shoulder	459 broad	447 small	12
518 broad	518 broad	506 small	12
612 sharp	606 medium sharp	593 medium	13
812 strong sharp	818 strong sharp	803 strong sharp	15

The positions and relative intensities of the different peaks are in general agreement with our data. But for the three main peaks at 215, 606, and 817 cm-1 in our pellet spectrum, there is an upshift of about 13 cm-1 relative to the data reported by (Graves et al., 1993). A similar shift is seen for the small peaks.

The pellet was studied with both the SPEX 1403 and the DILOR XY Raman instruments. The same peak positions were observed. The spectrum taken with the DILOR contains a spurious sharp plasma line at 116.5 cm-1 (it is visible at the upper left of Fig. 2.10). This plasma line was used to calibrate the frequency scale for this spectrum.

We also measured Raman spectra of a few other compounds of this Aurivillius family. The results are shown in Fig. 2.12. The $BaBi_2Nb_2O_9$ spectrum is compared with their data in Table 2.4. Again a shift of about 13 cm-1 is seen from the main lines. We believe that our peak positions are correct and that the reported values (Graves et al., 1993) suffer from a systematic error.

Table 2.4 **Comparison with our $BaBi_2Nb_2O_9$ Raman results with those of (Graves et al., 1995).**

Our BBN specimen	Shifts from Graves et al.	Difference [cm-1]
167.9 medium sharp		
202 shoulder	189 shoulder	13
232 strong sharp	219 strong sharp	13
305 weak	293 weak	12
457 weak	450 weak	7
514 weak	503 weak	11
570 medium broad	558 weak	12
870 medium/strong	858 strong sharp	12

It can be seen from Fig. 2.12 (a) and (b) that all the compounds of the n=2 phase share the same distinct Raman characteristics as SBT, as found for the IR spectra (section 2.5). These characteristics are strong, sometimes degenerate features between 150 and 250 cm-1, small broad peaks between 250 and 430 cm-1, a medium broad band between 550 and 600 cm-1, and the strong band at 800-850 cm-1.

There are also bands at low wavenumber which have been observed by (Liu et al., 1994). These bands have also been detected in this study with the krypton laser (λ = 647.1 nm) on the SPEX machine, using a polarizer to reduce the laser tail. They are shown in Figs 2.13. Table 2.5 compares our SBN spectrum with (Liu et al., 1994) data. There are very distinct peaks for $SrBi_2Nb_2O_9$ and SBT.

Table 2.5 Raman lines detected at low frequencies in SBN and SBT compared to reported measurements (Liu et al., 1994).

SBT [cm-1] Our data	SBN [cm-1] Our data	SBN [Liu et al.] at 27C [cm-1]
26	38	30
63	66	60
85		

As seen in Fig. 2.13 (a) the compound containing calcium seems to contain some degenerate features. Four peaks are observable in the CBT spectrum, and only one in the PBT spectrum. This is not that obvious for the niobium family, in which the spectra contain fewer peaks than the spectra of the tantalum family. The 60 cm-1 peak is shifted to lower energy for the Sr and Pb compounds.

(Liu et al., 1994) report that, as the temperature is increased, the SBN band at 30 cm-1 disappears and the one at 60 cm-1 is shifted. Above the Curie point, the distortion created by the Sr atoms disappears and with it, the ferroelectricity. Above the Curie point the ferroelectric state transforms to a paraelectric one, and the spontaneous polarization disappears. Therefore their conclusion is that the Sr atoms play a very important role in the ferroelectricity of these crystals. This is consistent with the work of (Graves et al., 1995).

There is no band around 30 cm-1 in the PBT spectrum and there are several of them in the CBT spectrum. The spectra seem to indicate that the light Ca atoms introduce a more important distortion in the n=2 Aurivillius tantalum compounds than the heavy Pb does. It might then be concluded that the Ca atoms increase the Curie temperature and the Pb atoms decrease it, as the ferroelectricity disappears with these Raman-active mode. This does seem to be the case from the phase transition temperatures reported. (Smolenskii et al, 1984) report the following transition temperatures between ferroelectric-paraelectric phases for:

SBN 430 C

SBT 310 to 335 C

CBN 575 to 650 C

CBT 550 to 600 C.

The temperatures reported by Graves et al. for SBT are 311 C and 571 C. This low-frequency Raman analysis in those compounds seems to highlight the different preferable cations of different masses which could be used [Sr, Ca, Ba, Pb] to modulate the ferroelectricity.

2.4.2 Tentative Assignment of Vibrational Modes

In the same work by (Graves et al, 1993), theoretical calculations, starting from the average Fmm structure have been done. The refinement from (Rae et al., 1992) for the atoms positions, mentioned in section 2.3 was done in a similar fashion.

The work from (Graves et al, 1993) reported Raman and IR mode assignments for Aurivillius layered structures. The tentative origin of the different modes for the n=2 phases is compared to the trends observed with our Raman measurements.

For the layered structure of the SBT type (n=2), they found three possible motions (or distortions), which might be the key to the origin of ferroelectricity in these compounds:

- The Sr ions displace along the a-axis with respect to the entire chain of octahedra. This would induce a polarization along the a direction.
- TaO_6 octahedra rotate around an axis parallel to a.
- TaO_6 octahedra rotate around an axis parallel to b.

Their work definitely assigned the strong band at 818 cm-1 to the stretching of the TaO_6 octahedra. This conclusion can be compared to trends observed from the spectra of different Aurivillius compounds examined in our work.
The lighter element Nb; substituting for Ta in the octahedra seems to introduce asymmetry in the peaks, even in the strong peak above 800 cm-1. Nb also clearly upshifts the 818 cm-1 band of SBT, as expected for a lighter metal atom in the metal-oxygen stretch. This is consistent with a Ta-O assignment for this band.

The effect of the light calcium atom substitution was discussed in section 2.4.1 in connection with the low-frequency Raman spectra. The compound containing calcium was noted to show additional Raman features compared to the others. The spectrum for $CaBi_2Ta_2O_9$ [CBT] also shows more features in the 100-1000 cm-1 range. The light Ca atom may introduce a distortion which splits degenerate modes near 200 cm-1. CBT spectrum shows two bands at 205 cm-1 and 227 cm-1. The SBT spectrum shows only one band (at 214.5 cm-1) in this region. The two bands in CBT could be the result of a lifted degeneracy. The band at 214.5 cm-1 was actually assigned to a degenerated mode by (Graves et al., 1993).

The 605 cm-1 peak in CBT is very asymmetric; a shoulder may be present indicating a splitting. The asymmetry already noted for the peaks shown by Nb-substituted material may also arise from small splittings, since Nb is intermediate in mass between Ta and Ca.

2.4.3 Pulsed-Laser-Deposited Thin Films

The thicknesses of the films investigated was of approximately 200 nm. SBT is a very ionic and the Raman scattering strength from such ionic crystal is much weaker than for covalent crystals. It was therefore doubly difficult to obtain a Raman response of the PLD SBT films. They are also very shiny and reflect very well. Most of the measurements on the films were taken on the DILOR instrument in the normal backscattering geometry. A few films were studied using the SPEX instrument in the near-backscattering geometry. It is very easy to damage the films with the DILOR microprobe, and a limit on the laser power should be respected in order to avoid damaging the films with the high power/area. Sometimes this damage cannot be seen with the eye.

The main consistent results obtained for the films was that for substrate temperature below 600 C, no Raman signal characteristic of SBT was observed. Figure 2.14 shows spectra obtained for five films prepared with higher substrate temperature. Also included in this figure is the SBT pellet spectrum (the top panel). All of the films exhibit the strong Raman band near 820 cm-1. In the four films for which the low frequency region was observable, a band near 215 cm-1 was seen. This band evidently corresponds to the strong band at 215 cm-1 in crystalline SBT.

A summary of the different peaks seen in the films is given in Table 2.6.
The shift between the Bi excess film and the film at 750 C can be explained by two factors. The Bi excess film cannot be compared with the SBT bulk for the peak position, but to $SrBi_2Ta_{1.6}Nb_{0.4}O_9$ as the Bi concentration is changed with respect to this composition and not with respect to the one of SBT. The lighter anions such as Nb instead of Ta in the octahedra upshift the 810 cm-1 band observed in SBT. This is consistent with the mode assignment (section 2.4.2).

Table 2.6 Raman peaks detected in the SBT films.

Powder specimen Our data	2.5% Bi excess film DILOR	750C 1st set SPEX	750C 2nd set DILOR	700C 2nd set DILOR	650C 2nd set DILOR
164.7	169.37		167??	167??	
	203	Laser tail			
214.5 strong Sharp			215	214	
238 shoulder					
323.5 broad					
368 broad					
434 broad					
459 broad					
518 broad					
606 medium sharp	580	582			
818 strong sharp	829	830	820	813	823??

The first 750 C film displayed on the top second panel belongs to the first set of films, and does not seem to be as stoichiometric as the films from the second set.
For the other films, only a few bands from the pellet are present. The most prominent feature is still the band at 813 cm-1.

2.4.4 Raman and X-ray Measurements Combined: Evidence for a Lower Crystalline/Amorphous Ratio for PLD $SrBi_2Ta_2O_9$ Films Grown at Substrate Temperatures Below 650 C

The two main bands in the pellet, at 215 and 818 cm-1, were observed (with difficulty) in the PLD thin films, but only for films prepared at substrate temperatures of 650 C and higher. These Raman bands were not discernible for films prepared at low substrate temperature. From the x-ray diffraction patterns on the low-substrate-temperature films, we know that a certain fraction of the material on the films is crystalline, as the patterns do contain sharp peaks. But x-ray diffraction does not indicate what fraction of the material is crystalline. Raman scattering intensity is sensitive to the percentage of crystalline material on the films. As no Raman signal was observed below 650 C substrate temperature, it is evident that the films deposited at low temperature are crystalline enough to diffract but not crystalline enough to show a measurable Raman signal. It is therefore reasonable to conclude that the low-substrate-temperature films have a lower crystalline/amorphous ratio then the high-substrate-temperature films. This is clearly consistent with the ferroelectric properties observed for the films. The films below 650 C substrate temperature do not exhibit good ferroelectric properties.

These are the first Raman results obtained on films made by pulsed laser deposition. It should be remembered that films should be thicker to make Raman a reliable characterization method for two main reasons. Raman is a weak phenomenon which requires a reasonable amount of crystalline material, and ionic crystals such as SBT do not have a Raman scattering strength as strong as that of covalent materials. The fact that Raman signals were observed at all, for the very very thin, very ionic, PLD films investigated here, is an achievement in itself.

A byproduct of the Raman measurements on the pellet and the crystals is the discovery that reported Raman frequencies for SBT and its Aurivillius relatives are too low (by about 13 cm-1).

In the films exhibiting good ferroelectric properties, the Raman bands at 215 and 818 cm-1 are present. A previous report attributed this 818 cm-1 band to the stretching of the octahedra formed by Ta or Nb anions surrounded by the six oxygen atoms. The fact that this band is upshifted to higher wavenumber on our Raman measurements of SBN and SBT is consistent with this interpretation.

Calcium introduces additional low-frequency Raman lines that are not seen in SBT, perhaps because the lighter mass of Ca introduces larger splittings of near-degenerate modes.

2.5 LO and TO Modes from Infrared Measurements

2.5.1 Infrared Measurements on the Pellet and the Crystal

Infrared reflectivity measurements were initially carried out on the bulk pellet and the single crystal from Penn State. This was done using near-normal incidence and a gold mirror as the comparison reference. The results are shown in Fig. 2.15.
The spectra show the same general features. The crystal was mounted so that the c-axis [the long one] was perpendicular to the surface, due to the geometry of the crystals. Thus there is no E||c contribution in the measured spectrum. The thin thickness of those flaky samples does not allow us to make measurements from the side. The domains in this ferroelectric crystal may affect the spectrum.
For the pellet sample, all the polarizations should be present. A weak band at 235 cm-1 is noticeable in both spectra. The one at 307 cm-1 for the pellet is shifted to 320 cm-1 in the crystal. A strong band at 465 cm-1 in the pellet is at 485 cm-1 in the crystal. The high frequency reflectivity cutoff is near 800 cm-1 for both samples (This feature is characteristic of a longitudinal-optical phonon.). Also seen are two not-so-pronounced bands at 570 cm-1 and 690 cm-1 for the pellet. Since these are absent in the crystal, they may correspond to E||c features.

It was not possible to obtain IR reflectivity data at normal incidence on the films, because they are too thin ($\approx$ 200 nm). The film thicknesses were much smaller than the infrared wavelength. Therefore the near-grazing incidence set-up was used for the films, since more light goes through the material this way. The films were grown on $Pt/Ti/SiO_2/Si$ substrate and this was taken also as a reference in the IR measurements. Figures 2.16 and 2.17 show the results of the near-grazing infrared reflectivity measurements, carried out on two sets of six samples.

For the first sample set shown in Fig 2.16 the absorption at 440 cm-1 is present in all the samples but more weakly in the low substrate-temperature ones. A very strong absorption near 740 cm-1 is present at all substrate temperatures. Its variation with substrate temperature does not reveal a systematic trend.

A peak at 546 cm-1 appears sharply in the 700 C substrate temperature film of the first set [Fig. 2.16]. In the 2nd set [Fig. 2.17] this same peak seems more consistently present than in the 1st set. The 546 cm-1 peak has a tendency to sharpen with increasing temperature of the substrate.

The data on the first set are not very smooth in the low energy range. Most of the peaks come from interferences with the signal of the Pt substrate [Fig. 2.16], such as the peaks at 360 cm-1, at 400 cm-1, and also at 440 cm-1.

2.5.2 Infrared Reflectivity Data Fitted with the Factorized Form of the Dielectric Function

The crystal data has been analyzed to estimate the optical constants in the studied region, so that these could then be used for analyzing the films and the pellet. It should be noted that it was for this main purpose that an effort was made to obtain SBT crystals in this study. The crystal data was used because it is closer to a single polarization, since it contains E || a and E || b, but not E || c. The pellet spectrum contains all three. The analysis given below is actually valid only for a pure polarization. Thus the results must be treated as an approximation.

The way a crystal is going to respond to incident radiation is dependent on the nature of the dielectric function response. The reflectivity is the quantity being measured. The dielectric function and the reflectivity are complex and related by the following relation:

$$R = [\frac{(n_c - 1)}{(n_c + 1)}]^2 \qquad 2.5.1$$

n_c and ε_c being related through:

$$\begin{aligned} n_c &= n + ik \\ \varepsilon_c &= \varepsilon_1 + i\varepsilon_2 \\ n_c^{\,2} &= \varepsilon_c \\ n^2 - k^2 &= \varepsilon_1 \\ 2nk &= \varepsilon_2 \end{aligned} \qquad 2.5.2$$

Once the spectrum is obtained, there are different ways of fitting this data to obtain n and k or ε_1 and ε_2. There are several ways of proceeding. The most widely known one is using the Kramers-Kronig [KK] relations. They have been derived with Green function and complex analysis using the fact that the material can not respond before the stimulus [incident electromagnetic wave] is applied (causality).

$$\operatorname{Re} G(\omega) = \frac{1}{\pi} P \int_{-\infty}^{\infty} \frac{\operatorname{Im} G(\omega')}{(\omega - \omega')} d\omega' \qquad 2.5.3\ (a)$$

$$\operatorname{Im} G(\omega) = -\frac{1}{\pi} P \int_{-\infty}^{\infty} \frac{\operatorname{Re} G(\omega')}{(\omega - \omega')} d\omega' \qquad 2.5.3\ (b)$$

Where P stands for the Principal value. The imaginary part and the real part are not independent and are connected by these dispersion relations. This model yields the Kramers-Kronig Relations:

$$\varepsilon_1(\omega) - 1 = \frac{2}{\pi} P_0 \int_{-\infty}^{\infty} \frac{\omega' \varepsilon_2(\omega')}{(\omega'^2 - \omega^2)} d\omega' \qquad 2.5.4\ (a)$$

$$\varepsilon_1(\omega) = -\frac{2}{\pi} P_0 \int_{-\infty}^{\infty} \frac{\varepsilon_2(\omega') - 1}{(\omega'^2 - \omega^2)} d\omega' \qquad 2.5.4\ (b)$$

The main disadvantage of this method is that there is an extrapolation beyond the measured range that is necessary to evaluate the integral. Several methods have been

proposed and are being used to confront this problem. Some of these methods have recently been analyzed by (Veszelei et al., 1994).

Another way of obtaining the dielectric function from the reflectivity is by using the factorized form of the dielectric function, (Berreman and Unterwald, 1968), and (Rytz et al., 1983). The factorized form is an improved version of the classical dispersion relation developed by (Barker and Hopfield, 1964). It allows a different damping factor for the longitudinal optic [LO] and transverse optic [TO] modes. It is especially appropriate when the LO frequency is much larger than the TO frequency, which occurs in highly ionic crystals such as SBT. It has also been derived using complex analysis in the frequency plane. The physical restrictions imposed on the poles and the zeros are discussed by (Berreman, 1963).

The factorized form of the dielectric function is the following:

$$\varepsilon(\omega) = \varepsilon_{\infty} \prod_{j} \frac{\Omega_{jLO}^{2} - \omega^{2} + i\omega\gamma_{jLO}}{\Omega_{jTO}^{2} - \omega^{2} + i\omega\gamma_{jTO}} \qquad 2.5.5$$

There is a specific frequency and damping factor for each TO and LO mode.

The factorized-form analysis was used here. The fortran program used for the fitting was developed by R. J. Gonzalez, (Gonzalez et al., 1996).

The fit obtained for the crystal data is displayed in Fig. 2.18. The TO and LO frequencies corresponding to this fit are listed below in Table 2.7. (The values have been rounded off to the nearest wavenumber, since the results are not more accurate than this.) Three TO-LO pairs were used to fit the measured spectrum, and Fig. 2.18 shows this fit to be quite successful. This success indicates that the optical anisotropy in the a-b plane of SBT is small; the E || a and E || b reflectivity spectra must be very similar. This reconfirms the "pseudotetragonal" character of the SBT structure. The

structure has been refined and found to be orthorhombic, section 2.3 (Newnham et al., 1973) with a = 5 Å, b = 5.49 Å, and c = 25.06 Å. Without this "pseudotetragonality", the fit would not have been so successful. From the factorized-form results for the crystals, we can also extract the spectra corresponding to the real and imaginary parts of the dielectric function and the refractive index. These are shown in Figs. 2.19.

Table 2.7 **The infrared reflectivity of the SBT crystal data, fitted with the factorized form of the dielectric function.**

Mode	Wavenumber cm^{-1}	Damping Factor γ
TO	230	58
LO	330	14
TO	333	16
LO	451	57
TO	612	24
LO	773	39

	$\varepsilon_{\infty}=5.5$	$\varepsilon_0=33$

2.5.3 Infrared Measurements on PLD SBT Films

The measurements on the PLD films were carried out at near-grazing incidence. At normal incidence, no signal was detected due to the small thickness of the films ($\approx$ 200 nm) as mentioned in section 2.5.1. Comparing the pellets standards at near-grazing to the film is not helpful. Figure 2.24 shows that the pellet reflectivity at near-grazing incidence has many features in common with the pellet reflectivity at normal incidence, but the reflectivity from the PLD films is rather different.

The main purpose of obtaining the crystal IR was for comparison with the IR results on the pellets and the films in this study. Table 2.8 lists the IR frequencies observed in the films of the second set and the crystal. The two higher crystal LO frequencies appear in the films.

The factorized-form analysis assumes an abrupt solid/air interface, as usual. This is not a good approximation for a pressed pellet. For the pellet, we have a rough surface layer that is essentially a graded-layer composite consisting of a depth dependent mixture of SBT and air. To treat this we use the effective medium approximation [EMA]. The method followed here is the one described in (Hopfe et al., 1993). It consists of a stack of layers of different dielectric functions. Each layer has a certain percentage of material and air. The surface layers have a larger percentage of air than the bottom layers.

Table 2.8 **Infrared frequencies in the crystal and in four films of the second set.**

LO in SBT crystal	TO in SBT crystal	FILM1 750C	FILM2 700C	FILM3 650C	FILM4 600C
	230				
330					
	333				
					421
		442	442	442	441
451					
		509 536 560	560	573.6	
	612				
		742	720	735	720
773		797	812	799	

The best results for fitting the pellet reflectivity are shown in Fig. 2.20. The spectra were simulated using an infinite bottom layer of SBT, and additional layers composed of a certain percentage of air and SBT. The fit was more successful with the additional layers ordered in a progressive way, as done in (Hopfe et al., 1993). Layers combining a certain percentage of air and SBT were created. A layer of 10% air and 90% SBT, 20% air and 80% SBT, etc. up to 100% air and 0% SBT were defined using the real and imaginary part of these two media. Different combinations were then tried to obtain the best fit. A stack of such layers, each 0.2 μm thick, gave the best fit. It is clear in Fig. 2.20 that this graded-layer model gives a reasonable fit. The total thickness of the graded layer used here is 1.8 μm.

The spectra of the films were simulated with the same EMA method and the same layers but simply arranged in a different way. As the films stand on a substrate, the properties of this medium can not be ignored as it modifies the reflectivity measurements. Aluminium data for n and k were used (Palik, 1985). For the films, the "best" fit was obtained with a non-gradual transition. A first layer of 300 nm of pure SBT with a layer of 150 nm of 10% air- 90 % of SBT, and 200 nm of 30% air 70% of SBT was the combination leading to the fit displayed in Fig. 2.21 for two films of the second set. This leads to a total film thickness of 650 nm.

The PLD SBT film thicknesses were estimated around 200 nm by ellipsometry (Vijay, 1995). Therefore the reflectivity fit obtained for the films is not very good. The fit only works for the pellet. For the films, only the strong features of SBT at 442 and 799 cm-1 are recovered.

2.5.4 Infrared Measurements on Other Aurivillius Compounds

No infrared data of SBT bulk pellets or films or modeling has been found in literature. Therefore other infrared spectra were carried out to complement the spectra of SBT films.

The spectra of compounds of the n=2 phase Aurivillius layer structure, described in section 2.2, are shown in Figs. 2.22 (a), (b). None of them differ fundamentally from SBT. The same conclusion was found in the XRD pattern comparison of SBT and SBN. Three common features seem to persist: the strong band at 465 cm-1, a shoulder more or less pronounced at 780 cm-1, and the frequency reflectivity cutoff around 800 cm-1. The main differences arise between 500 and 700 cm-1. Also quite a few difference at low energy are noticeable for compounds containing calcium.

No systematic trend is observable from the masses of the substituted elements. From the lighter to the heavier we have: Ca (20), Sr (38), Nb (41), Ba (56), Ta (73), and Pb (82). A similar analysis was followed for Raman measurements (section 2.4.2) and seem to bring more structural information.

The final results are reflectivity measurements of PLD thin films containing different bismuth concentrations. Figure 2.23 contains the spectra of PLD films deposited at 700 C, 700 mJ, 200 mT, 18000 pulses, but all with a different amount of bismuth. Included is the reflectivity of $SrBi_2Ta_{1.6}Nb_{.4}O_9$ as the Bi variation was started from this material and not SBT directly. The IR spectra were again carried out at grazing incidence using the Pt as a reference. As for the first set of temperature deposition ones, the Pt signal is quite apparent below 450 cm-1.

2.5.5 Conclusions on Infrared Characterization

This section reports the first IR measurements on SBT materials, to the best of our knowledge. Reflectivity measurements on the SBT crystal permitted us to extract the LO and TO modes with the factorized form of the dielectric function. The obtained fit was excellent, even though the measurement included two polarizations, E || a and E || b, that are in principle distinct from each other for an orthorhombic structure. This means that the a-b plane is nearly vibrationally isotropic, supporting the pseudotetragonal view of SBT's structure.

The reflectivity of the SBT crystal and pellet standards were used for comparison to results on PLD thin films. For the thin films, near-grazing incidence was necessary for detecting a signal corresponding to the film.

The FTIR method is not adequate for the study of SBT PLD films for a main reason. The near-grazing incidence necessary is not directly comparable to the standards at normal incidence. And the fit of the reflectivity of the film with the crystal data does not recover all the main features from the films. But a similar simulation is successful for the pellet. Only the main features of SBT at 440 and 790 cm-1 are recovered for the films. They correspond to the two larger LO frequencies.

2.6 Summary for PLD $SrBi_2Ta_2O_9$ Films, and Possible Future Work

An active literature can be found on SBT applications. But most of the references concentrate on the growth of films by various methods, as the research is oriented towards direct applications. Few references were found on fundamental understanding of the SBT material itself; our results were compared to them, when possible.

Little work was found connecting the study of films for applications with basic studies of SBT. In the present work, an attempt was made to connect the knowledge of the material itself to the properties of the films obtained, in this case, by laser ablation. For the first time, IR data was obtained, along with Raman results, for SBT films deposited by laser ablation.

The characterizations measurements obtained from the films provided information about their structure and composition. Single crystal results provided basic knowledge for the interpretation of the measurements obtained on polycrystalline and thin film samples. The more information we have on the structure and the basic properties of SBT, the easier it will be to judge films prepared by a selected deposition process. This study was oriented towards PLD, but some of the material in this work can also be useful for other depositions.

The x-ray analysis confirmed the SBT crystal structure present in the pellet and the films: orthorhombic, $A2_1am$. Orientation effects were also observed in the x-ray diffraction work on the films. The texture of the films varies from one film to another.

From the x-ray experiments, all the films contain some crystalline SBT. But this technique can not reveal the amount of crystalline material present. Raman on the other

hand, is sensitive to the crystalline/amorphous ratio. As no Raman signature of crystalline SBT was detected below 650 C substrate temperature, the conclusion of this study is films deposited at higher substrate temperatures have a higher percentage of crystalline SBT in the film. This is consistent with the poor observed ferroelectric properties for films grown at substrate temperatures (below 650 C).

Another factor which is revealed by the x-ray diffraction is a variable preferred orientation during the growth of the PLD films. This might also affect the ferroelectric properties. As texture effects are observed on TiO_2 PLD films as well, it might be characteristic of PLD. A specific study could be done to investigate texture effects during the growth of PLD films.

For the first time, infrared information has been reported on SBT material and especially SBT PLD thin films. The IR reflectivity on the SBT crystal was successful enough to extract the TO and LO modes polarized in the plane perpendicular to the c-axis. The infrared technique was not satisfactory to characterize the PLD SBT films in this study. The measurements had to be carried out at grazing incidence. A simple comparison of the reflectivity at grazing-incidence on the PLD films and the reflectivity pellet is not helpful. Measurements at grazing incidence are difficult to interpret.
A recovery of these measurements by fitting the SBT crystal reflectivity data was not completely successful. Only the strong features at 440 and 790 cm-1, corresponding to the two larger LO frequencies were recovered. It might be partly due to the fact that the $E \| c$ polarization was missing and that the films were oriented. The fit was much more complete for the pellet. If measurements at $E \| c$ can be later performed on crystals allowing such a measurement, it might be worth trying this technique to characterize the films at near-grazing incidence.
On the other hand, infrared transmission can be used on films deposited on a IR transparent substrate such as silicon. The TO mode at 612 cm-1 has been recovered on

On the other hand, infrared transmission can be used on films deposited on a IR transparent substrate such as silicon. The TO mode at 612 cm-1 has been recovered on spin coated SBT films of 300 nm in our IR lab. Therefore the IR results presented in this study can be used for IR transmission measurements; SBT films deposited on silicon substrate can be characterized quantitatively.

With the Raman characterization analysis, a parallel between the trend observed and the tentative ferroelectricity origins reported previously by other scientists was tried. This generate useful information for the necessary quality of the films for FRAM applications. For future work it should be remembered that Raman characterization will be ideal on these kind of films only if the samples are much thicker (at least 600 nm). Raman scattering strength is a weak phenomenon which is affected by the amount of crystalline materials. The Raman strength scattering is also affected by the fact that SBT is a highly ionic crystal which gives much weaker signal than covalent crystals.

As future work, another characterization could be suggested. The films could be deposited on substrates transparent in the visible regime. The crystal's bandgap could be measured, similarly to what has been undertaken in section 3.3 on TiO_2. This would provide a separate new characterization tool for the films. These bandgap values could also be compared with the values obtained in the thin film lab by another student on MOCVD films.

The research in the domain of FRAM, using Aurivillius layer-structure materials, is relatively new. This important application will stimulate other research and characterization on these materials, leading to a more complete understanding of their behavior. The work reported here was a small contribution to this long process, and research on these materials will continue to be carried out at Virginia Tech.

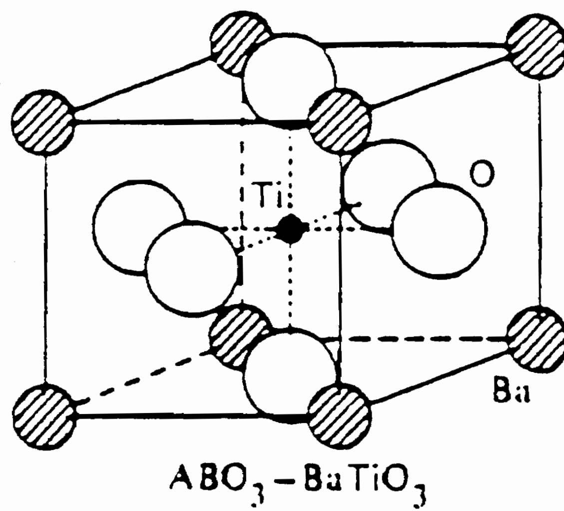

Fig. 2.1 $BaTiO_3$ structure.

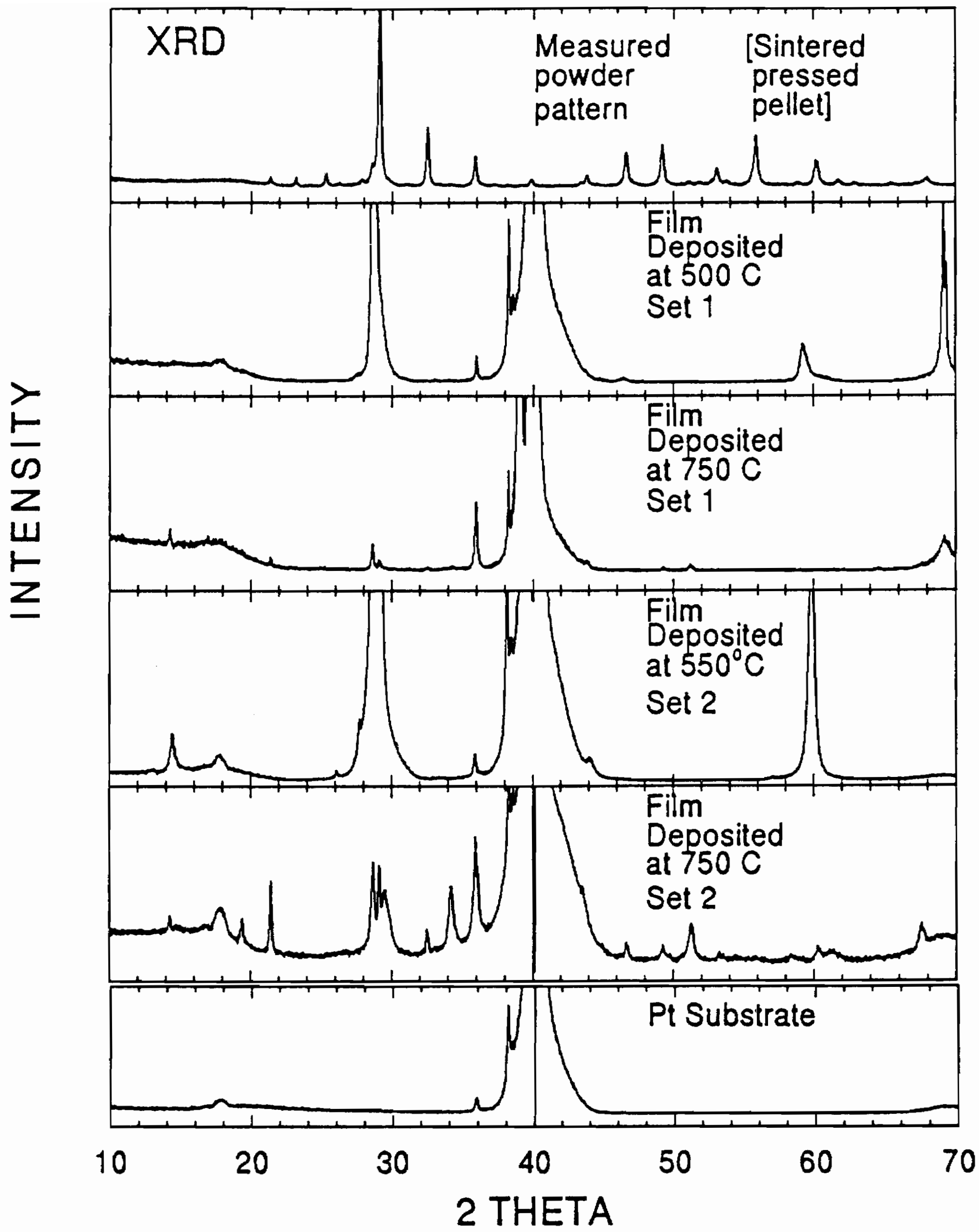

Fig. 2.2 X-ray patterns of $SrBi_2Ta_2O_9$ (SBT) thin films in normal configuration.

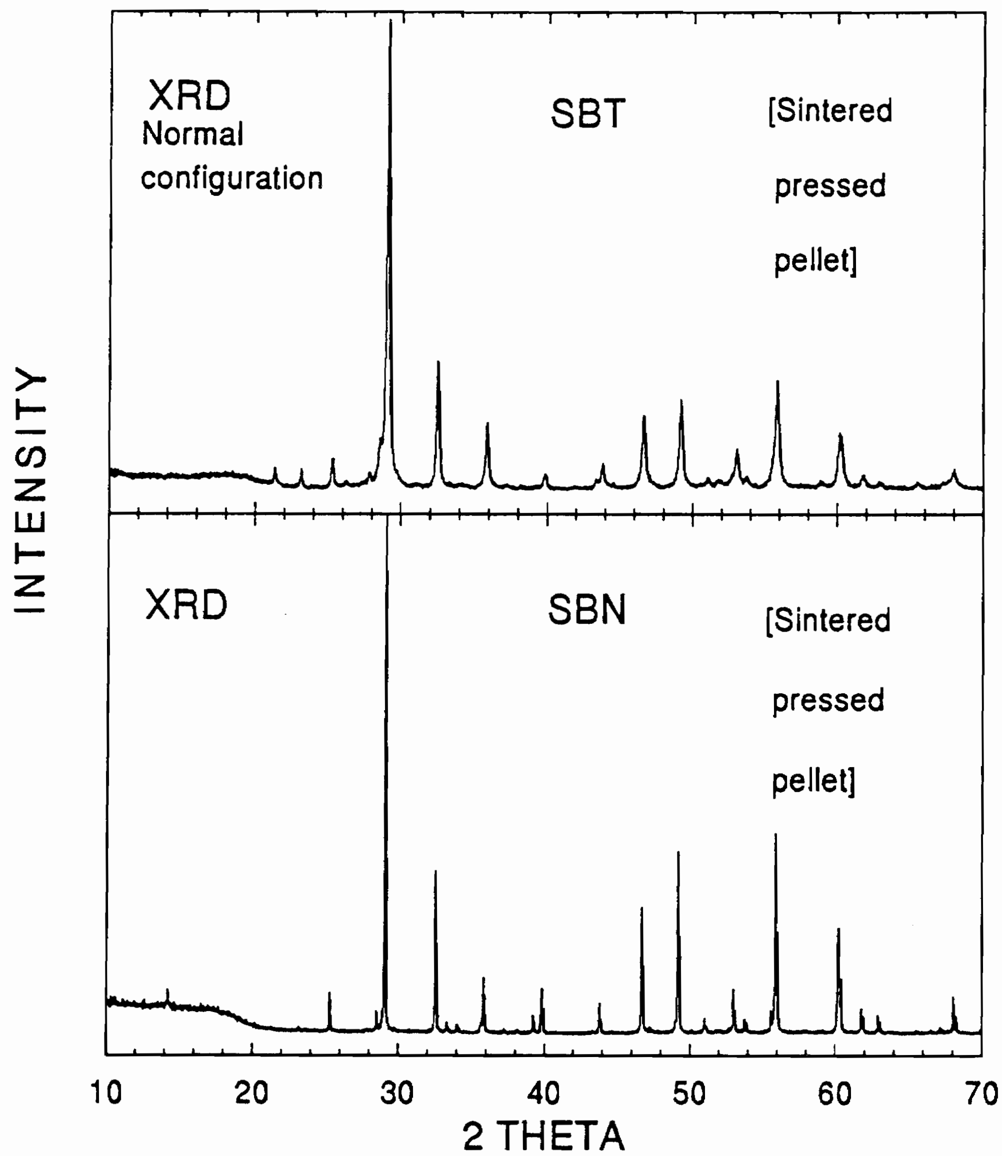

Fig. 2.3 X-ray patterns of SBT and SBN powders at normal incidence.

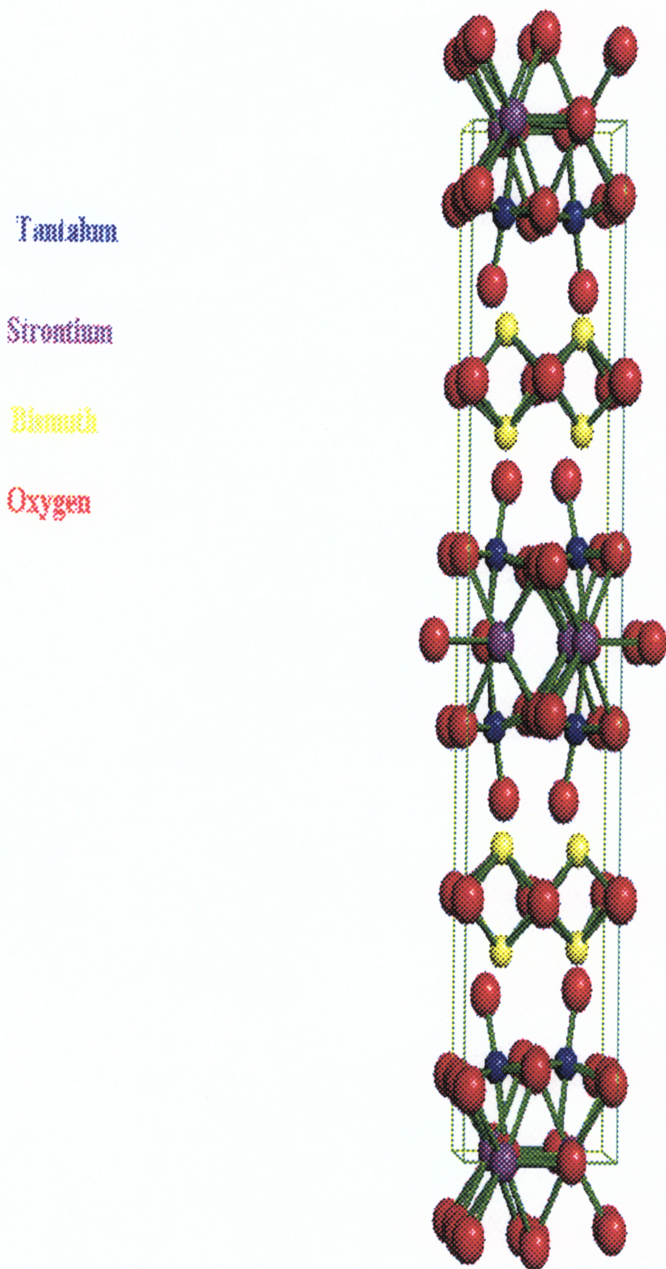

Fig. 2.4 Schematic of the SBT structure using Newnham atom positions.

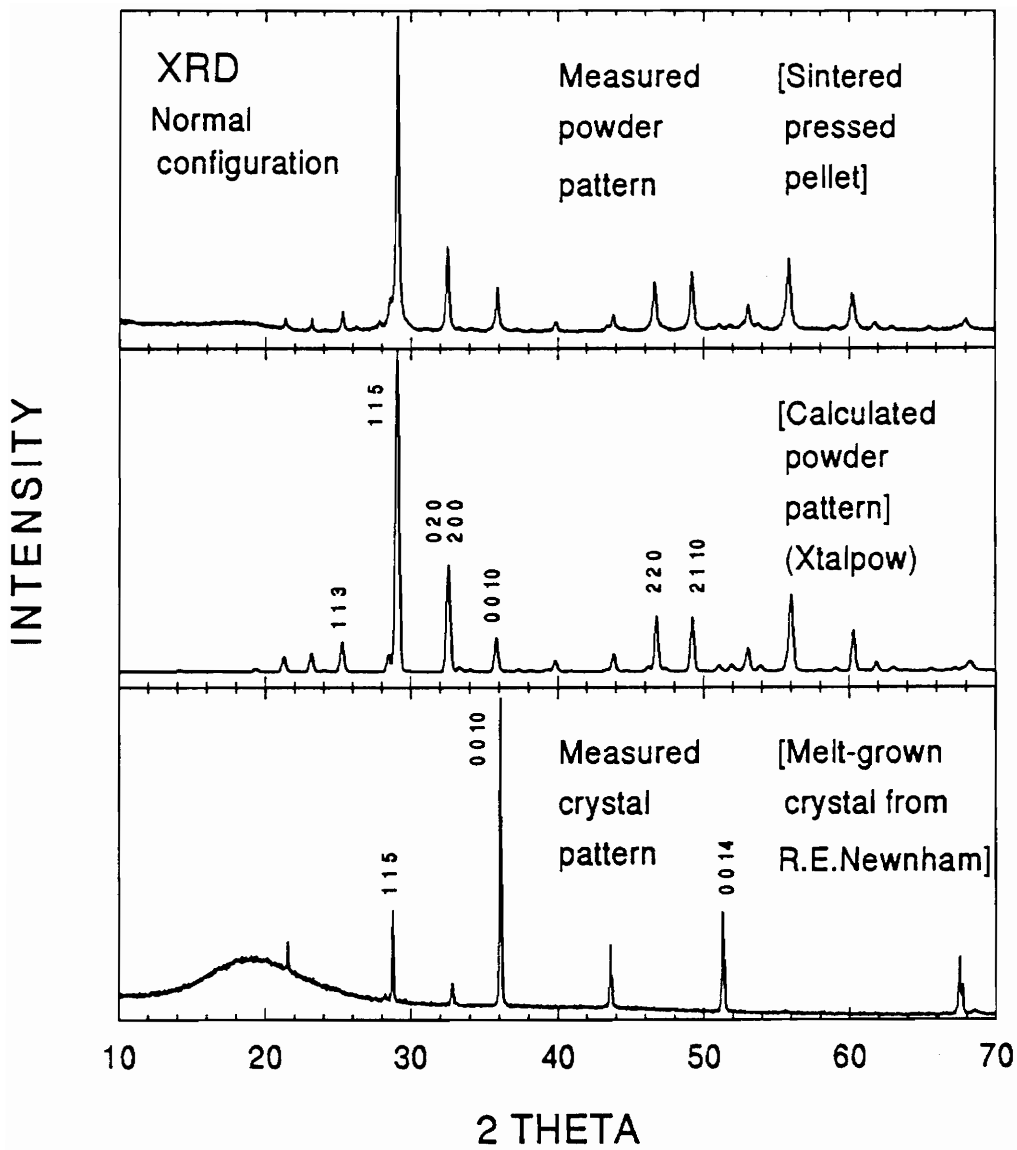

Fig. 2.5 Comparison of generated powder pattern with measured XRD patterns of SBT pellet and SBT crystal.

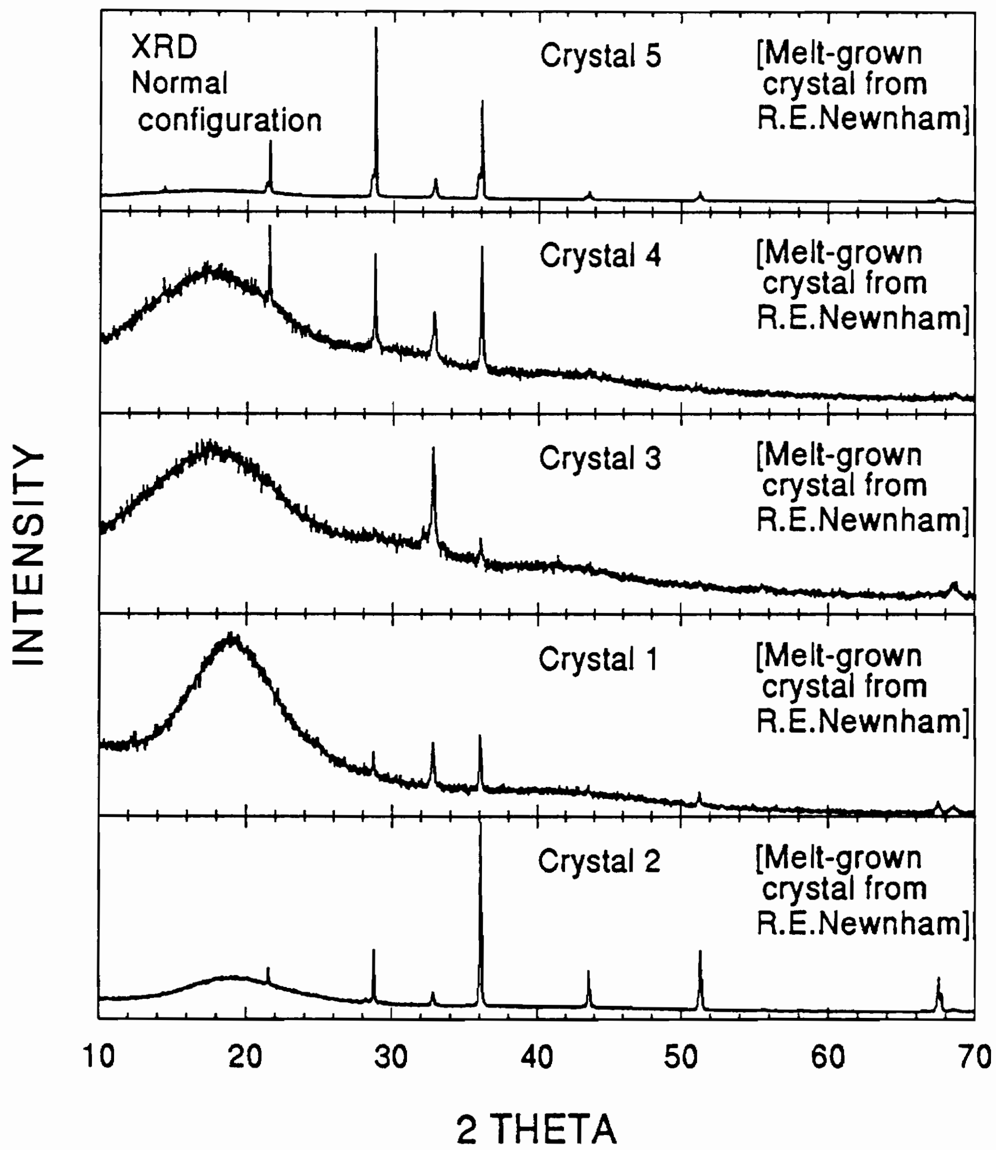

Fig. 2.6 X-ray powder patterns of SBT crystals.

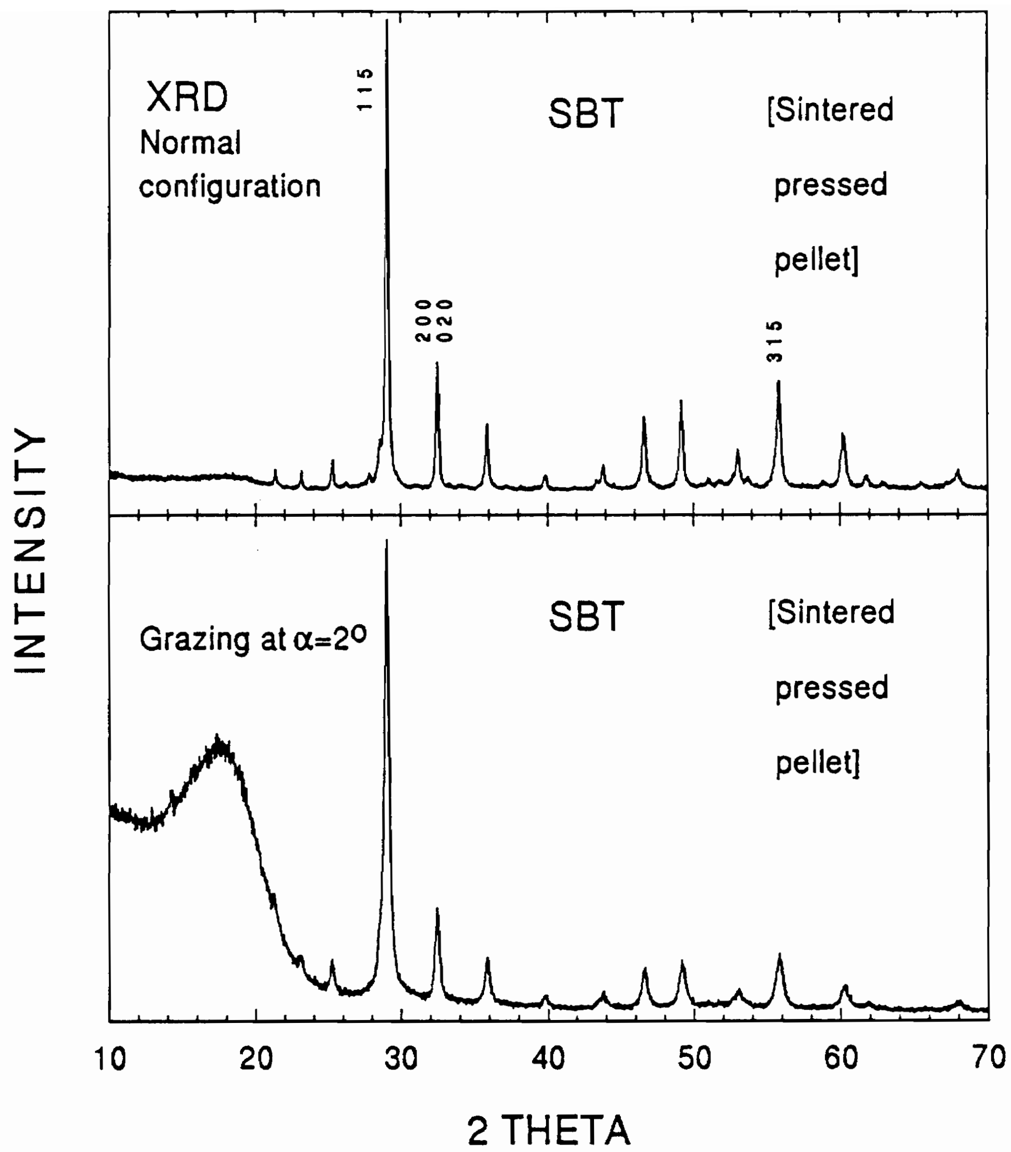

Fig. 2.7 Comparison of SBT powder at normal and grazing incidence 2°.

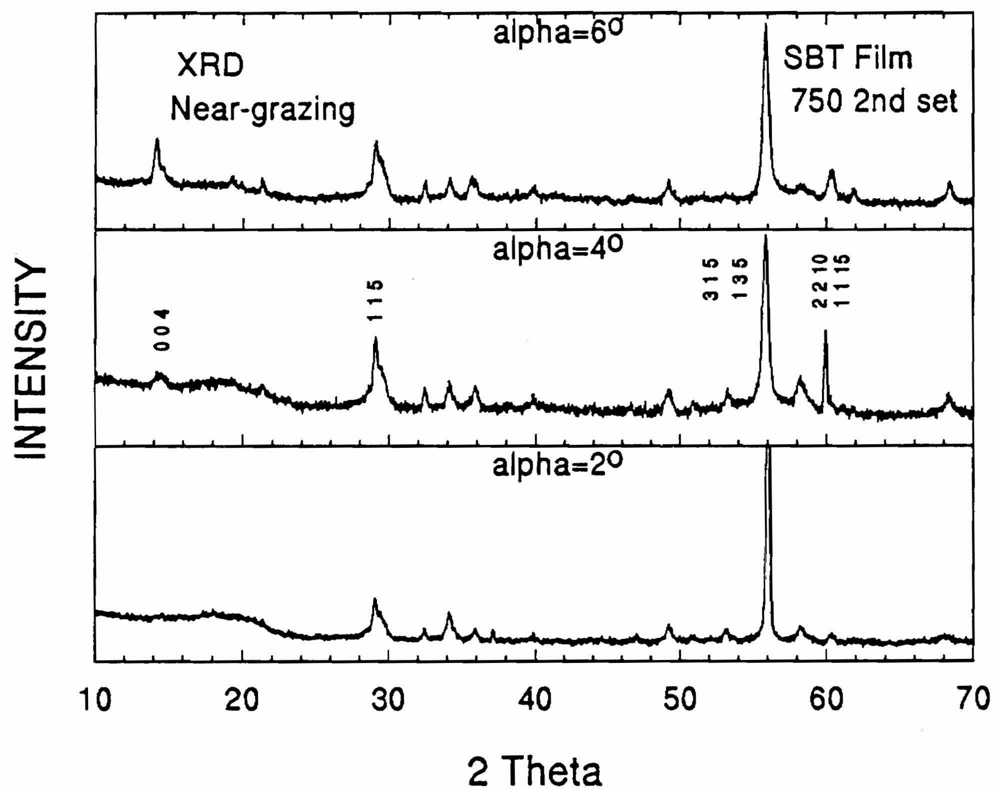

Fig. 2.8 (a) Near-grazing x-ray data on SBT thin film 750 C substrate temperature, 2nd set for various angles of incidences.

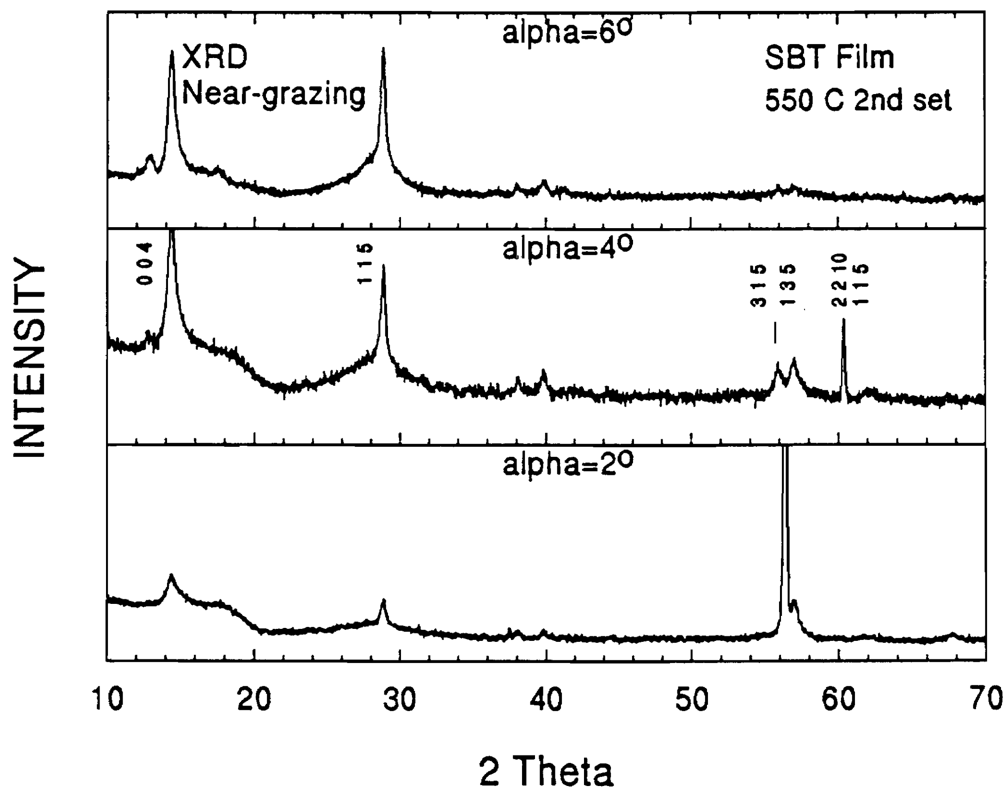

Fig. 2.8 (b) Near-grazing x-ray data on SBT thin film 550 C substrate temperature, 2nd set for various angles of incidences.

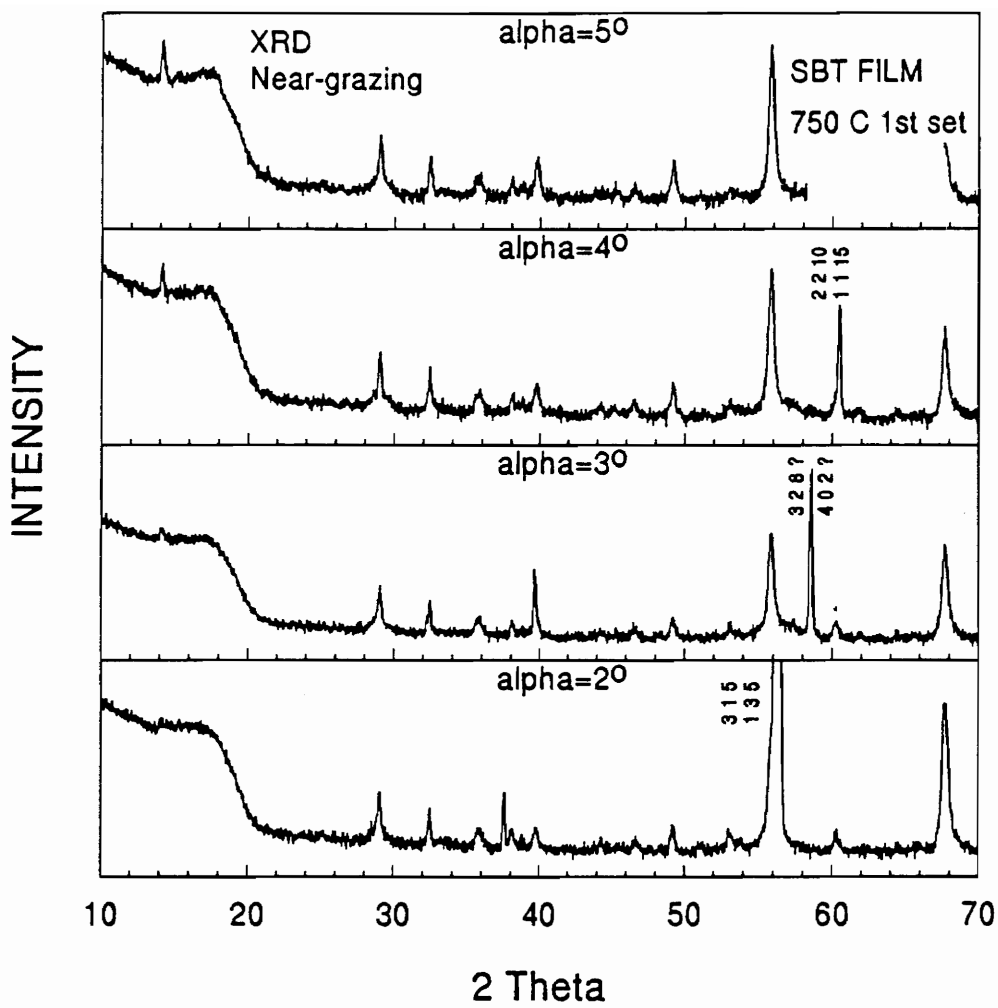

Fig. 2.8 (c) Near-grazing x-ray data on SBT thin film 750 C substrate temperature, 1st set for various angles of incidence.

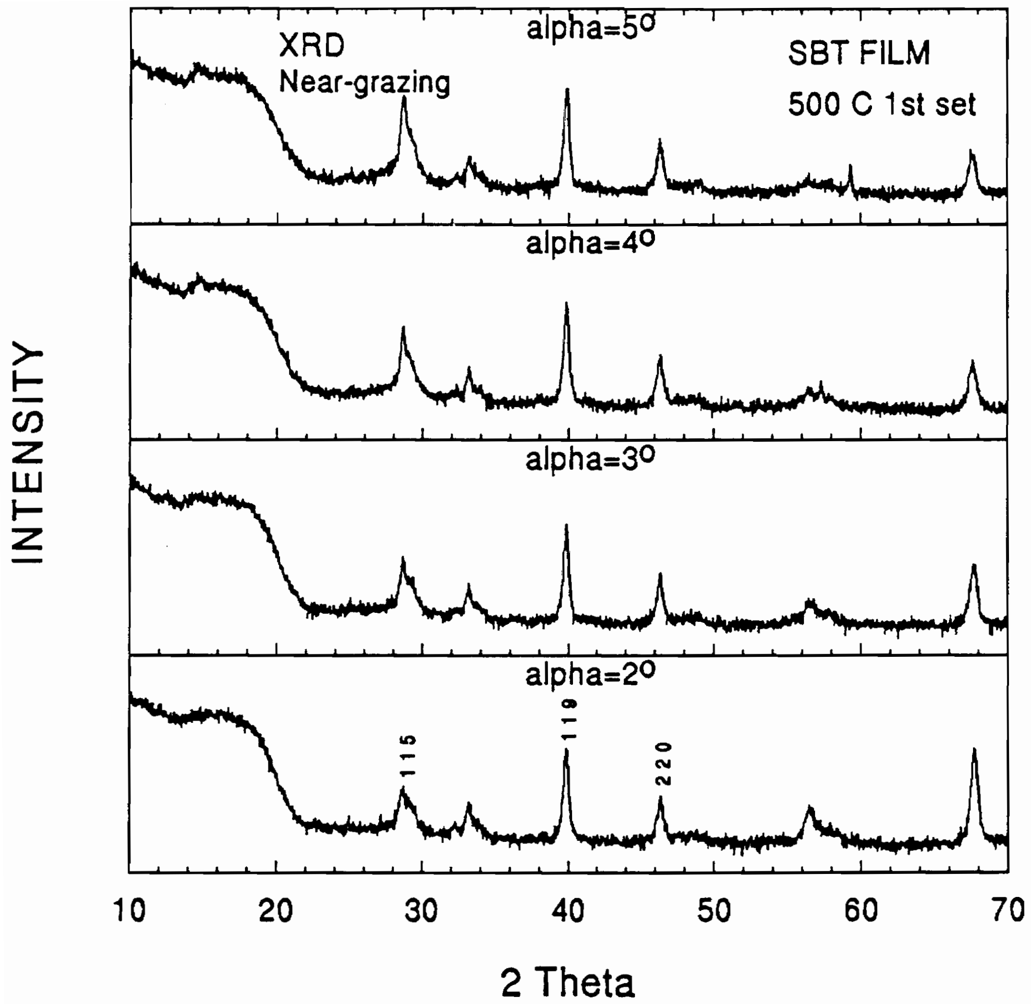

Fig. 2.8 (d) Near-grazing x-ray data on SBT thin film 500 C substrate temperature, 1st set for various angles of incidence.

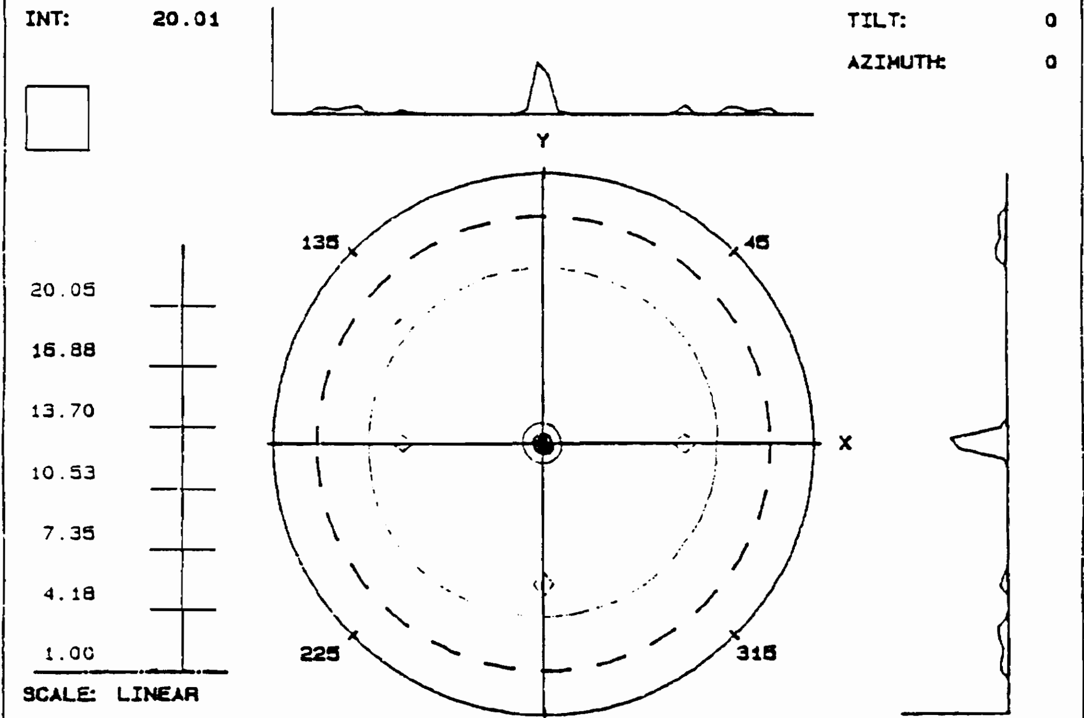

Fig. 2.9 Pole figure on the 500 C 1st set SBT thin film at 29°.

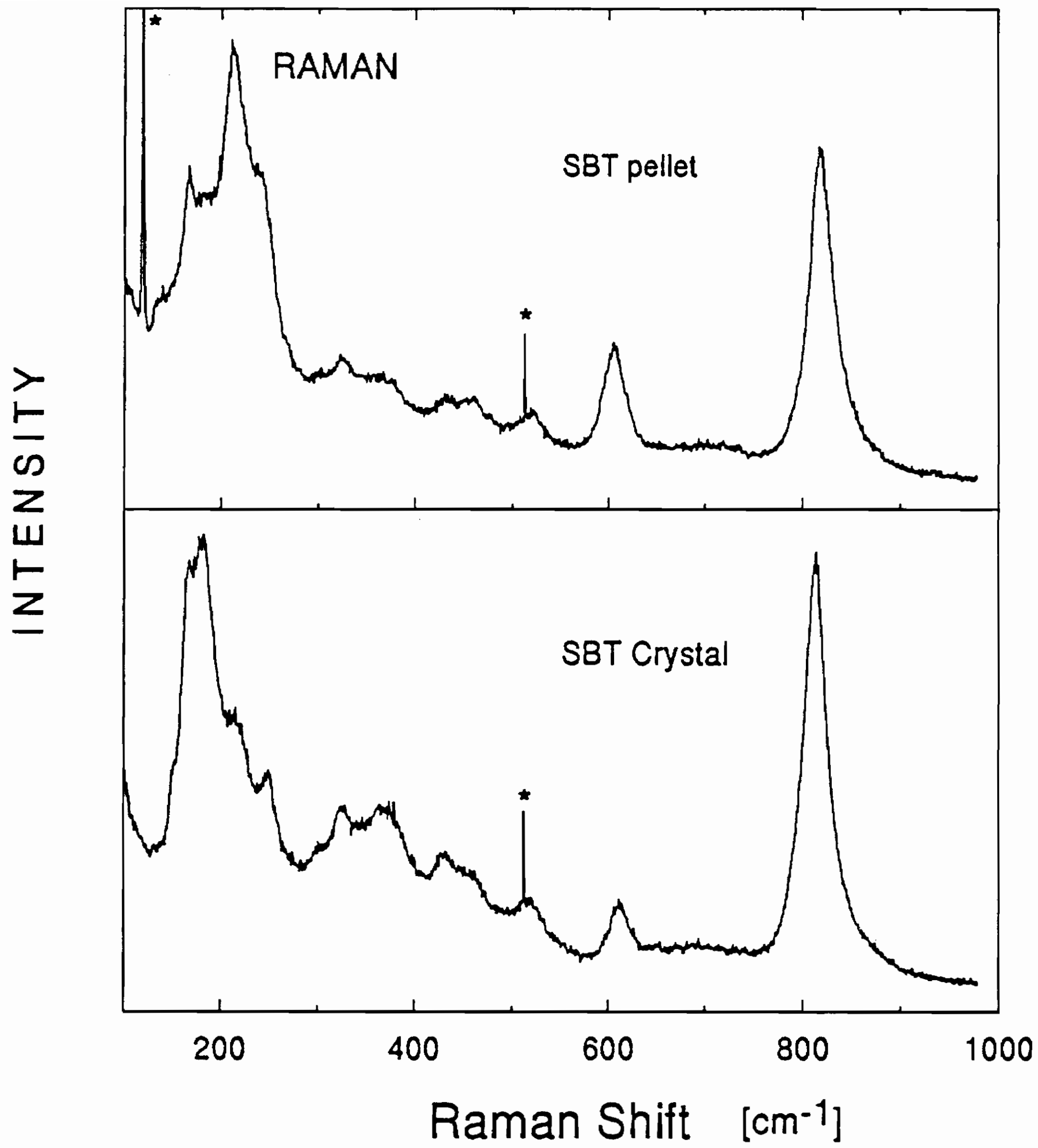

Fig. 2.10 Raman spectra of the SBT pellet and the SBT crystal.

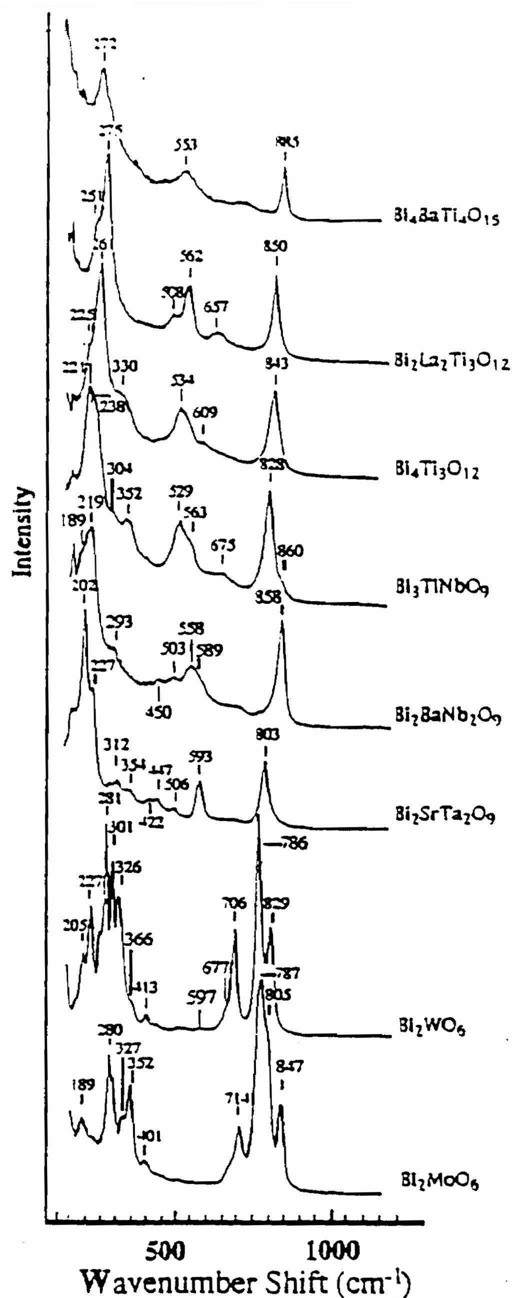

Fig. 2.11 Reported Raman spectra for n=1,2,3, and 4 Aurivillius phases for powder specimens at ambient temperature (Graves et al., 1995).

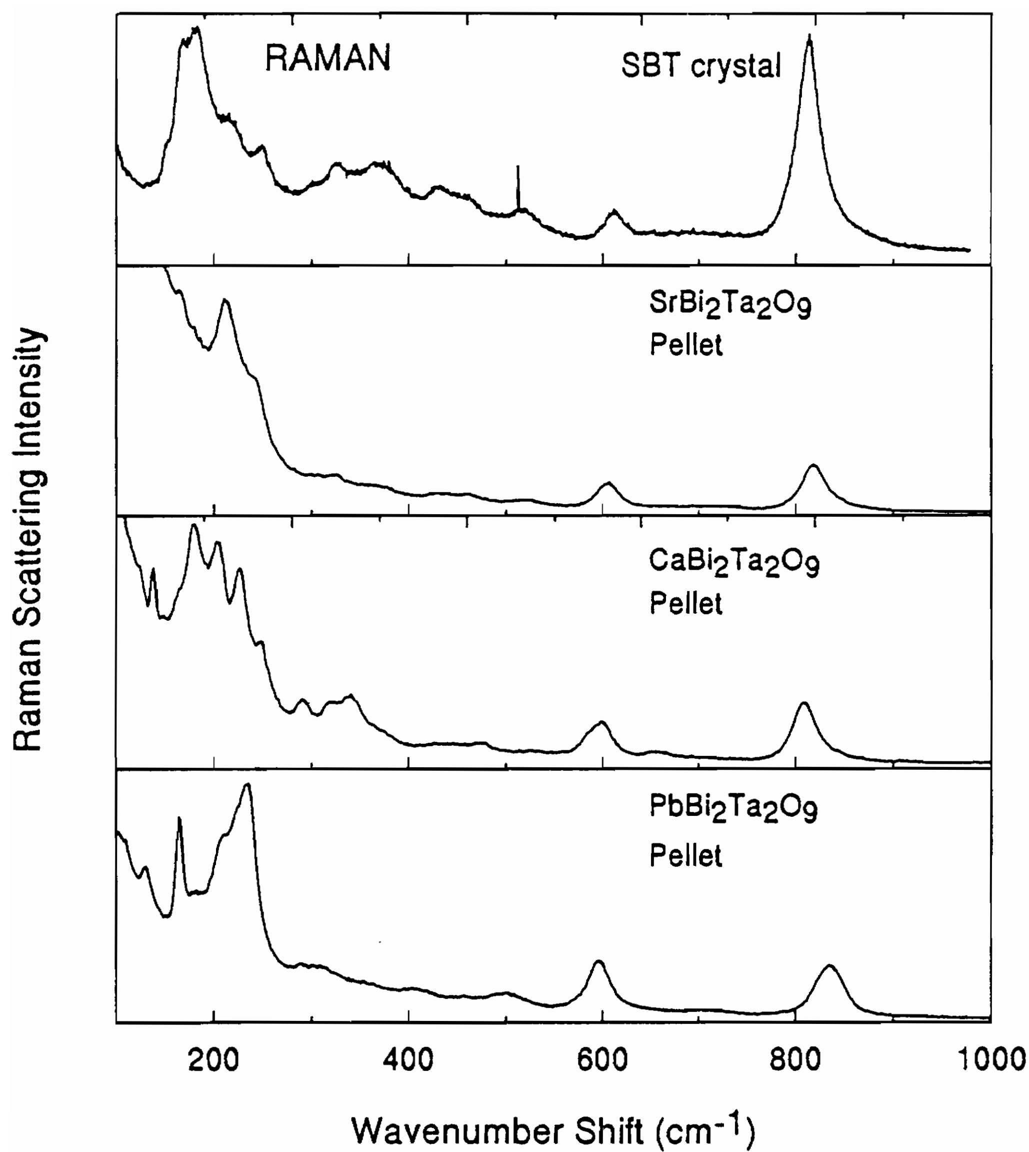

Fig. 2.12(a) Raman spectra of the tantalum-compounds.

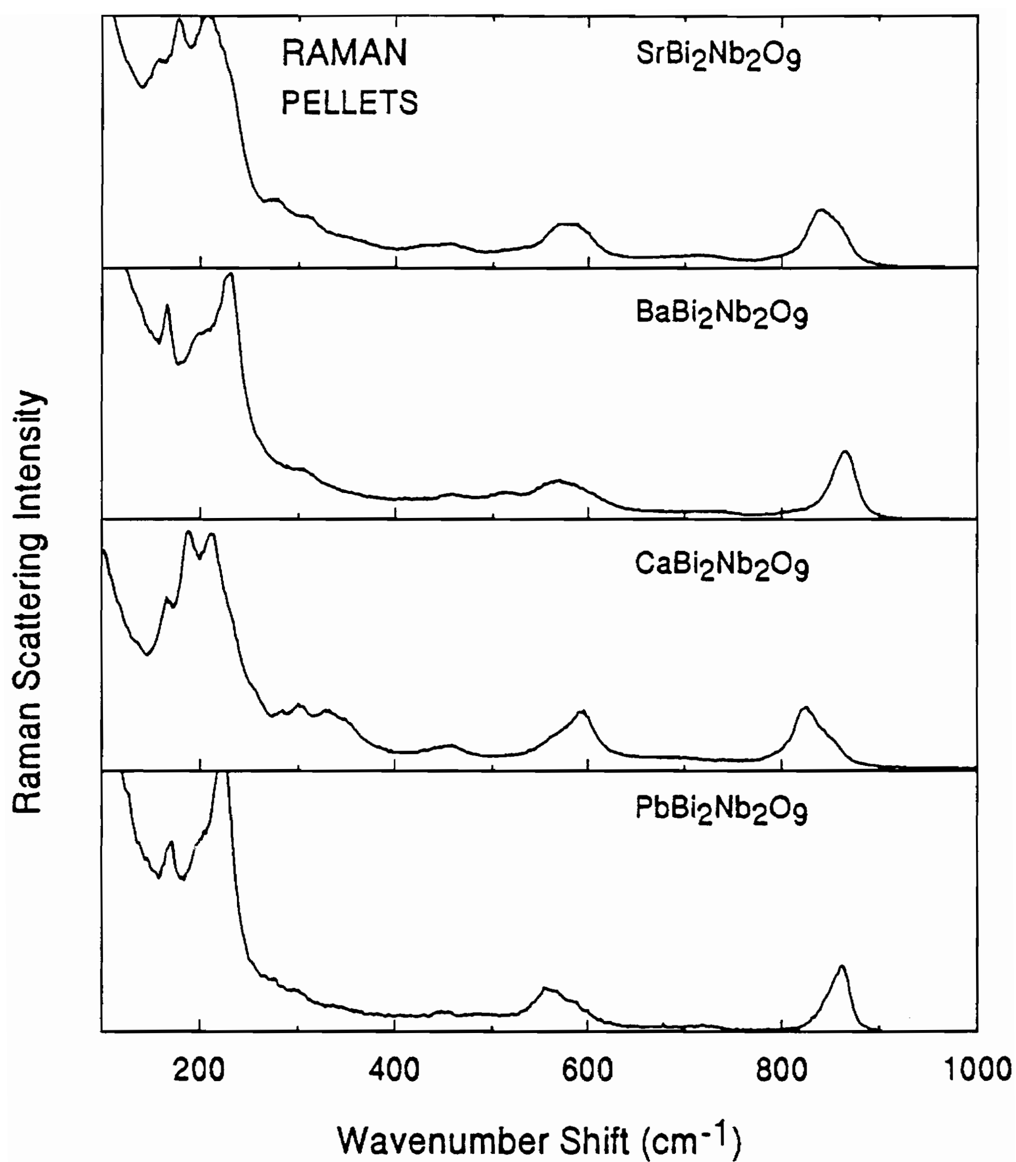

Fig. 2.12(b) Raman spectra of the niobium-compounds.

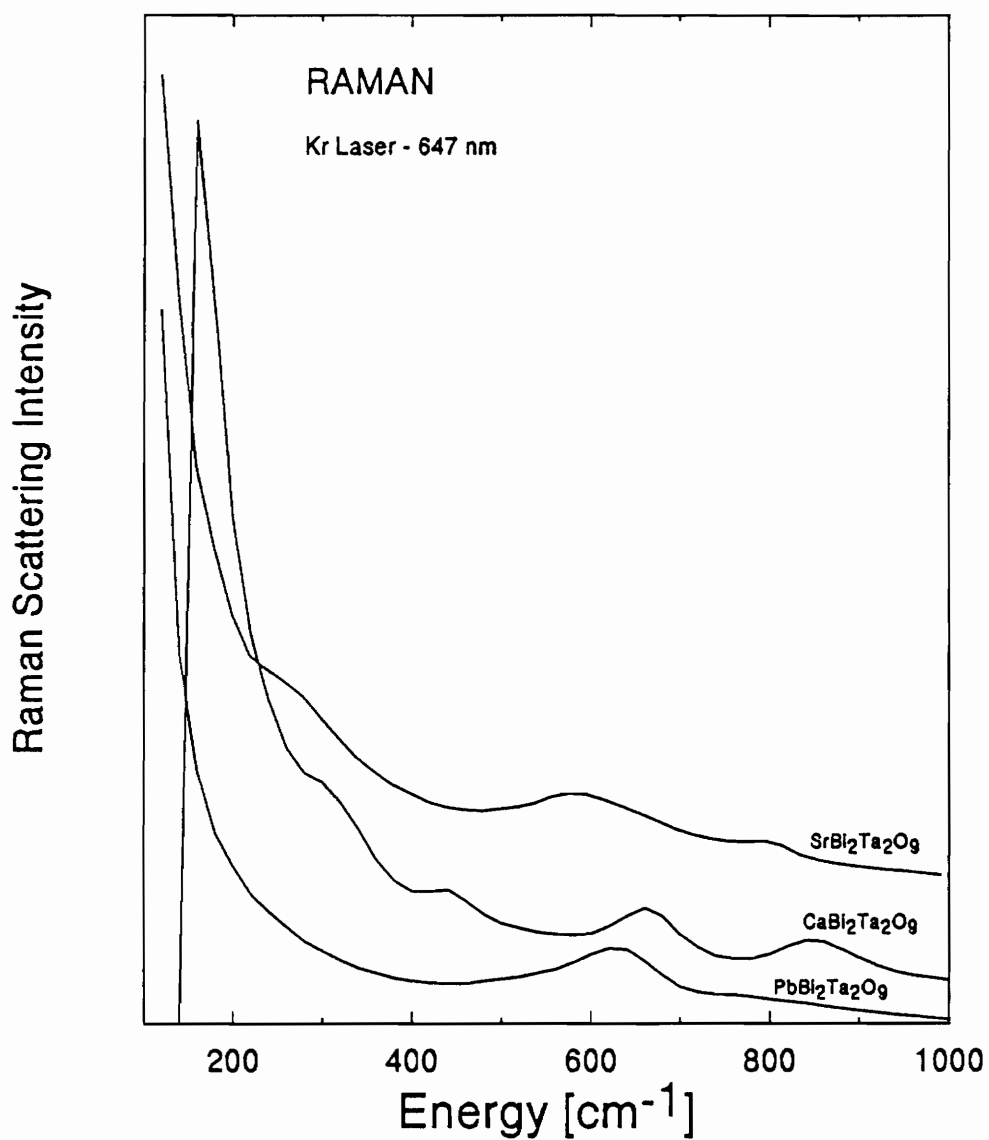

Fig. 2.13(a) Raman spectra of the tantalum-compounds at low energy.

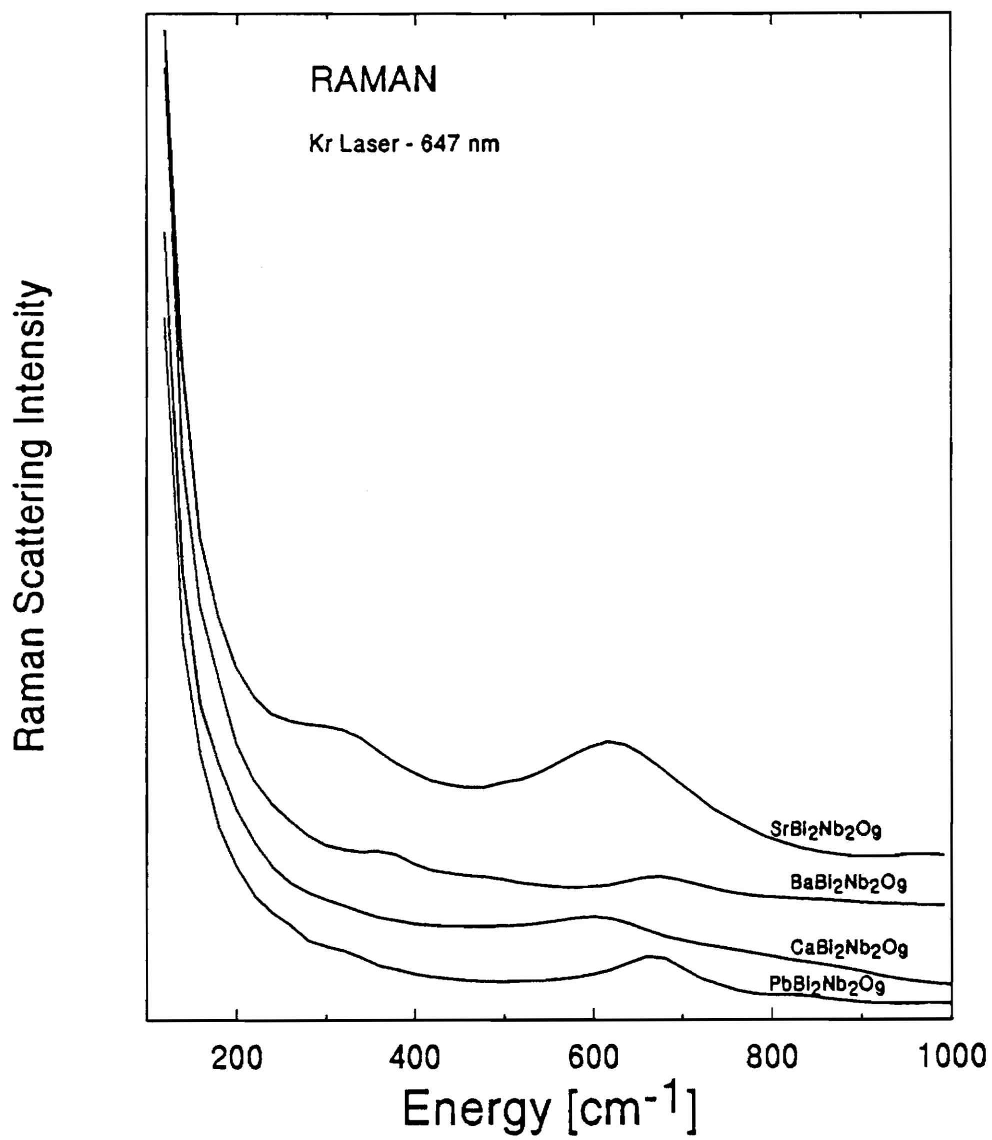

Fig. 2.13(b) Raman spectra of the niobium-compounds at low energy.

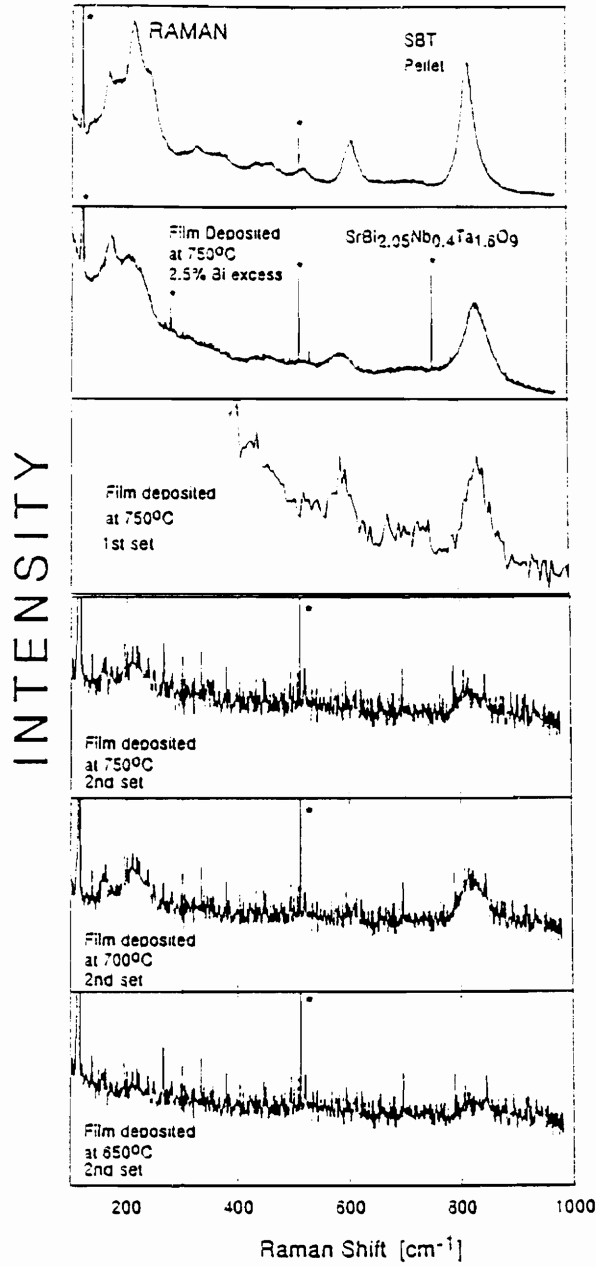

Fig. 2.14 Raman spectra of the PLD $SrBi_2Ta_2O_9$ films.

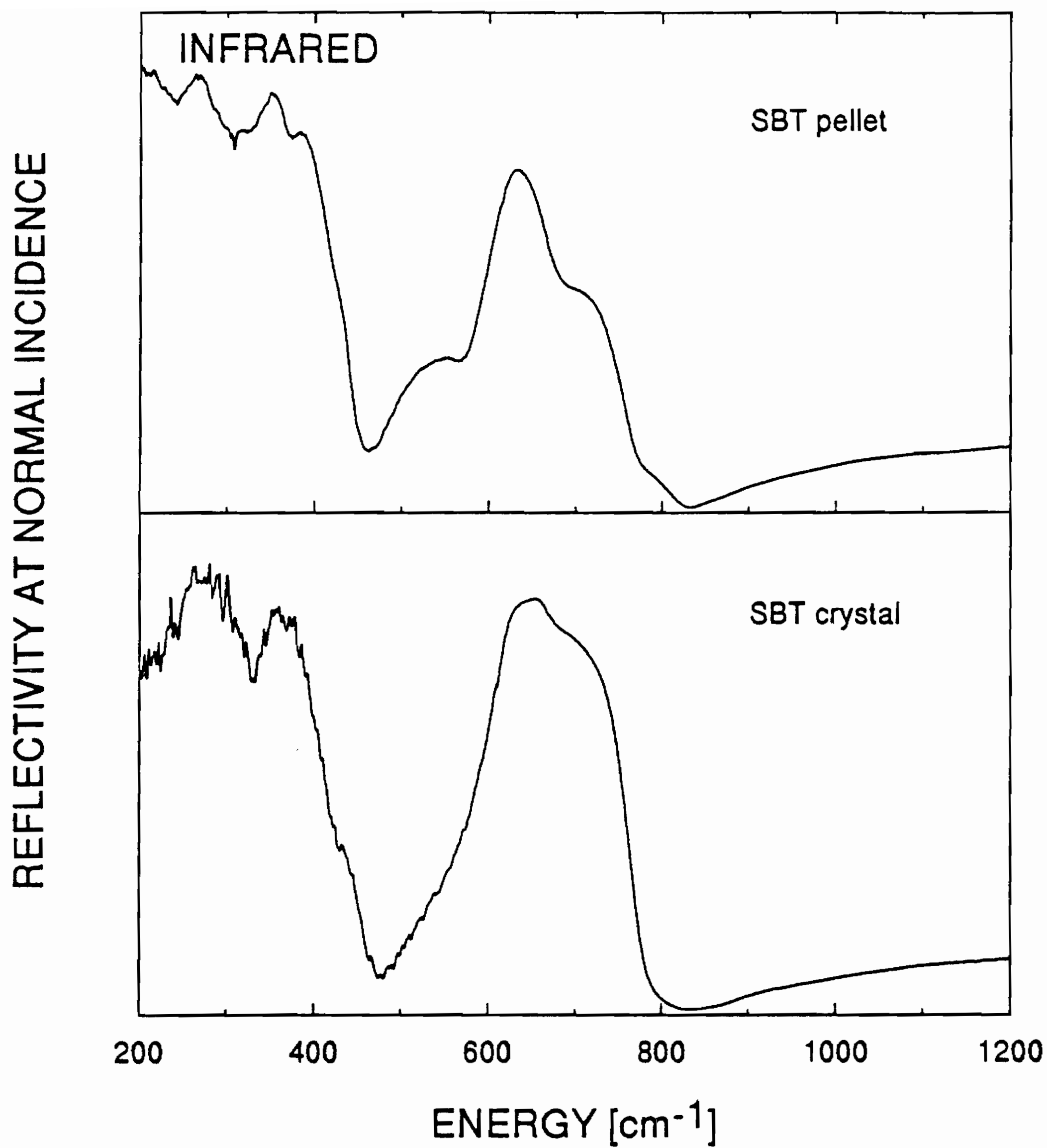

Fig. 2.15 Infrared reflectivity at normal incidence on SBT pellet and SBT crystal.

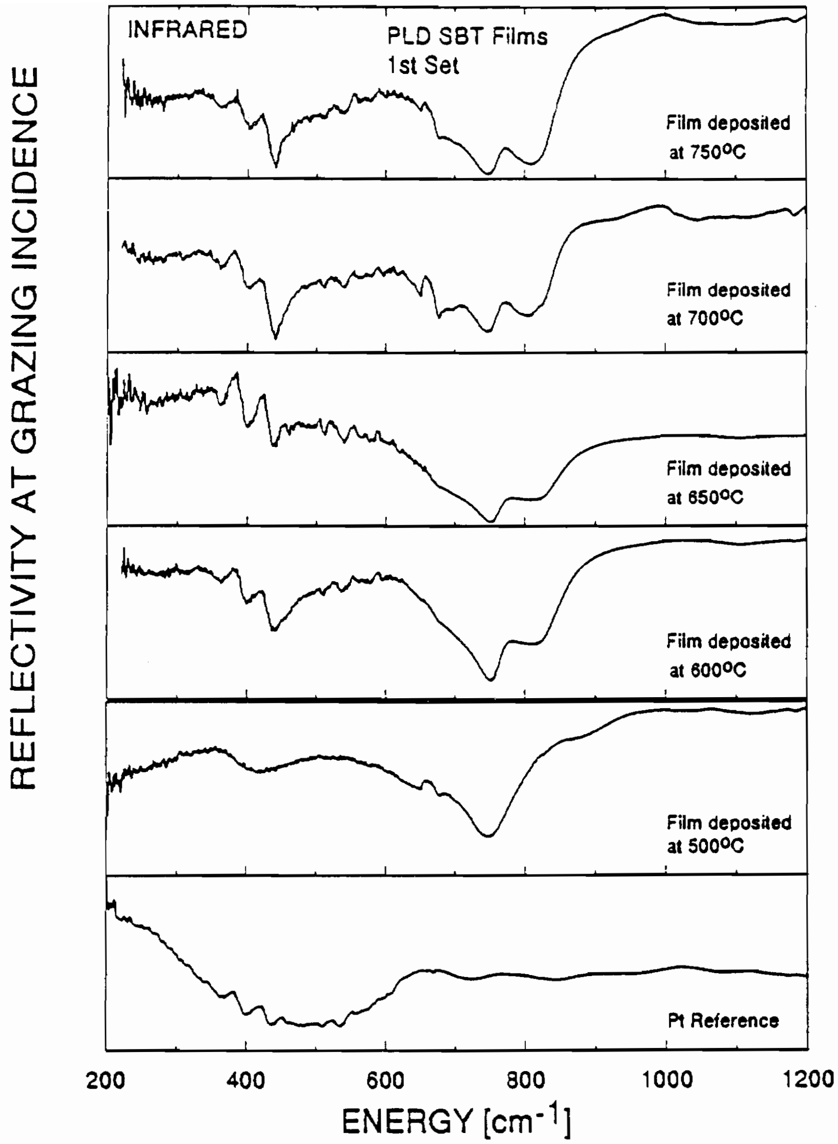

Fig. 2.16 Infrared reflectivity at grazing incidence on the SBT 1st set of films.

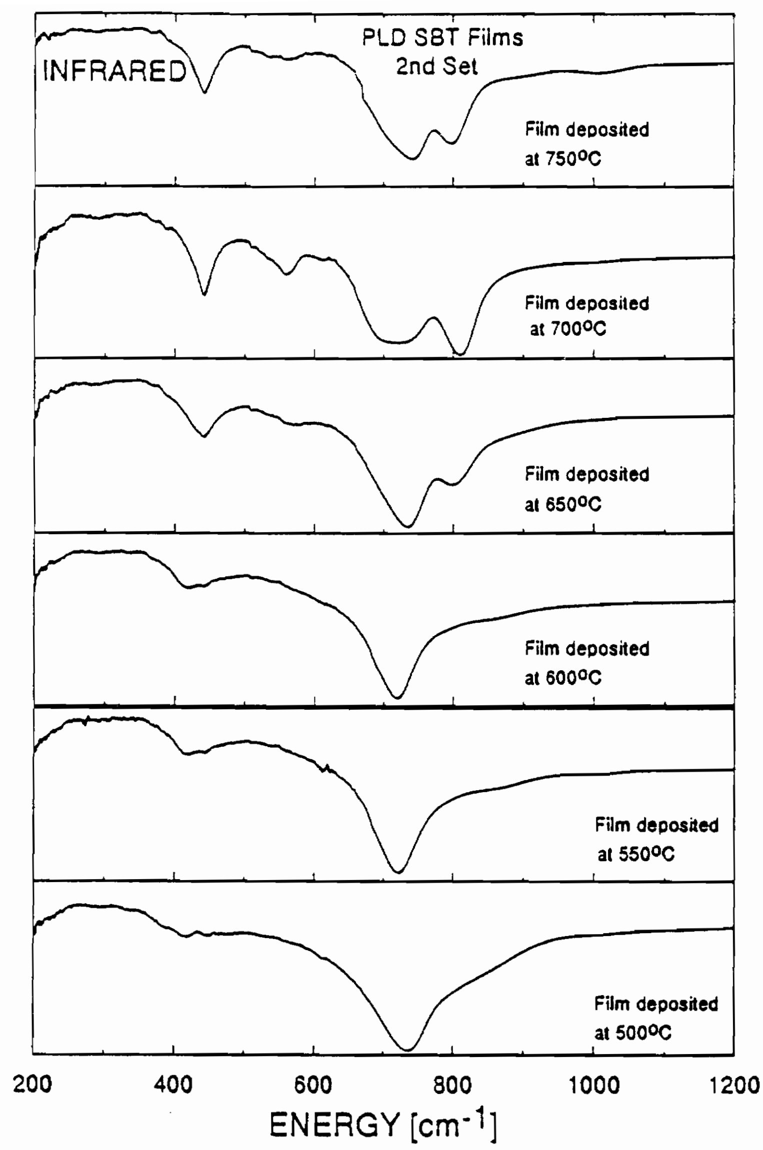

Fig. 2.17 Infrared reflectivity at grazing incidence on the SBT 2nd set of films.

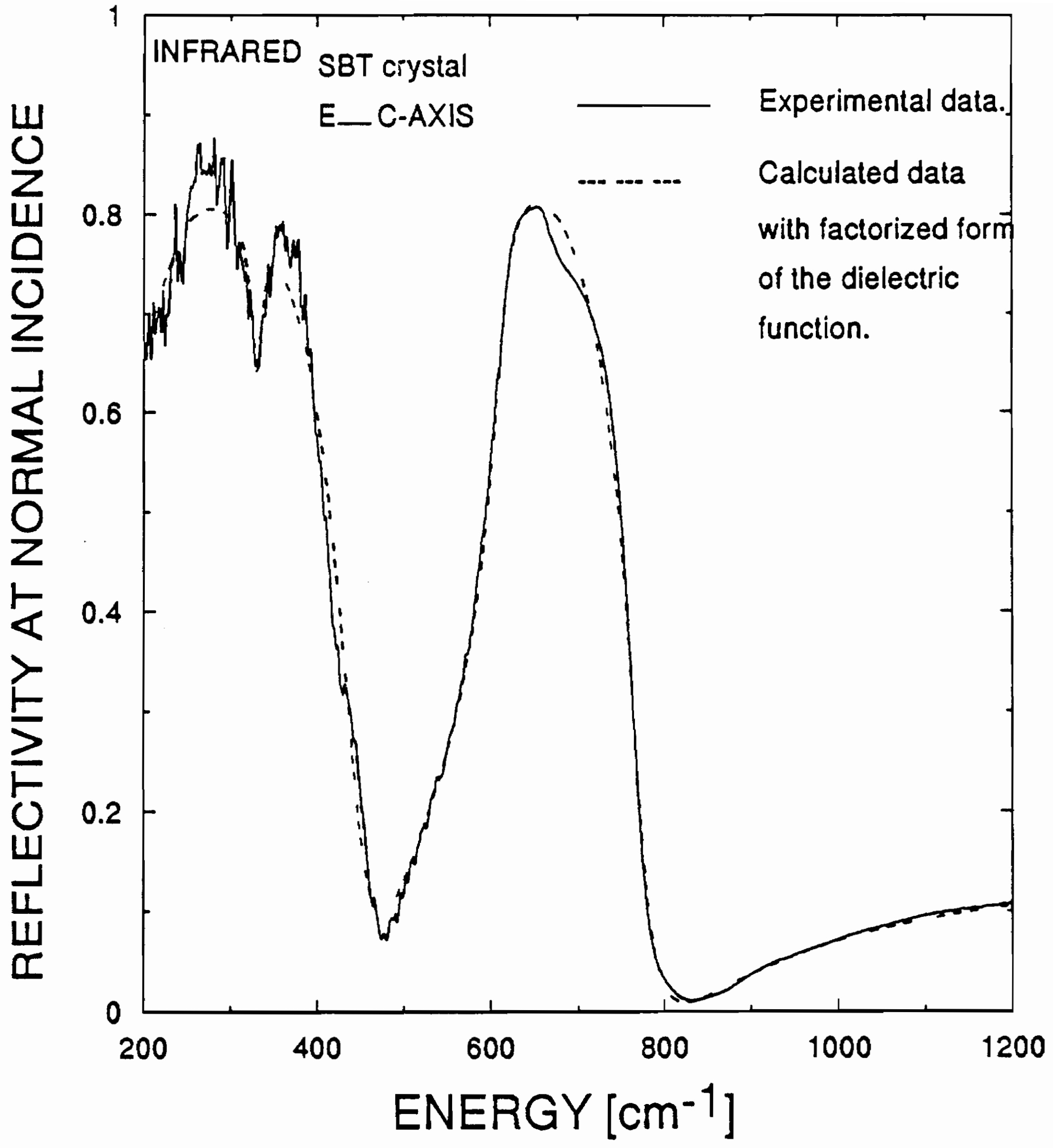

Fig. 2.18 Factorized form of the dielectric function fit of the SBT crystal infrared reflectivity.

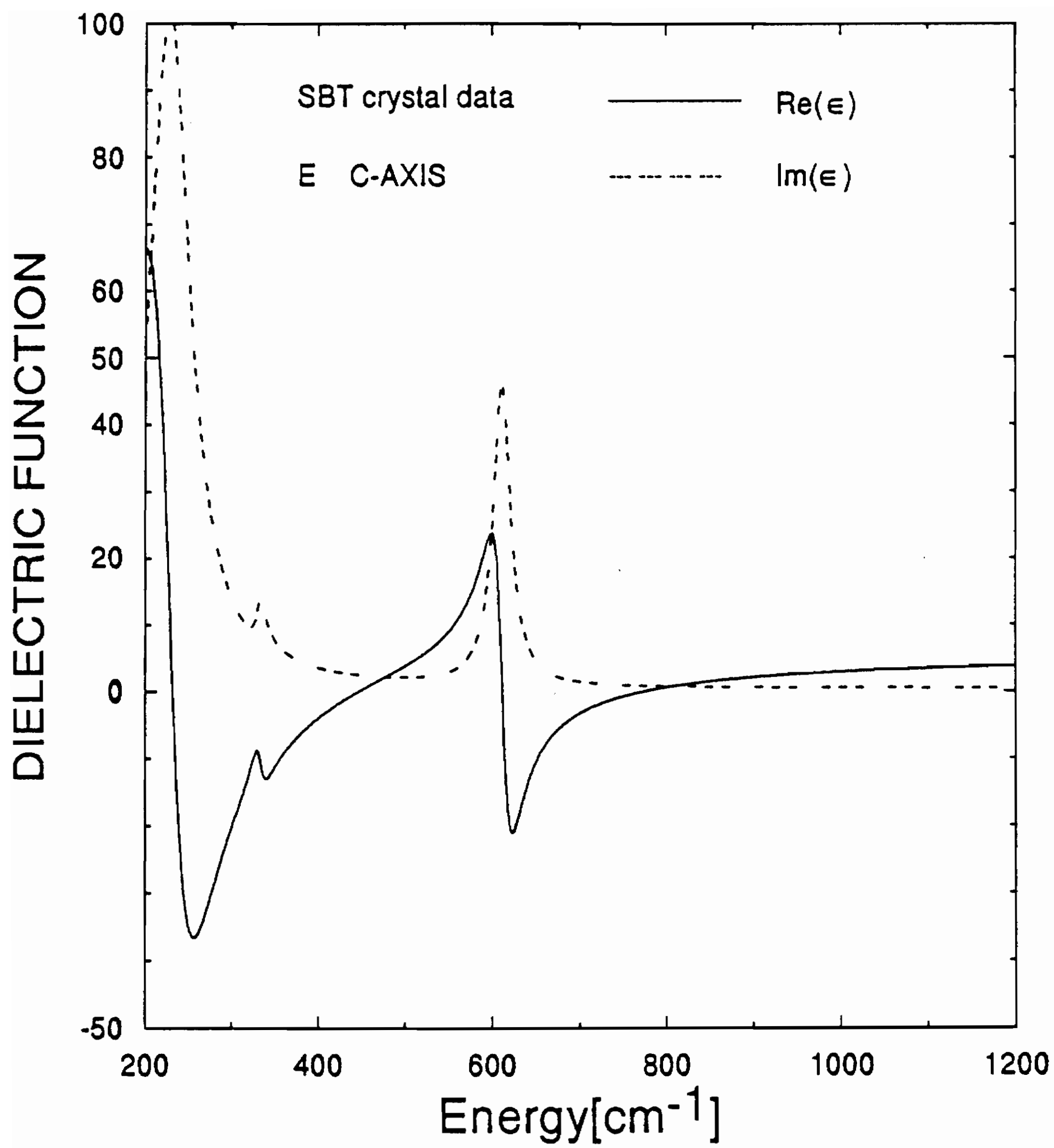

Fig. 2.19 (a) Dielectric constants extracted from the fit.

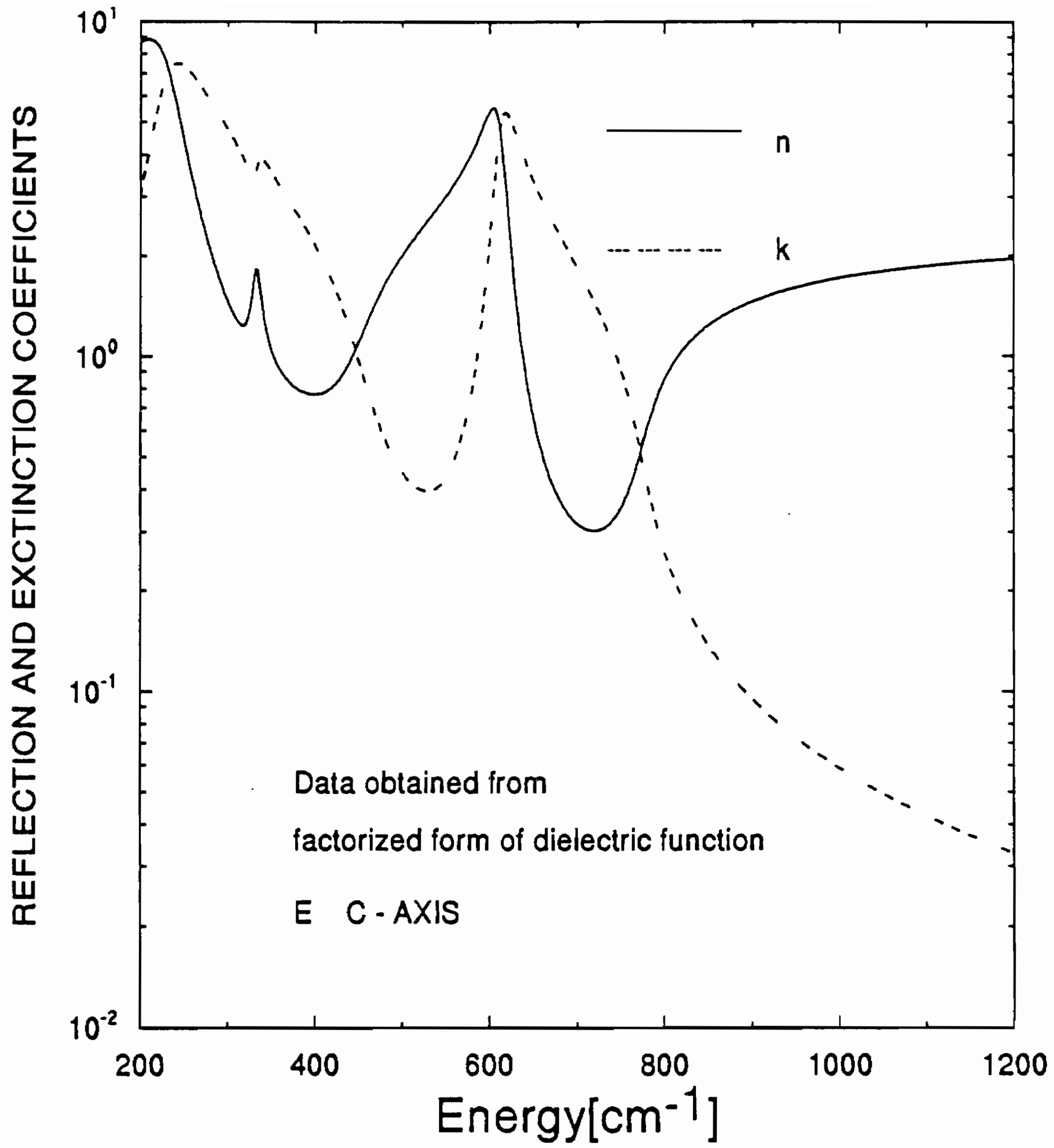

Fig. 2.19 (b) Refractive index and extinction coefficient extracted from the fit.

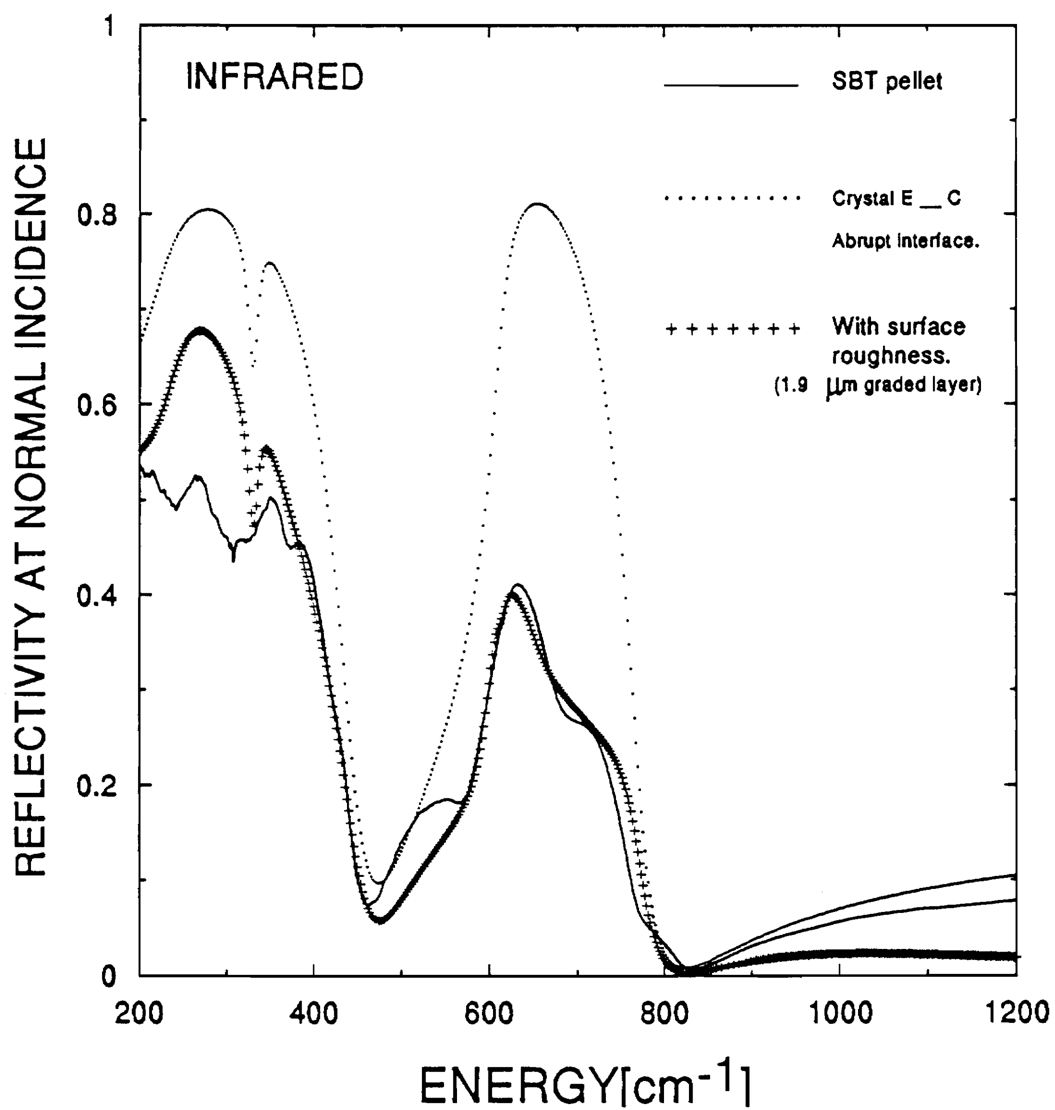

Fig. 2.20 Simulation of the pellet reflectivity data using the results from crystal fit.

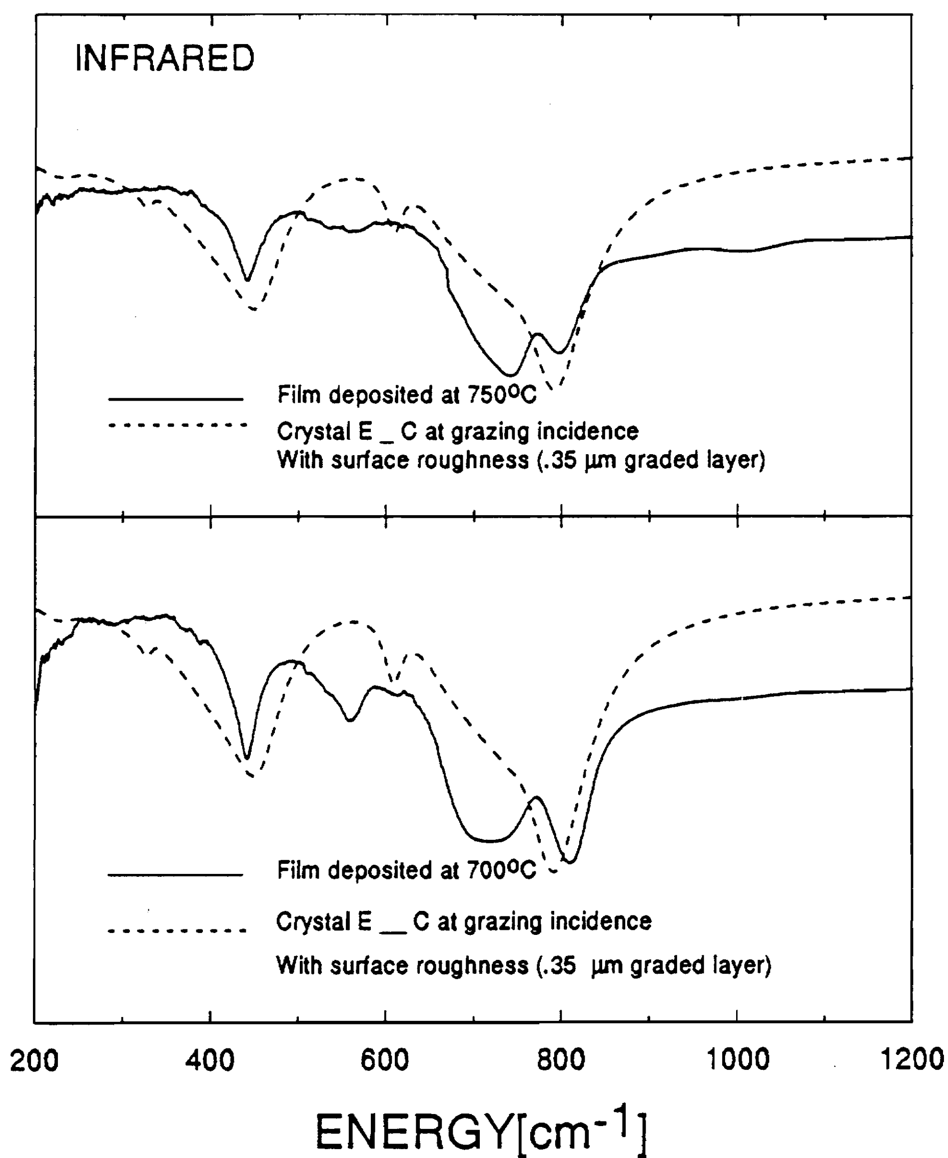

Fig. 2.21 Simulation of the film reflectivity data using the results from crystal fit.

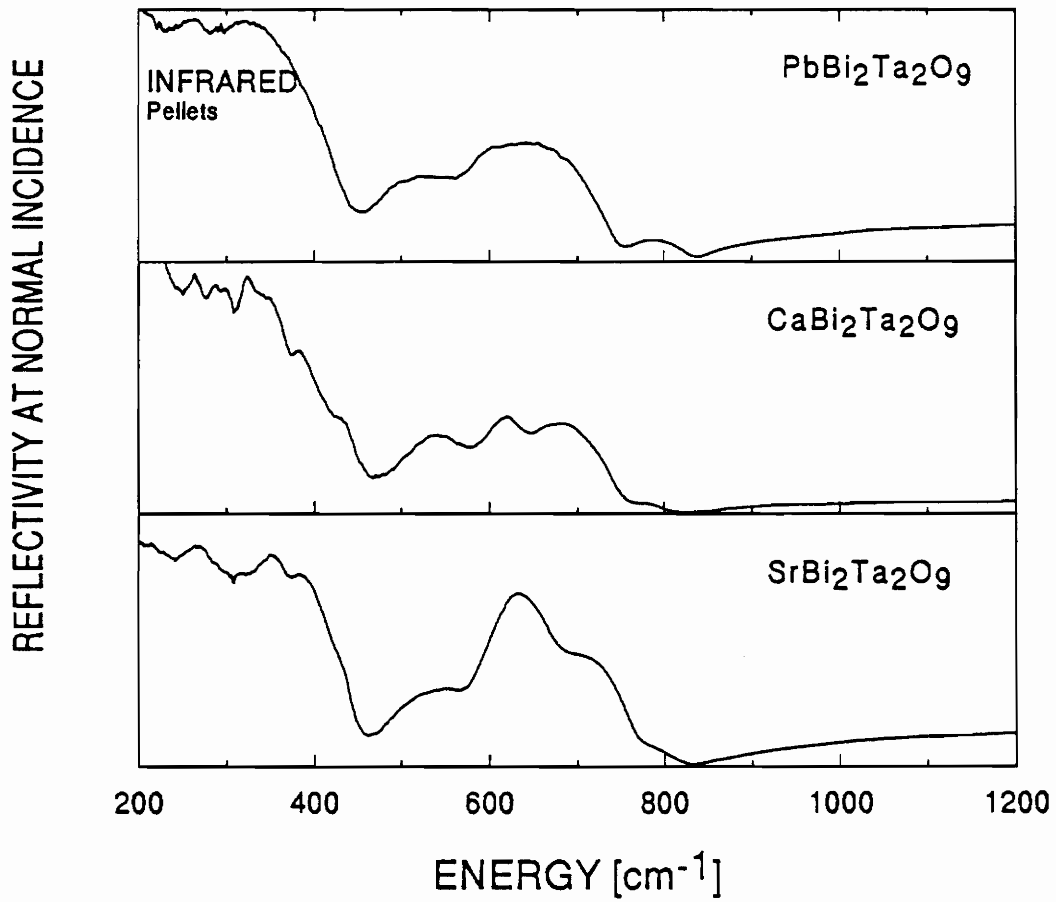

Fig. 2.22 (a) Infrared reflectivity of the tantalum-compounds family.

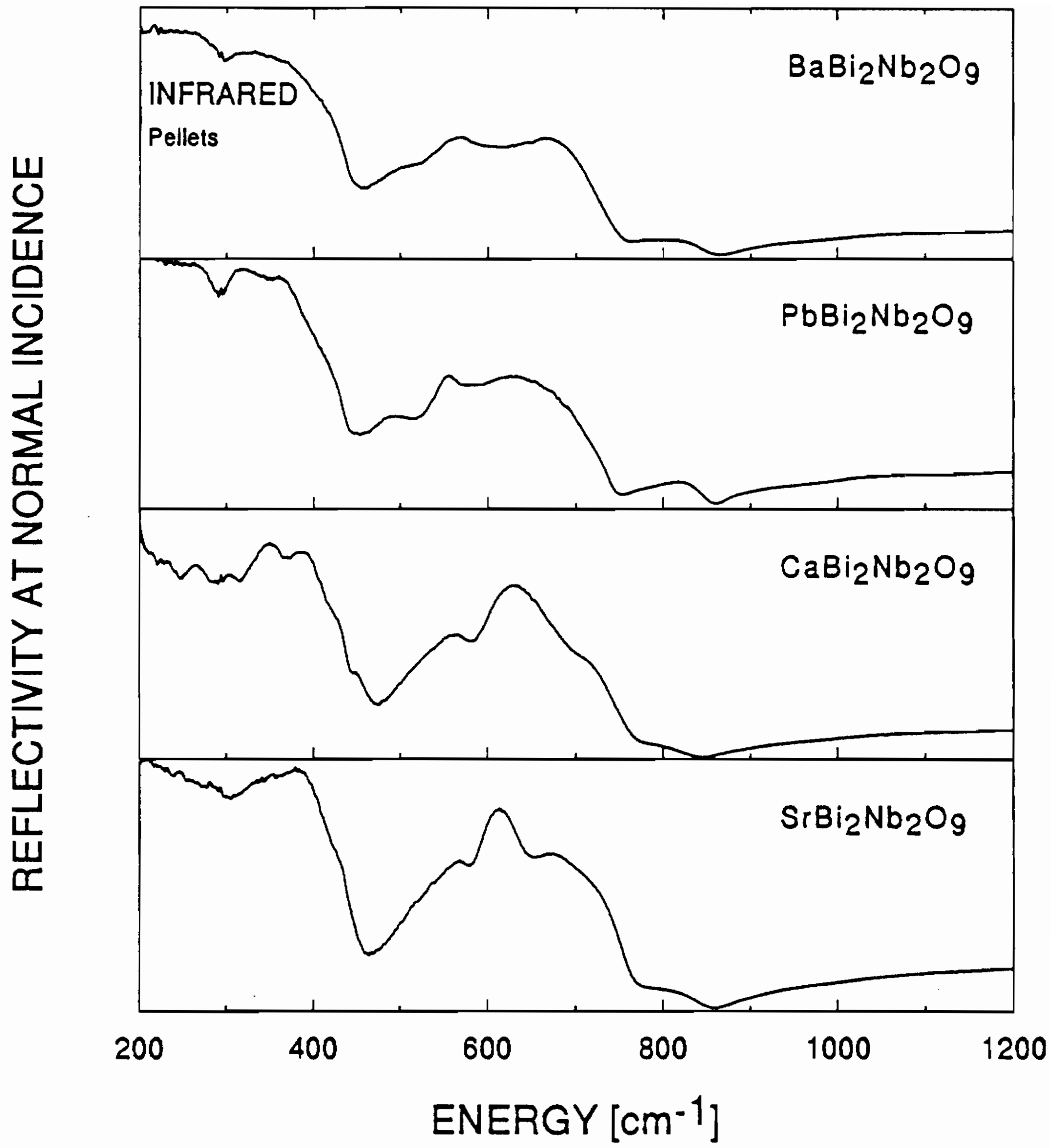

Fig. 2.22 (b) Infrared reflectivity of the niobium-compounds family.

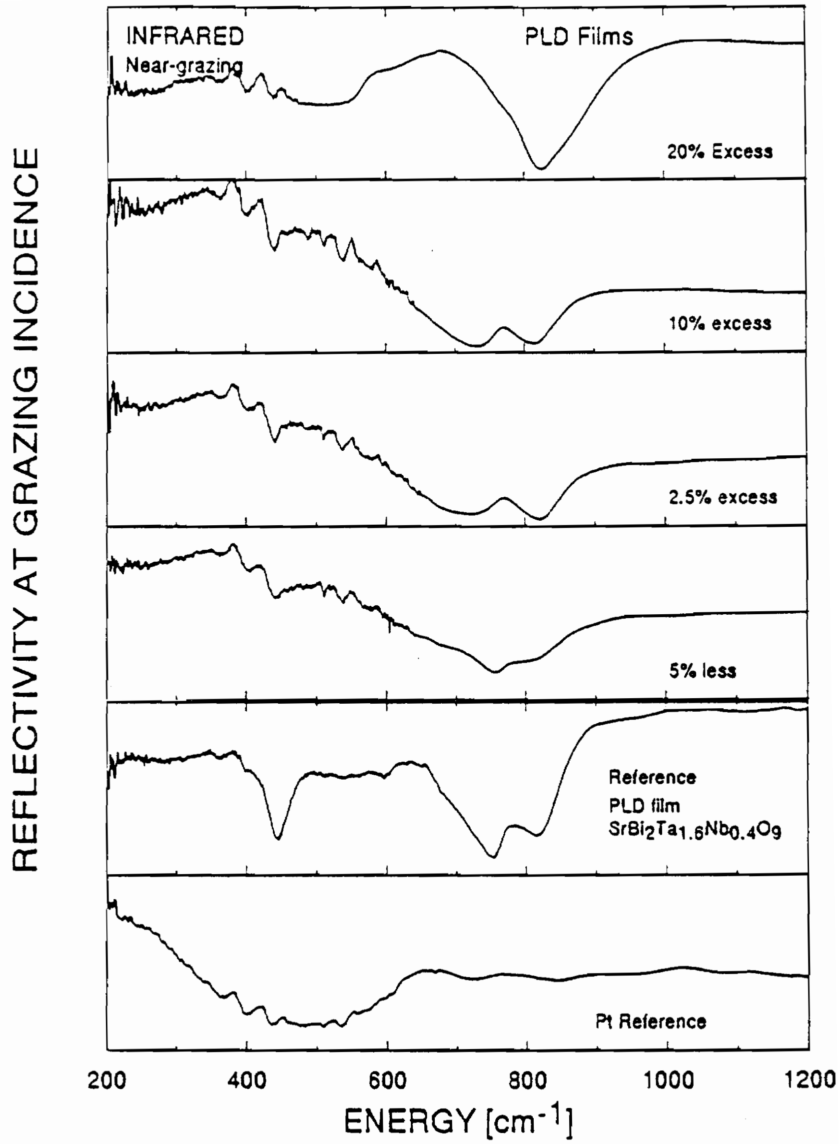

Fig. 2.23 Infrared reflectivity of the films, for various bismuth concentrations.

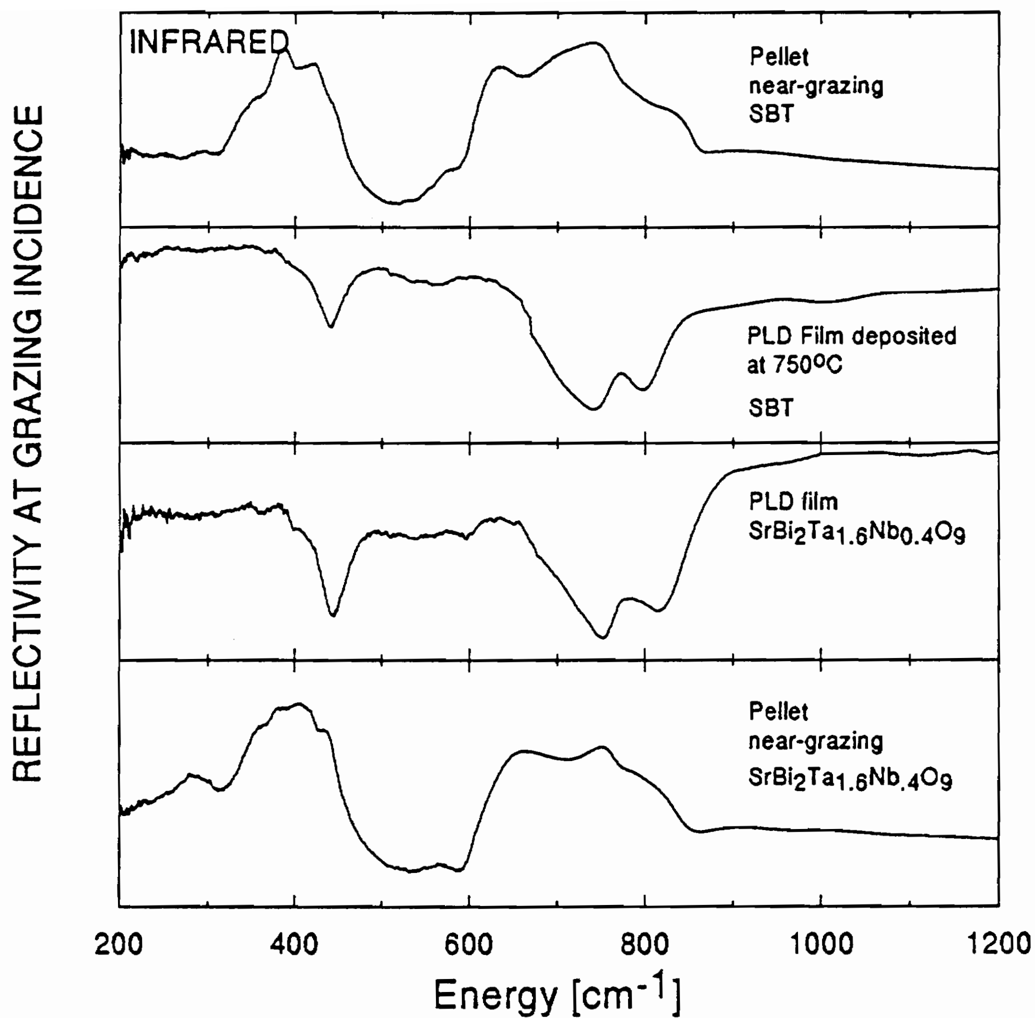

Fig. 2.24 Infrared reflectivity at near-grazing incidence on PLD SBT films and SBT pellet, and PLD $SrBi_2Ta_{1.6}Nb_{0.4}O_9$ film and $SrBi_2Ta_{1.6}Nb_{0.4}O_9$ pellet.

Chapter 3: TiO_2 Films Made by Pulsed-Laser-Deposition

3.1 Background on TiO_2

3.1.1. Polymorphism

Titania is a polymorphic metal dioxide, the mineral has been found with three structures (Bragg and Claringbull, 1965) and (Wyckoff, 1963). The stable condensed phase at all temperatures is rutile. The other two low-pressures crystal phases are anatase and brookite. The three forms, described in Table 3.1, are each composed of octahedral groups of oxygen atoms around titanium, but the octahedra are connected differently for each mineral, producing different structures. Other MX_2 compounds possess the rutile structure but the anatase and brookite structures appear to be unique to TiO_2. The three structures all have orthorhombic symmetry but different space-group symmetry.

Table 3.1 **The three crystal structures of TiO_2.**

Structure	System	Space Group	a(Å)	b(Å)	c(Å)
Rutile Fig. 3.1	Tetragonal	D^{14}_{4h}=P4(2)mmm number 136	4.594	4.594	2.959
Anatase Fig. 3.2	Tetragonal	D^{19}_{4h}=I4(1)/amd number 141	3.7873	3.873	9.5147
Brookite Fig. 3.3	Orthorhombic	D^{15}_{2h}=Pbca number 61	9.14	5.44	5.15

Figures 3.1, 3.2, and 3.3 show the three different structures. As in section 2.3, the software used to simulate the crystal structures from the atom positions is Crystaldraw. The atomic positions used are given in Table 3.2. The dimensionless coordinates given are normalized to the three orthogonal lattice constants.

Table 3.2 **Atomic positions used to generate plot of the structures (Wyckoff, 1963).**

	x	y	z
Rutile			
Ti	0	0	0
O	.3049	.3049	0
Anatase			
Ti	0	0	0
O	0	0	.2066
Brookite			
Ti	.129	.09720	-.1371
O_1	.0101	.14860	.1824
O_2	.2304	.113	-.4629

In addition to these three phases, there are many high-pressure polymorphs.
Two high-pressure, non-equilibrium phases, called TiO_2-II and TiO_2-III, were first synthesized by shock waves (Linde and DeCarli, 1969). Anatase and brookite can irreversibly transform to TiO_2-II and TiO_2-III. The magneli phases are a set of discrete phases, with compositions between TiO and TiO_2, with the form Ti_nO_{2n-1}. Details on the TiO system are summarized in the work of (Murray and Wriedt, 1987).

3.1.2. Applications

TiO_2 has varied applications ranging from toothpaste and candies to paints (for pigment applications) to semiconductor sensor materials. The applications relevant to this study are related to thin film technology. More and more ceramics are used for specific coatings due to high hardness, high melting point, or resistance to chemicals. Some of these ionic ceramics are grown as films, for optical properties. In this thin film form rutile TiO_2 is a very good example as it is grown for a varied number of applications, as seen below.

The different microstructural, electrical, optical, and mechanical properties obtained in the thin films are linked to the deposition method chosen. This choice will depend on the application, which exploits a particular property of the films.

TiO_2 thin films are used in optics due to their high refractive index and stability. High refractive index is reported for films bombarded with particles of high energy (Lobl et al., 1994), (Bennett et al., 1989). Also good optical transmittance in the visible and in the IR combined with the high absorption in the ultraviolet make them good candidates for UV filters. TiO_2 films can also be found in photoelectric devices (electrodes for solar energy conversion), photocatalytic devices, and in the domain of the microelectronics due to their high dielectric constant (Lobstein et al., 1995). Their high dielectric constant also make them promising candidates to replace silicon dioxide and silicon nitride in microelectronics capacitors.

3.1.3. This Study

The present study was initiated to determine the range of structures of TiO_2 which can be obtained by pulsed laser deposition.

In the literature, from 1989 to 1991, many papers can be found reporting TiO_2 thin films deposited by various techniques, (Bennett et al., 1989). The methods reported include sputtering and evaporation (Lobl et al., 1994), metallo-organic chemical vapor deposition, laser ablation, (Lobstein et al., 1995). This is of course not an exhaustive list, but rather a small sample of the recent literature. The first TiO_2 thin films made by PLD seem to have been made in the early to mid 90's (Ardakani, 1994), (Lobstein et al., 1995).

Rutile is usually the dominant crystalline phase in the deposited film. The anatase phase appears occasionally; a few papers, (Arsov et al., 1991), (Lobl et al., 1994), and (Ardakani, 1994), report the deposition of films with anatase present in addition to rutile. This was done using physical vapor deposition techniques, magnetron sputtering and RF sputtering, or PLD. The only TiO_2 films reported by PLD were amorphous (Lobstein et al., 1995) or containing rutile, anatase and certain magneli phases (Ardakani, 1994).

A 1984 Japanese paper (Takahashi et al., 1984) claims the deposition of the brookite phase along with the rutile phase on vapor deposited films. But this was not confirmed by later workers (Mo et al, 1995), who reported that brookite had never been previously deposited in thin films. Brookite has never been reported on films made by the PLD technique, to the best of our knowledge.

3.2 Observation for the First Time of the Brookite Phase in PLD Titania Thin Films

3.2.1 Brookite Identification by X-ray and Raman Measurements

A pellet of titanium dioxide was used as a target for the laser ablation. Two pellets were prepared by pressing and sintering a commercially available 99.95 % purity Fisher TiO_2 powder. One pellet was sintered at 700 C for six hours and the other for six hours at 1000 C. Only the second pellet was used for the deposition as the first one was too brittle; sintering is not achieved at 700 C. But this brittle pellet was used as a reference for the characterization of the films, because it was found to consist essentially entirely of the anatase form of TiO_2. The pellet sintered at 1000 C was found to consist entirely of the rutile form of TiO_2. This will be shown below in Fig. 3.4.

Four samples [Table 3.3] were deposited initially. The first set of films was deposited on Si (1 1 1) substrates. The first three samples were prepared in the normal range of operation of the laser ablation system. The last sample was deposited in what can be called "pushed conditions", higher beam energy and higher pulse rate and smaller target-substrate distance than normally used.

Table 3.3 Deposition parameters for the first four TiO_2 films.

Sample	Substrate Temperature (°C)	Beam energy (mJ)	Pulse rate (Hz)	Oxygen Pressure mTorr	Target-Substrate distance (cm)	Number of pulses (Deposition time)
Sample1	room	600	10	200	4	36,000
Sample2	350	600	10	200	4	36,000
Sample3	750	600	10	200	4	36,000
Sample4	750	900	30	200	3	36,000

The room temperature film is uniform blue-gray. Samples 2 and 3 are very similar, yellow in the center and the surrounding blue. Sample 4 is covered with colorful circular fringes which might be interference fringes explained by a thickness variation arising from the target-substrate distance variation. These fringes are not observable on the films deposited with the standard target-substrate distance.

Ellipsometry measurements were performed on a Variable Angle Spectroscopic Ellipsometer (VASE) Woolam instrument, using visible light. Data were taken at three different angles, to obtain psi and delta. Then from a theoretical model, the thickness, the real part, and the imaginary part of the refractive index could be obtained. The thickness was estimated at 200 nm for samples 2 and 3 and about 400 nm for sample 4.

The identification of the different phases present in the film was done with x-ray diffraction and Raman scattering.

- **X-ray diffraction**

The powder patterns observed for the two pellets were compared with the simulated powder patterns of anatase and rutile. Pellet 1 has the anatase structure and pellet 2 the rutile structure. This is shown in Fig. 3.4. It is evident that pellet 1 is essentially entirely anatase and that pellet 2 is essentially entirely rutile. The brookite powder pattern shown in Fig. 3.4 was simulated using the references quoted in the introduction, and the experimental pattern was observed for a loose powder of the natural mineral.

Figure 3.5 shows XRD results for the four thin film samples, as well as the bare silicon substrate. The silicon substrate exhibits a single peak, as this is a (1 1 1) substrate. The broad background might be due to thermal scattering. Only samples 3 and 4 reveal extra

features other than the silicon. There is a slight broadening in the peak size for sample 3, which is less apparent for sample 4. The phase present in sample 3 is anatase, which is clearly identified by the strong peak at 25.3°.

Sample 4 contains **all three** crystal phases of TiO_2. This is clearly demonstrated in Fig. 3.6, which compares this film's x-ray diffraction pattern to the experimental diffraction patterns of Fig. 3.4 for brookite, anatase, and rutile. Also included in Fig. 3.6 is the XRD pattern for the silicon substrate. All of the lines observed in this film (sample 4) are accounted for by the other patterns included in Fig. 3.6. The main rutile peaks at 27.5°, 36.1°, 54.4° are present; the 25.3 ° and 38.6° anatase peaks are present, and brookite peaks are seen at 25.4°, 25.7°, 30.9°, 40.2°, 46.1°, and 54.3°. The anatase peaks have been indexed with A, brookite peaks with B, and rutile peaks with R. Appendix 2 contains the h k l notation for every peak. The same notation has been used on the x-ray and the Raman figures through the whole chapter. Brookite is thus confirmed in this PLD film.

- **Raman**

Just as the anatase pellet, rutile pellet, and brookite powder provided valuable characterization standards for the Raman work. Figure 3.7 (which shows the Raman spectrum measured for the PLD film sample 4) includes the Raman spectra of these three standards as well as the spectrum corresponding to the silicon substrate. The very sharp low frequency lines that are designated by stars should be ignored; they are plasma lines (from the argon laser) that commonly contaminate Raman spectra taken with the DILOR instrument.

Anatase has a very distinctive peak in the low wavenumber region and three other peaks of much lower intensity. Rutile has two peaks of similar intensities at 439 cm-1 and 608

cm-1, and a broad one at 235 cm-1. The brookite spectrum has more lines than rutile and anatase, as expected for its multi-atom unit cell. In Table 3.4 is a listing of the peaks of the three phases, compared to the value for brookite reported by a group of Russian scientists (Arkhipendo et al., 1984) and described by (Arsov et al., 1991).

There is a good agreement between the Raman spectra reported for the three TiO_2 phases and our measurements. Rutile literature data were compared to the measurements performed by (Betsch et al., 1991), and the anatase one to the measurement referred by (Arsov et al., 1991).

Table 3.4 Raman lines [cm-1] of: rutile, anatase, brookite. Intensities estimates: vs, very strong; s, strong; m medium; ms, medium small; bd, broad; sh, shoulder.

Rutile sintered powder [our data]	Rutile single crystal [literature]	Anatase sintered powder [our data]	Anatase single crystal [literature]	Brookite loose natural powder [our data]	Brookite natural [literature]
143 w	143 w			130 m	127 s
				135 sh	
		150 vs	144 s		150 s
				160 vs	
		198 w	197 w	195 w	193 w
				211 w	212 m
231 bd	235 bd				
				248 m	247 s
				285 m	286 w
				325 m	318 s
				365 m	366 w
		392 m	399 m		
				395 m	
				415 w	412 w
442 s	446 s				
				460 s	462 w
				498 s	502 w
		512 ms	516 m		
				545 s	544 w
				586 s	582 w
610 s	609 s				
		638 m	639 m	640 s, bd	645 w

The first-order (one phonon) silicon Raman line from the substrate, at 521 cm-1, shows up in the thin film spectrum, as does the silicon second-order (two-phonon) threshold at 950 cm-1. The weak peak near 300 cm-1 in the spectrum of the bare substrate is a genuine feature of crystalline silicon (Temple and Hathaway, 1973); (Weinstein and Piermarini, 1975). The Raman scattering strength from the covalent silicon is much stronger the Raman scattering strength of the ionic titania. Even in this case when the silicon is the substrate.

The Raman results of Fig. 3.7 clearly reveal the presence of brookite, as well as anatase and rutile, in the PLD film denoted as sample 4, in agreement with the x-ray results. Figure 3.8 shows a Raman comparison of the four PLD films. The TiO_2 signals from samples 1, 2, and 3 are much smaller than from sample 4; this is seen by the greater relative strength (for films 1, 2, and 3) of the silicon features from the substrate. Only part of this difference is explainable by the greater thickness of sample 4 (about twice as thick as the others). Sample 4 must be better crystallized than the others. Samples 1 and 2 show no peaks attributable to TiO_2 crystalline phases; they are evidently amorphous. Sample 3 contains some anatase. Table 3.5 lists the observed peaks and their identifications.

- **Conclusion.**

There is good agreement between the Raman and x-ray characterization of the TiO_2-on-silicon thin films prepared by pulsed laser deposition. Both techniques clearly reveal, for one of the PLD thin films, the presence of three TiO_2 crystal phases: anatase, brookite, and rutile. **This is the first time that brookite has been synthesized in PLD thin films**. It appears that laser ablation deposition parameters, such as energy and pulse rate of the beam and substrate-target distance, have as much influence on the TiO_2 phases deposited as does the substrate temperature.

Table 3.5 **Raman lines (cm-1) appearing in the first four TiO_2 films.**

Sample 1		Sample 2		Sample 3		Sample 4	
Position (cm-1)	Origin	Position (cm-1)	Origin	Position (cm-1)	Origin	Position (cm-1)	Origin
				142	Anatase	143	Anatase
						198	Ambiguous
						214	Ambiguous
						247	Brookite
305	Si	305	Si	305	Si	290	Brookite
						323	Brookite
						367	Brookite
						397	Anatase
						434-464	Brookite-Rutile Ambiguous
518	Si (111)	518	Si (111)	518	Si (111)	520	Si(111)
						580	Rutile
						637	Anatase-Brookite Ambiguous

3.2.2 Brookite in PLD Films: Reproducibility? Substrate Dependence? Presence of New Phases?

As sample 4 was deposited using special conditions, additional new films were deposited in order to see if for example a pure brookite PLD film could be prepared. First, a simple repetition of exactly the same conditions used for S4 [sample 4] was attempted. Then films were also grown on different substrates. Additionally, different parameters were changed independently during the deposition to try to identify any trends or any critical parameter inherent to the deposition of the brookite phase. Table 3.6 lists the samples prepared.

Table 3.6 List of the TiO_2 samples deposited.

[? refers to the phase discuss below.]

Sample	Substrate	Deposition Conditions [Temperature, Frequency, Energy, #pulses, O_2 Pressure]	Phases present in film
SAMPLE 1	• Si	Room Temperature, 10Hz, 600mJ, 36000, 200mT	Amorphous/Non adherent
SAMPLE 2	• Si	350°C, 10Hz, 600mJ, 36000, 200mT	Amorphous
SAMPLE 3	• Si	750°C, 10Hz, 700mJ, 36000, 200mT	Anatase
SAMPLE 4	• Si	750°C, 30Hz, 900mJ,36000 , 200mT	Brookite/Anatase/Rutile
SAMPLE 5	• Si Repetition	750°C, 30Hz, 900mJ, 36000, 200mT	Brookite/Anatase/Rutile /?
SAMPLE 6	• Si Reduced Thickness	750°C, 30Hz, 900mJ, 18000, 200mT	Brookite/Anatase/?
SAMPLE 7	• Si Reduced Temp	550°C, 30Hz, 900mJ, 36000?, 200mT	Anatase/?
SAMPLE 8	• Sapphire repetition	Repeated S4	Brookite/Anatase/Rutile /?
SAMPLE 9	• Fused Quartz	750°C, 30Hz, 900mJ, 45000, 200mT	Brookite/Anatase/?
SAMPLE 10	• Fused Quartz	700°C,10Hz, 750mJ, 45000, 200mT	Anatase

Samples were deposited on silicon, on sapphire, and on fused quartz (amorphous silica). These substrates, transparent in the UV-visible, were chosen for the optical transmission experiments described below. Figures 3.9 and 3.10 show x-ray and Raman results on three of these films, and both figures include the S4 results for comparison.

From the Raman results, all the samples contain brookite and anatase. Only in sample 8 does rutile seem to be indicated by the clear shoulder at 610 cm-1.

There is a very interesting finding, especially in the Raman spectra, for these three new samples. Extra peaks appear in those three new samples. These occur respectively at 238 cm-1 medium to weak, 252 cm-1 medium to weak, 295 broad, 440 cm-1 weak, and 662 cm-1 (shoulder). The first two seem to come from a splitting of the 248 cm-1 brookite peak. The films have also been run on the SPEX instrument to verify the positions and existence of those new peaks. They appear at the same position on sample 5. Therefore they are real and there is something else in these films. The main extra peaks have been labelled by a ?. Figure 3.9 displays the x-ray patterns and Fig. 3.10 the Raman spectra.

TiO_2-II was measured at ordinary (low pressure) conditions (Mamone et al., 1980). There is no match with our extra peaks, so TiO_2-II is not present in our thin films. Similar measurement at low pressure were not reported for TiO2-III, therefore the possibility is still opened for TiO_2-III.

Another possibility is that these peaks belong to one of the magneli phases. If this was so, it would mean that stoichiometry has not been preserved in the three runs. The 200 mT pressure of O_2 used during deposition was intended to ensure a stoichiometric deposition. This O_2 pressure was the same for these samples as for sample 4, and S4 does not exhibit the extra peaks. Moreover the laser ablation process is used because of its assumed ability for complex compounds to conserve stoichiometry. The possibility of a magneli phase

deposited is not attractive but it could be that there were operator manipulation differences during the preparation of samples S4, S5, S8, and S9. Attempts to determine the Raman spectra of the simplest magneli phases is well beyond the scope of this work.

The final possibility is that a new phase has been deposited.

In this study, we cannot confirm or contradict any of these three possibilities.

The plot of the Raman spectra of S6, S7, and S10 add information as well as the section 3.3. Figure 3.11, displaying the Raman spectrum of S6, indicates evidence of the brookite phase by the definite 130 cm-1 and 365 cm-1 peaks. S6 also exhibits the extra peaks at 238, 252 and 440 cm-1. But S7, displayed in Fig. 3.12, does not contain brookite [no signature at 130 cm-1 but maybe at 365 cm-1 in spot 3], and does show the extra doublet peaks at 238 cm-1 and 252 cm-1. These extra peaks are clearly present on spot 3 (second panel at the top). It should be noticed that the weak silicon peak near 300 cm-1 is very pronounced in this set of data, indicating that the films are very thin. The data on S7 [Fig. 3.12] indicates that the percentage of each phase present on the films is not regular at the whole surface of the film, as the extra doublet peaks are only very distinct for spot 3, which was taken at the center of the film. The other spots were closer to the edge of the samples.

Sample 10 does not display any extra features and Fig. 3.13 clearly reveals the anatase phase. This film was used in the bandgap measurements presented in section 3.3.

• **Conclusion**

Brookite has been synthesized in other PLD films, but precise film reproducibility was not achieved. No purely brookite-structure film was obtained. No dependence on substrate material was found. Some films showed evidence of the presence of phases other than rutile, anatase, and brookite. It was not possible to identify these.

3.2.3 Brookite: Film Homogeneity and Estimation of the Percentage of the Different Phases Present

The deposition of brookite being rather unusual an effort was made to see if it was preferentially grown at either the substrate/film interface or the film surface. X-ray diffraction at near-grazing incidence, as a function of the angle of incidence, was used. Starting with a low angle of incidence, only a volume very close to the surface will see the incident beam. If the angle of incidence [α] is increased progressively (without moving the sample), a different volume, deeper in the sample will be probed. This method was tried on several of the samples: S4, S5, and S8. Figure 3.14, 3.15, and 3.16 contain the results of these experiments. In Appendix 2, there is a listing of the x-ray peaks for randomly oriented powders of rutile, anatase, and brookite.

For sample 4, above 6° angle of incidence, the anatase and brookite peaks near two theta of 25° is not resolved, possibly because the 25.4° peak of brookite is stronger at higher incidences. At angle of incidences around 8° or above, the substrate starts to be apparent in the pattern and indicates that the volume probed is closer to the interface with the substrate. The XRD pattern at 10° angle of incidence are close the patterns obtained in the normal configuration.

Brookite peaks are apparent at all angles of incidence for sample 4, sample 5, and sample 8. Therefore it can be concluded that there is a mixture of the three phases in volumes close to the surface, at the interface, and in between. Brookite does not seem to be preferentially grown at a specific depth in the film.

A very rough estimate has been attempted, for sample 4, to compare the percentage of each phase present from the peak height at the surface or at the interface.

The main idea was to identify the peaks of each phases, and summing them to obtain a percentage of each phase. The same was done simulating a film with the three phases present using the intensities given from the simulated pattern. Only the intensities of the peaks showing up in the measured XRD patterns were taken into account.

•S4 normal configuration - Background corrected:

26 % brookite

59 % anatase

15 % rutile.

→Taking the same peaks in the "simulated" mixture, we obtain:

54 % of brookite

19 % of anatase

26 % of rutile

•Sample 4 at $\alpha=3^{\circ}$ - Background corrected.

45 % of brookite

38 % of anatase

17 % of rutile.

→Taking the same peaks in the theoretical powders:

57 % brookite

18 % of anatase.

25 % rutile

As expected, the percentage between the theoretical percentages and the ones from the patterns do not compare well due to orientation effects which modify the peak intensities; especially at grazing incidence when the diffraction vector is moving.
These estimates indicate that the relative amount of the phases present does not vary greatly between the film surface and the film/substrate interface. A very crude consensus result for the relative proportions of the phases in sample 4, is: (40 ± 20) % brookite, (35 ± 15) % anatase, (20 ± 10) % rutile.

• **Conclusion**

Grazing incidence x-ray diffraction experiments on the PLD TiO_2 films, done as a function of the angle of incidence, indicate that brookite is not grown preferentially either near the surface or at the film/substrate interface. Similarly, the rutile/anatase/brookite mix exhibits no great variation in depth. from the x-ray diffraction results, a crude estimate of the relative proportions of the phases present in sample 4 is: brookite/anatase/rutile in the ratio of 2 / 2 / 1.

3.3 Measurements of the Optical Bandgap of Brookite

(Mo et al., 1995) recently discussed the electrical and optical properties of rutile, anatase, and brookite. Their work gave theoretical estimates of the bandgaps and compared them to experimental results, as shown in Table 3.7.

Table 3.7 Reported data on the rutile, anatase, and brookite bandgaps from (Mo et al. 1995) - See also (Tang et al., 1993) for the experimental data.

Phase	Calculated	Experimental
Rutile	1.78 eV	3.00 eV
Anatase	2.04 eV	3.2 eV
Brookite	2.2 eV	No report

Table 3.7 shows that the bandgap of brookite has not yet been experimentally investigated. In this section, we present the results of optical experiments (in the visible and near-ultraviolet) which were carried out to obtain an estimate of the optical bandgap of brookite.

Table 3.7 also shows that the theoretical calculations of the bandgaps of rutile and anatase are very poor, they are about 1.2 eV too low. If this same underestimate also held for brookite, we might expect the actual brookite bandgap to be about 3.4 eV, which would be the highest of any TiO_2 phase. This extrapolation to brookite is clearly dangerous since these calculations do not match the experimental data for rutile and anatase. In fact, our experimental results (presented below) will show that this extrapolation to brookite is off.

Sample 10 was deposited on sapphire and only contains the anatase phase. Therefore, an estimate of the anatase bandgap was possible in this study. As the anatase bandgap has been reported in literature (Tang et al., 1993), it can be compared to the bandgap of the same materials but deposited on thin films.

Natural crystals of brookite were used for the estimation of the brookite bandgap itself. These crystals were provided to us by Prof. S.C. Moss of the U. of Houston. Bandgap measurements for films S8 and S9 were also carried out. The optical bandgap of a film containing mixed phases should be that of the phase with the lowest bandgap, which cuts off the optical transmission at lowest photon energy. This method can also be used as a phase characterization tool.

3.3.1 Thickness estimation

In order to determine the optical absorption coefficient α from the measured transmission of a sample, it is necessary to know the sample's thickness.
A thickness estimation can be obtained from the interference fringes observed in transmission and reflectivity measurements. Interference fringes are usually observable for a thin sample, provided that its thickness is reasonably uniform.

The condition for constructive interference is the following:

$$m \times (\frac{\lambda}{n}) = 2d \qquad 3.3.7$$

m is an integer designating the interference number, 2d is the path-length difference.
If we are able to plot $1/\lambda$ versus m, the slope is:

$$\frac{1}{2nd} \qquad 3.3.8$$

If the refractive index n is known, then the thickness can be obtained and vice versa. This procedure can be done first using the peaks (constructive interference) and from the valleys (destructive interference), and the average slope can be computed.
The analysis has been conducted on different samples.

Reflectivity measurements were performed on an anatase double sided film deposited by MOCVD. The given data was the thickness: 200 nm. The instrument used was an IR-UV-Vis instrument from the materials science department. The two slopes obtained were 6130 cm-1 and 5620 cm-1. These yield an average refractive index of 2.8. This is consistent with data given in Palik for rutile($2.51 < n_{\perp} < 2.91; 2.88 < n_{//} < 3.24$) for the 2 to 3 eV range.

Using the same instrument, reflectivity from S4 was obtained at the center and at the edge of the sample. Figure 3.17 displays plots of the interference fringes. As S4 contains the three phases, a range of indices of refraction was chosen.
The average thicknesses obtained are listed in Table 3.8.

Table 3.8 **List of the estimated thicknesses for S4 from reflectivity measurements.**

n	S4 center	S4 Edge
2.5	218 nm	226 nm
2.6	210 nm	218 nm
2.7	202 nm	210 nm
2.8	195 nm	202 nm
2.9	188 nm	195 nm
3.0	182 nm	189 nm

This gives consistent thickness from the center to the edge, but still thicker on the edges.

Those data do not agree with the ellipsometry measurement which lead to 400 nm thickness for S4. Therefore the models in the ellipsometry chosen for S2, and S3 were probably more correct. The S4 thickness is probably around 200 nm.

The thickness measurement on S8, and S10 were done on the instrument described in chapter one. In the 1.5 - 3 eV region, interferences were seen in transmission measurements. From the x-ray and Raman characterization, the composition of S8 is a mixture of the three phases. For S10 only the anatase phase is grown. Therefore the n=2.8 should be a good estimation for S10.

Table 3.9 **List of the estimated thickness for S8 and S10 from transmission measurements.**

n	S8	S10
2.7	**117 nm**	**166 nm**
2.8	**113 nm**	**160 nm**
2.9	**109 nm**	**154 nm**
3.0	**105 nm**	**149 nm**

The two films give data in the same ranges, but S10 seems thicker than S8. But the thickness still ranges in between 100 to 200 nm.

• **Conclusion.**

The thickness estimates from the interference fringes lead to a thickness of about 200 nm for S4, about 100 nm for S8, and about 150 nm for S10.

3.3.2 Bandgap Measurements from UV-visible Optical Absorption

The absorption coefficient α of a material can be measured from transmission measurements in the visible region. The general form of the transmission can be written as

$$t = \frac{I(sample)}{I_0(reference)} = \frac{(1-R)^2 + 4R\sin^2\theta}{1-R^2e^{-2\alpha d}} \times e^{-\alpha d} \qquad 3.3.1 \text{ (Palik, 1985)}$$

Here d is the sample thickness, R is the reflectivity as defined in section 2.5.1. and α is the absorption coefficient. The angle θ is defined by:

$$\tan\theta = \frac{2k}{n^2 + k^2 - 1} \qquad 3.3.2$$

At these wavelengths the second term of the numerator in 3.3.1 can be ignored with respect to the first one, because the reflectivity is much higher than the absorption near the bandgap, therefore $\theta << 1$.

The following analysis was used (Zallen, 1962).

• When $e^{-\alpha d} << 1$ (highly absorbing region), the original formula for t can be simplified :

$$t \approx [(1-R^2) + 4R^2\sin\theta]e^{-\alpha d} = (1-R^2)e^{-\alpha d} \qquad 3.3.3$$

$$t \approx [(1-R^2)+4R^2 \sin\theta]e^{-\alpha d} = (1-R^2)e^{-\alpha d} \qquad 3.3.3$$

• On the other hand, in the transparent region $[e^{-\alpha d} \approx 1]$, t becomes:

$$t = t_o = \frac{(1-R)^2}{1-R^2} = \frac{(1-R)(1-R)}{(1-R)(1+R)} = \frac{(1-R)}{(1+R)} \qquad 3.3.4$$

• We introduce a normalized transmission T which is defined as t/t_o. In the highly absorbing region, T is given by:

$$T \equiv \frac{t}{t_0} = \frac{(1-R^2)e^{-\alpha d}}{\frac{(1-R)}{(1+R)}} = (1-R^2)e^{-\alpha d} \approx e^{-\alpha d} \qquad 3.3.5$$

Since R is 0.2 or smaller in this region, $(1-R^2)$ is, in fact, close to 1.

The final expression then used to obtain the absorption coefficient is the following:

$$\alpha = \frac{1}{d}(-\ln T) \qquad 3.3.6$$

This relation is strictly valid only when T is much less than 1. In practice, it is an excellent approximation when T is less than 0.5.

The transmission of very thin films such as our PLD films, roughly 200 nm thick, cannot be compared directly to the transmission of a bulk crystal of 0.5 mm thickness. Figure 3.18 shows the transmittance curves obtained from our films and our crystal. To be compared with respect to each other, the absorption coefficients need to be plotted, using equation 3.3.6. The absorption coefficients are shown in Fig. 3.19. In addition to our measurements, the measurements of (Tang et al., 1994) and (Tang et al., 1995) are reported on this figure. They are for rutile and anatase sputtered films and crystals. Their anatase-film measurements is consistent with ours. The different parts of the

For the brookite phase, the intermediate part of the absorption coefficient curve is missing. As S8 and S9 films contain brookite, they should represent the higher part of the curve. The crystal is going to be thinned down, so we can determine what kind of bandgap brookite has. Two options are expected, and are schematized on Fig. 3.19 with a question mark. If the absorption coefficient curve goes up sharply we might be able to join it with the data on the thin films. It would mean that the bandgap is direct, and it is the brookite phase which cuts off the transmission on the PLD film. If the absorption curve keeps the same shape all the way and does not rise sharply, we will not be able to relate the thin film measurements and the brookite crystal measurements. This would indicate that the brookite bandgap is indirect, and that it is the rutile phase which cuts off on the films. This work is still under way, and will be shortly finished.

• **Conclusions**

We report for the first time measurements on the absorption coefficients of brookite crystals and thin films. This measurement is not completed yet, but still shows that the bandgap is lower than the one observed in the rutile or anatase phase. This is in contradiction with the theoretical prediction. The measurements on the PLD film containing anatase are consistent with previous reports.

3.4 Summary for PLD Titania Films and Future Directions

The growth of brookite on PLD thin films has been realized for the first time. This may open a new area in thin film development and maybe another industrial application for the PLD system.

It has not been possible for us to exactly repeat the films containing brookite. But the films in the specific deposition conditions all contain brookite. It is probably more realizable on newer PLD systems which are designed for industrial purposes.

The films do not exhibit a preference of the brookite phase for either the interface substrate/film neither or the surface of the film. The percentages of the phases seem to be uniform in depth from the x-ray near-grazing incidence measurements. For our best-characterized brookite-containing film, a crude estimate of the relative proportion is brookite / anatase / rutile in the ratio 2 / 2 / 1.

The Raman measurements indicate that the phase mixture is not homogenous across the film area. Certain films even features new bands. These new bands have not been clearly identified. They could be from a magneli phase, the TiO_2-III high pressure phase, or from a new phase synthesized with the PLD system. A literature search was not successful, and further investigations could be undertaken to try to isolate this phase. An x-ray refinement around the new peaks would be very helpful as the rutile, anatase, and brookite are known.

The deposition of other metastable phases could be tried, using similar deposition conditions as for brookite. Work is undertaken in this direction to
focus on the deposition of metastable phases with the PLD system in the thin film lab at Virginia Tech. This is a new area of thin film technology, which can lead to surprising

and unexpected results. The preparation of PLD brookite is an example of this. New thin-film novel materials and applications could emerge from it.

In addition to this work, which is related to the technology of thin films, we also report work on the brookite phase itself. The first experimental measurement of brookite's absorption edge is included in this work. The bandgap is lower than for anatase and rutile. This is in contradiction with theoretical calculations.
In very near-future experiments, the brookite crystal will be thinned down to determine if the bandgap of brookite is direct or indirect. These results will also tell us whether it is the brookite or the rutile in the PLD films that is responsible for their ultraviolet transmission cutoff.

Rutile
(100)

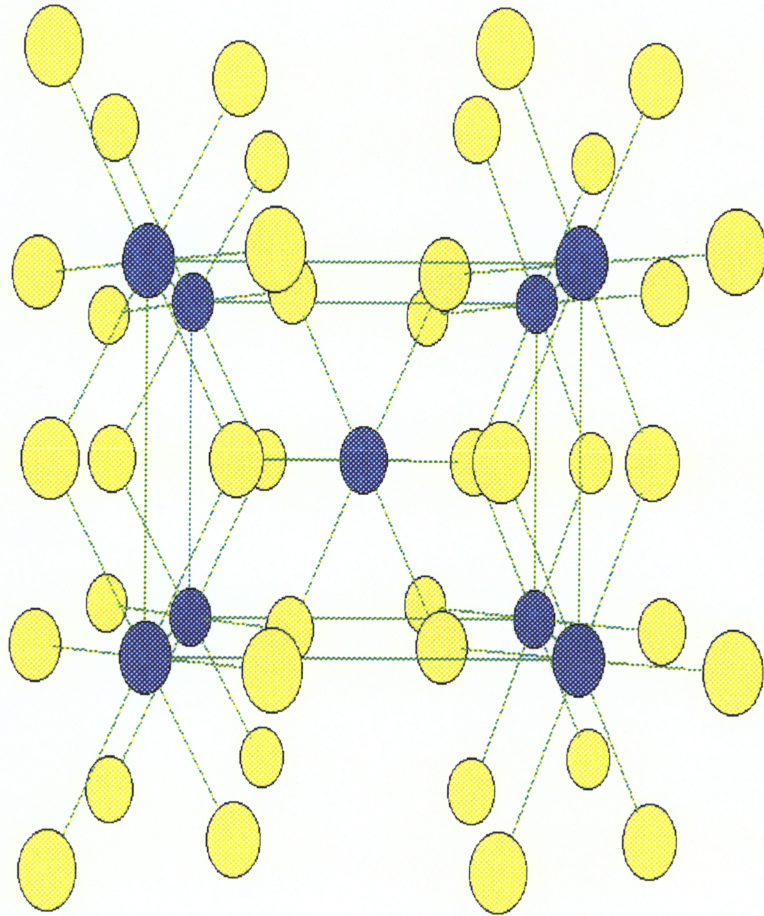

Titanium
Oxygen

Fig. 3.1 Structure of rutile generated in the 100 plane with Xtaldraw.

Anatase [110]

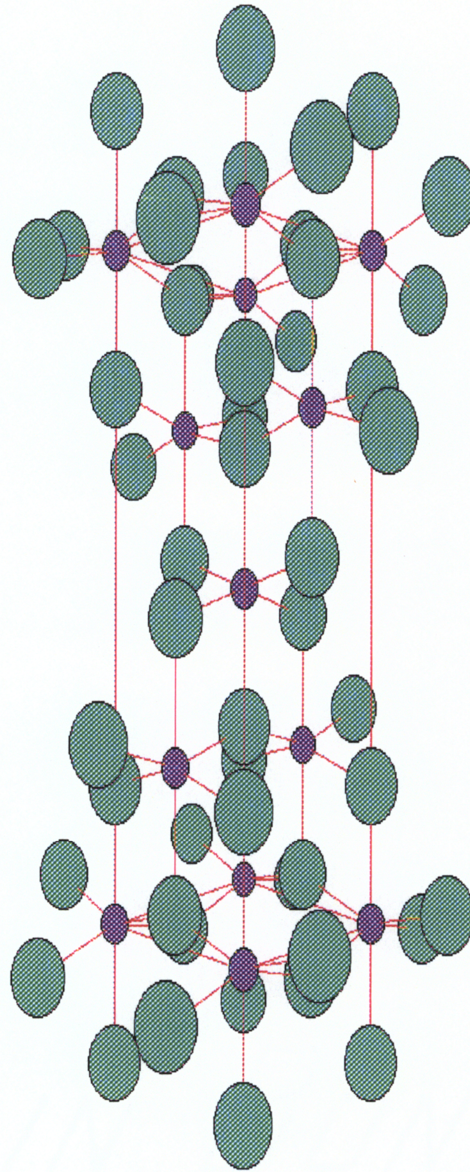

Titanium
Oxygen

Fig. 3.2 Structure of anatase generated in 010 plane with Xtaldraw.

Brookite(010)

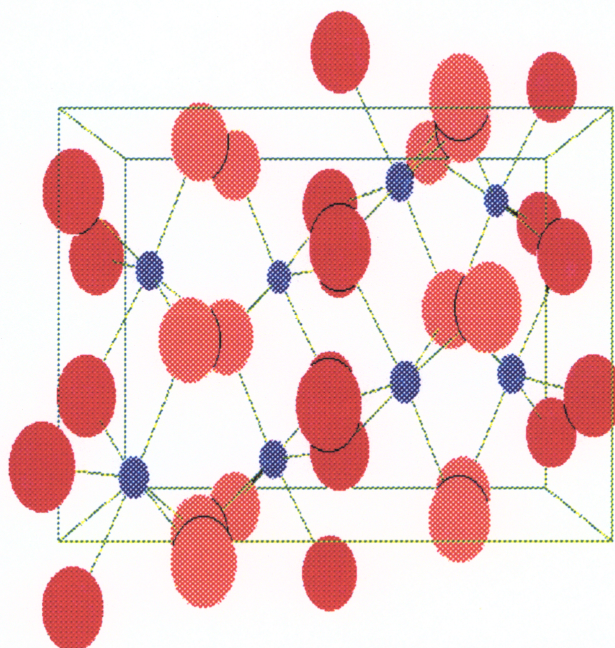

Titanium

Oxygen

Oxygen

Fig. 3.3 Structure of brookite generated in 010 plane with Crystaldraw.

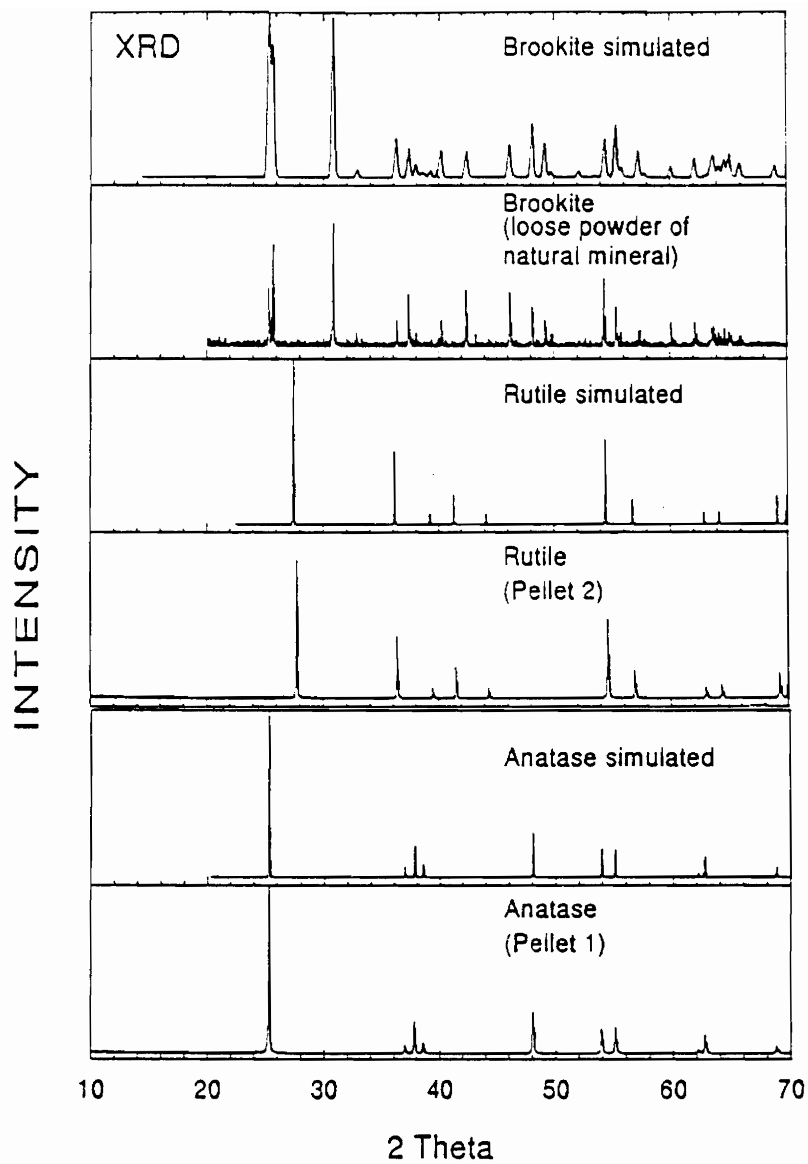

Fig. 3.4 Comparison between the x-ray powder patterns measured and simulated for the TiO_2 crystals phases.

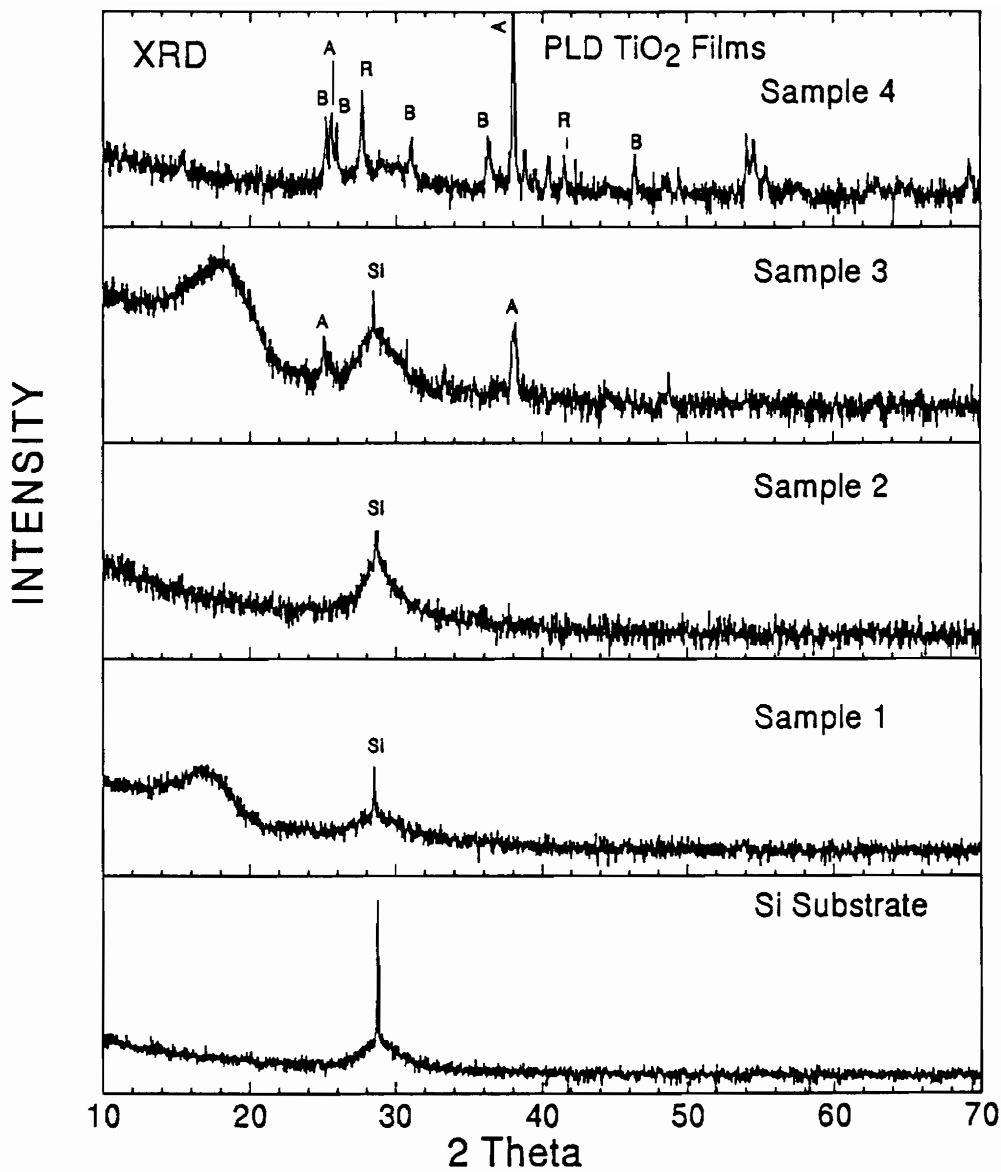

Fig. 3.5 X-ray powder pattern of the first four TiO_2 films.

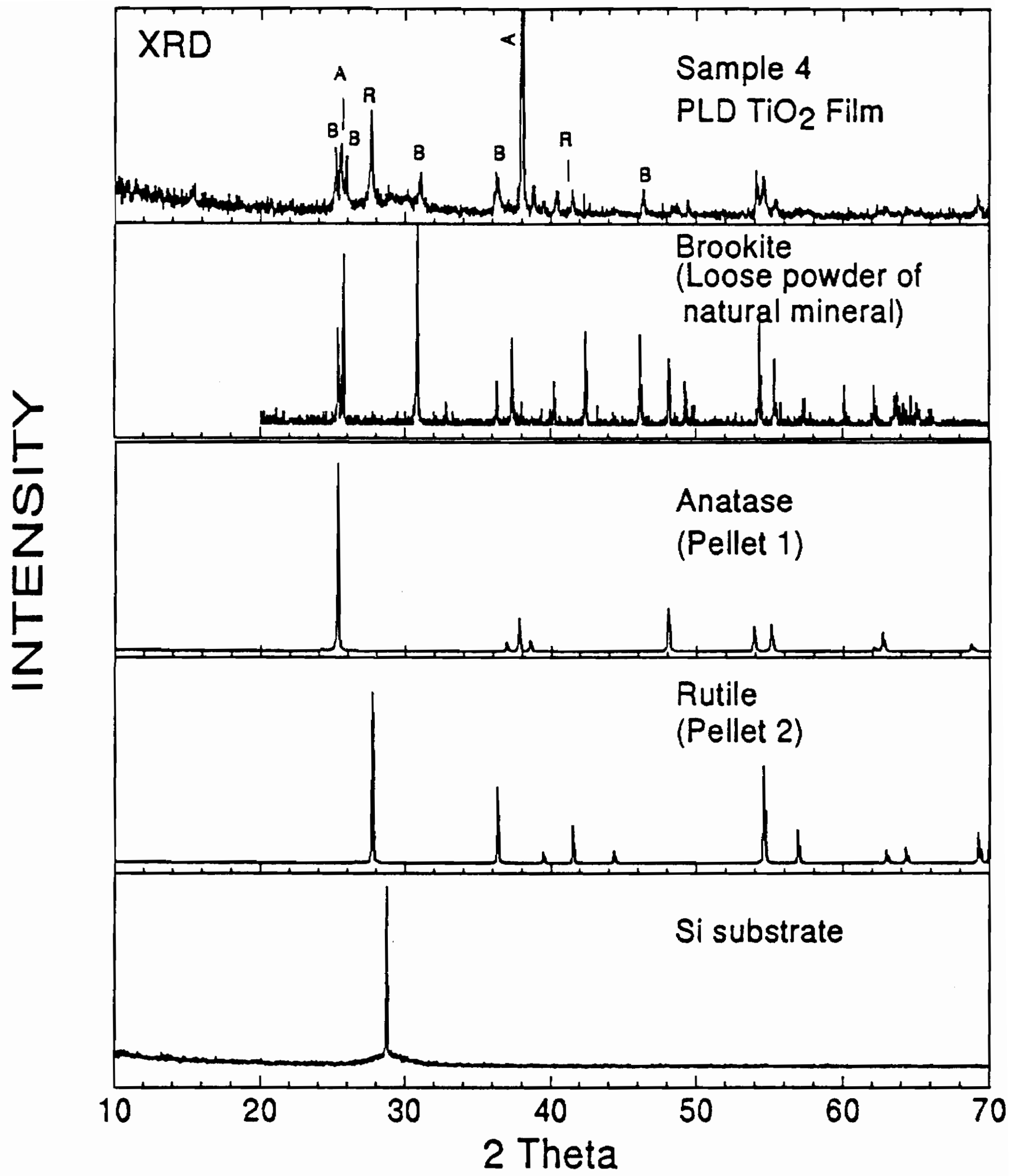

Fig. 3.6 X-ray powder pattern of the TiO_2 crystal phases and Sample 4 [S4].

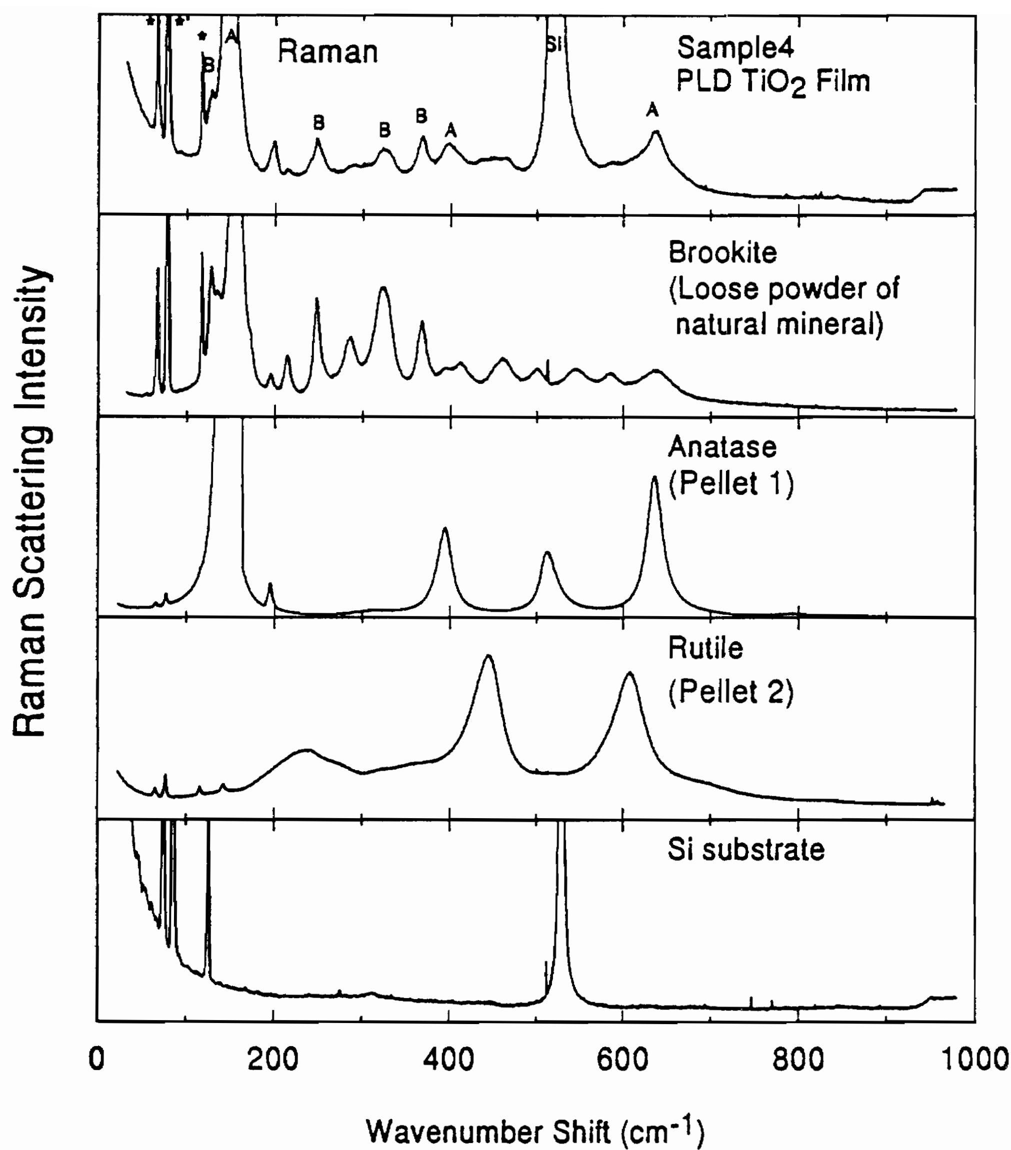

Fig. 3.7 Raman data from the TiO_2 crystal phases and Sample 4.

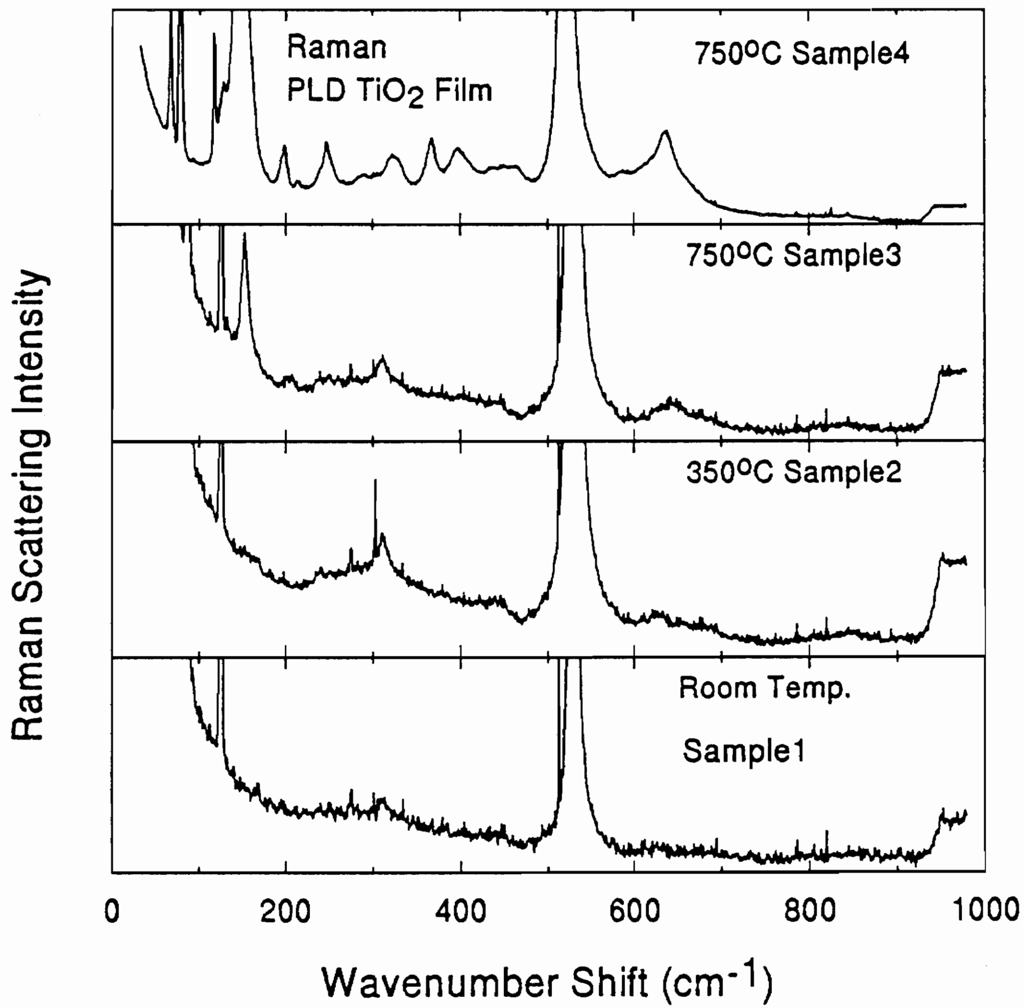

Fig. 3.8 Raman data obtained on the first four TiO_2 samples.

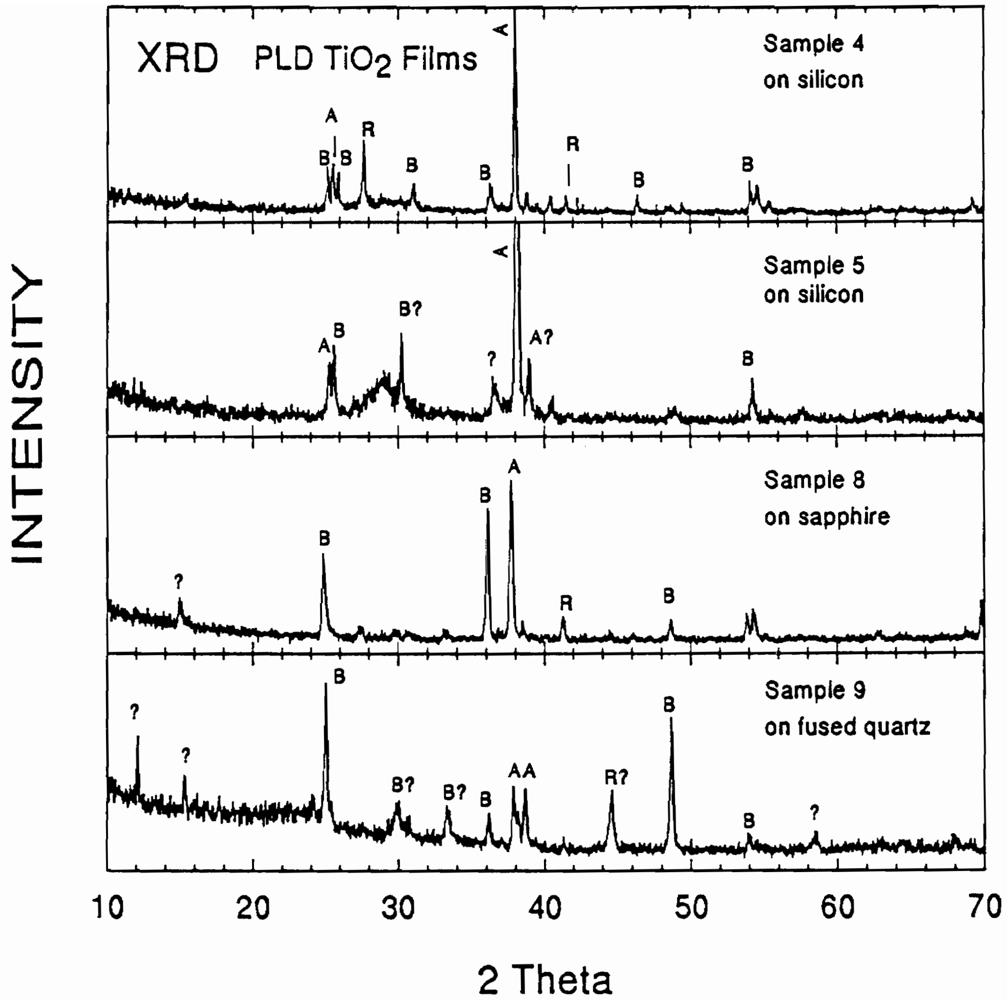

Fig. 3.9 X-ray powder patterns obtained on the four film-samples deposited in the exact same conditions as S4.

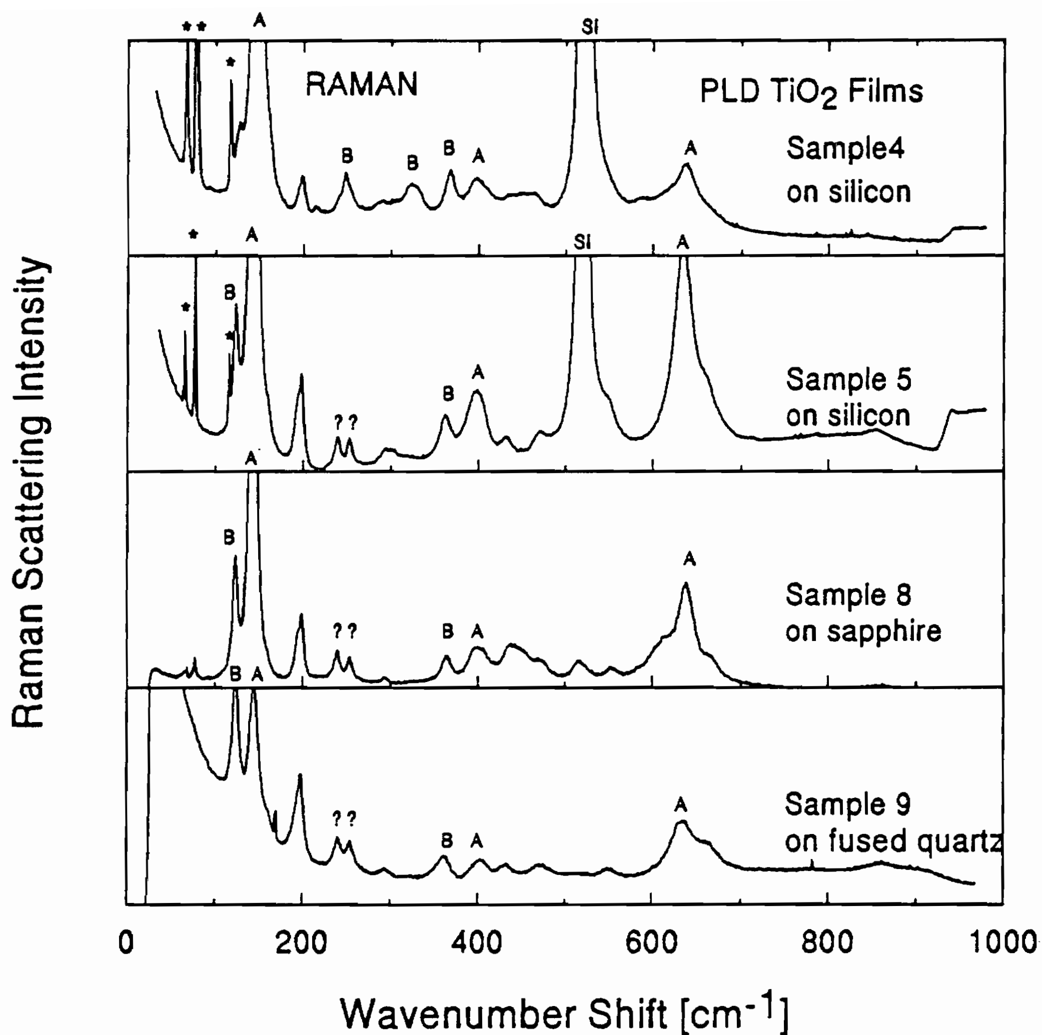

Fig. 3.10 Raman data on the four film-samples deposited in the exact same conditions as S4.

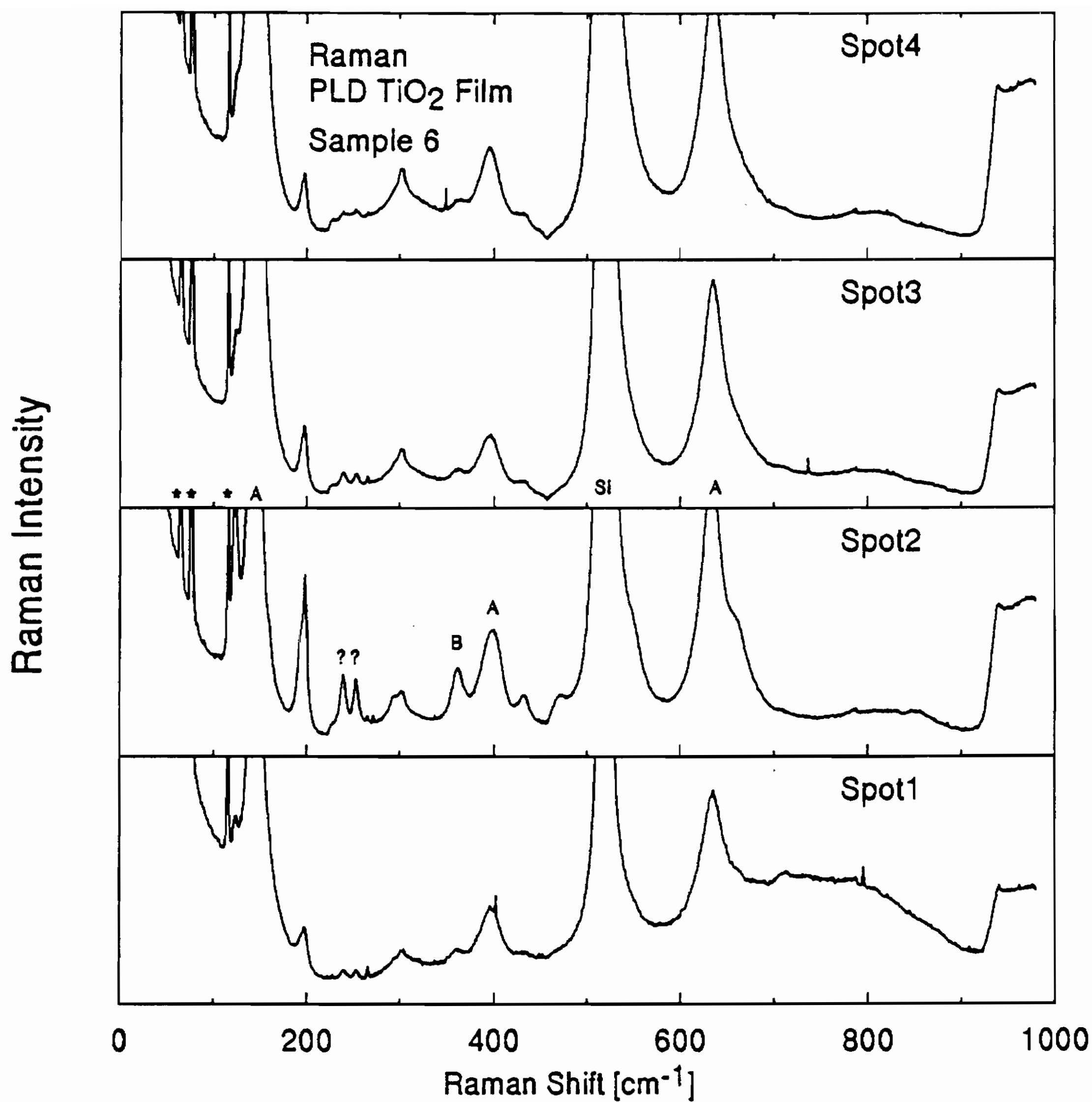

Fig. 3.11 Raman data obtained at different locations on the surface of the film S6.

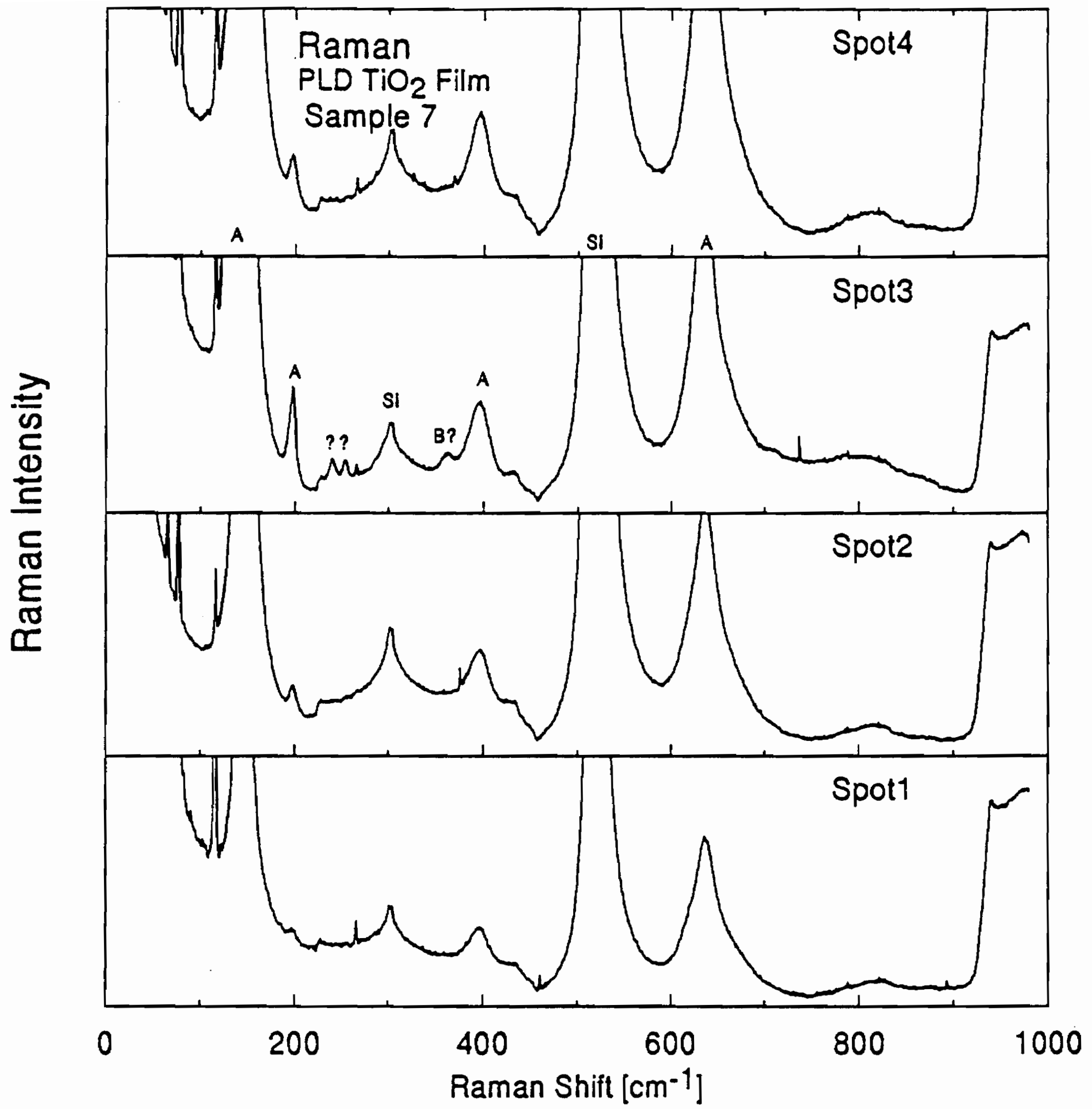

Fig. 3.12 Raman data obtained at different locations on the surface of the film S7.

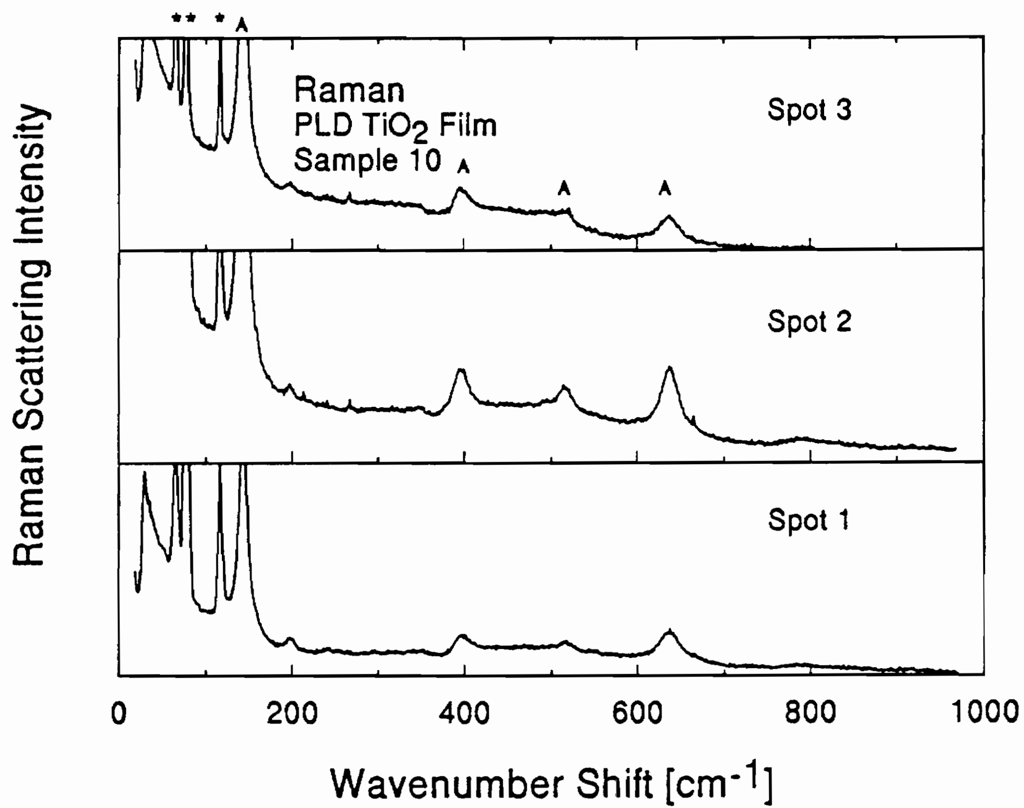

Fig. 3.13 Raman data obtained at different locations on the surface of the film S10.

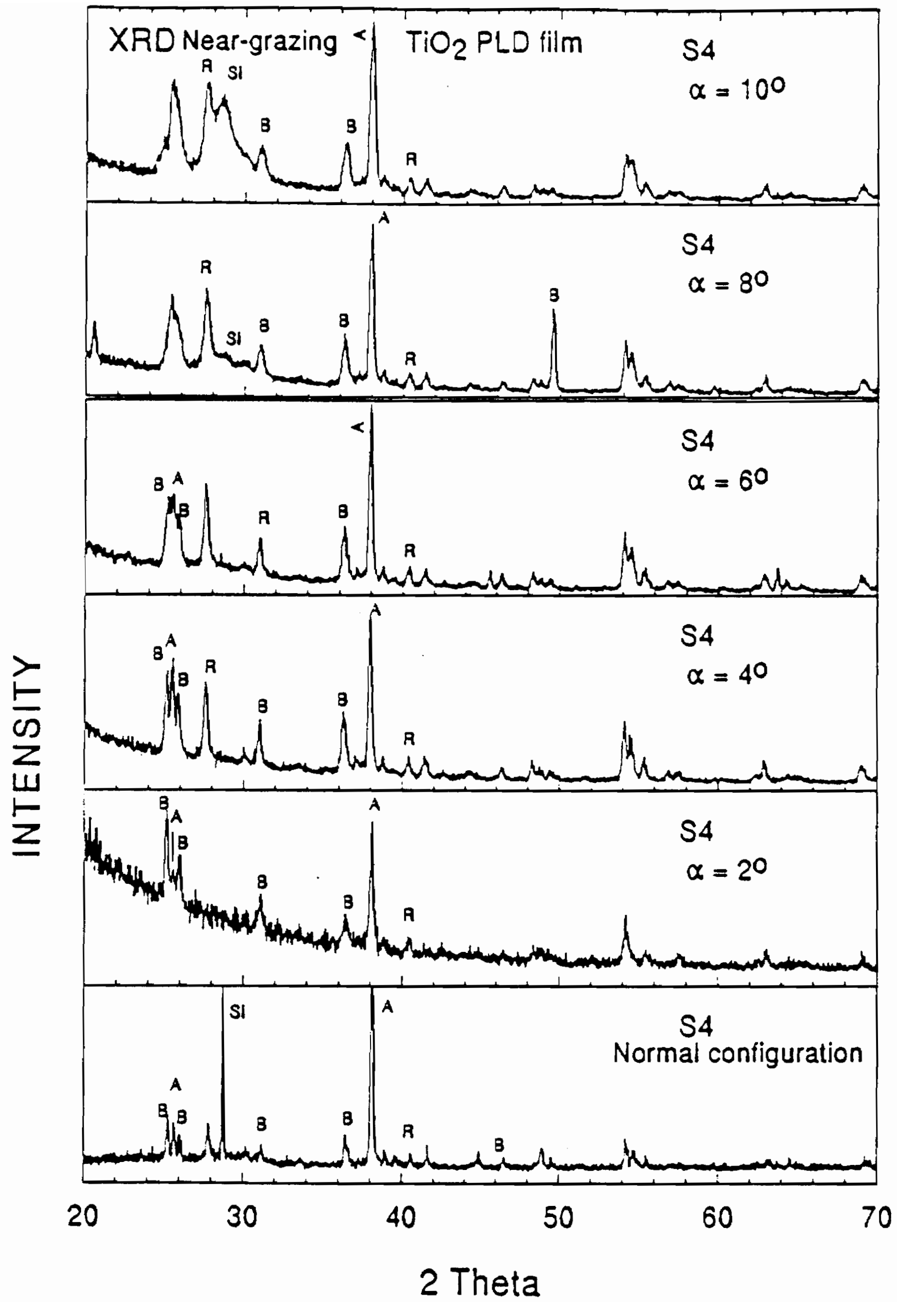

Fig. 3.14 Near-grazing x-ray pattern of S4 for various angles of incidence.

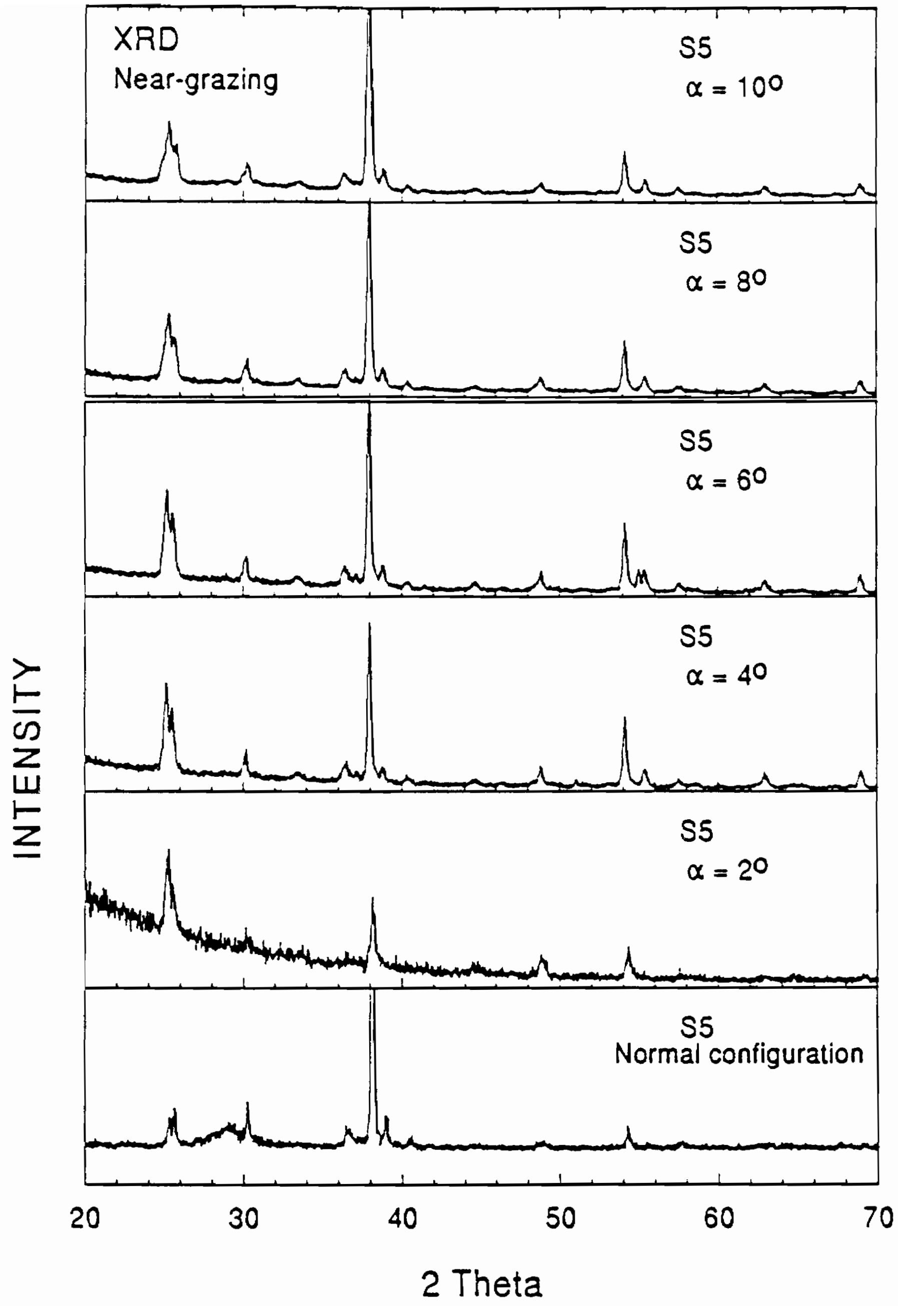

Fig. 3.15 Near-grazing x-ray pattern of S5 for various angles of incidence.

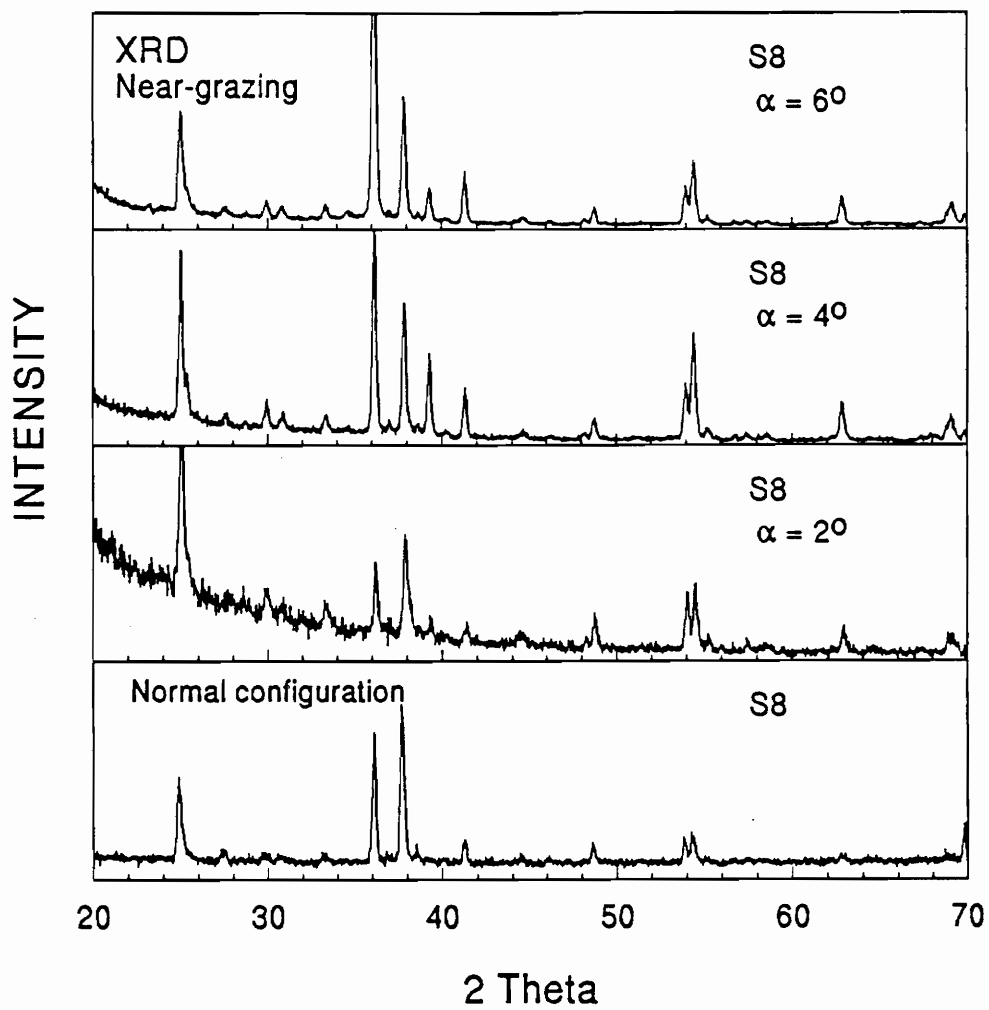

Fig. 3.16 Near-grazing x-ray pattern of S8 for various angles of incidence.

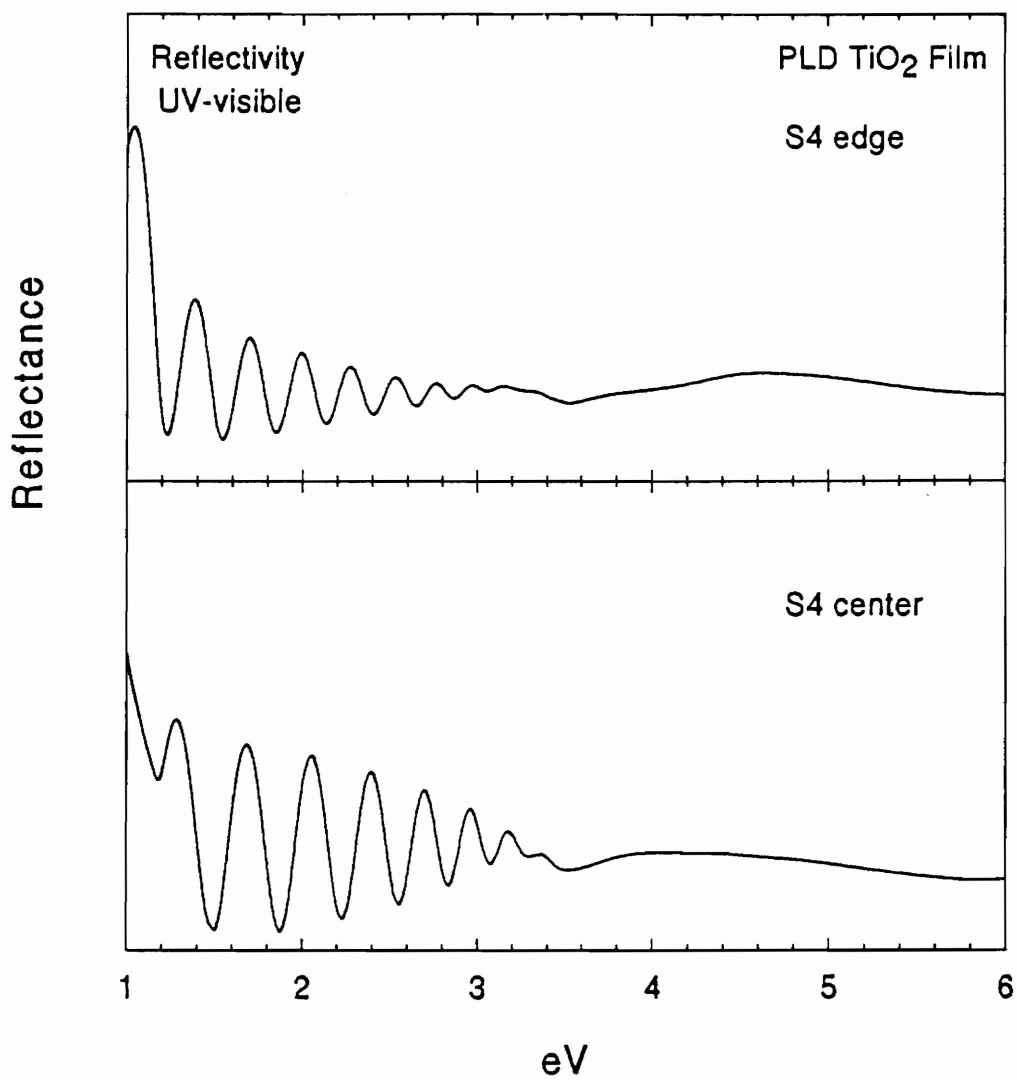

Fig. 3.17 Reflectivity measurements on S4 in the UV-visible region.

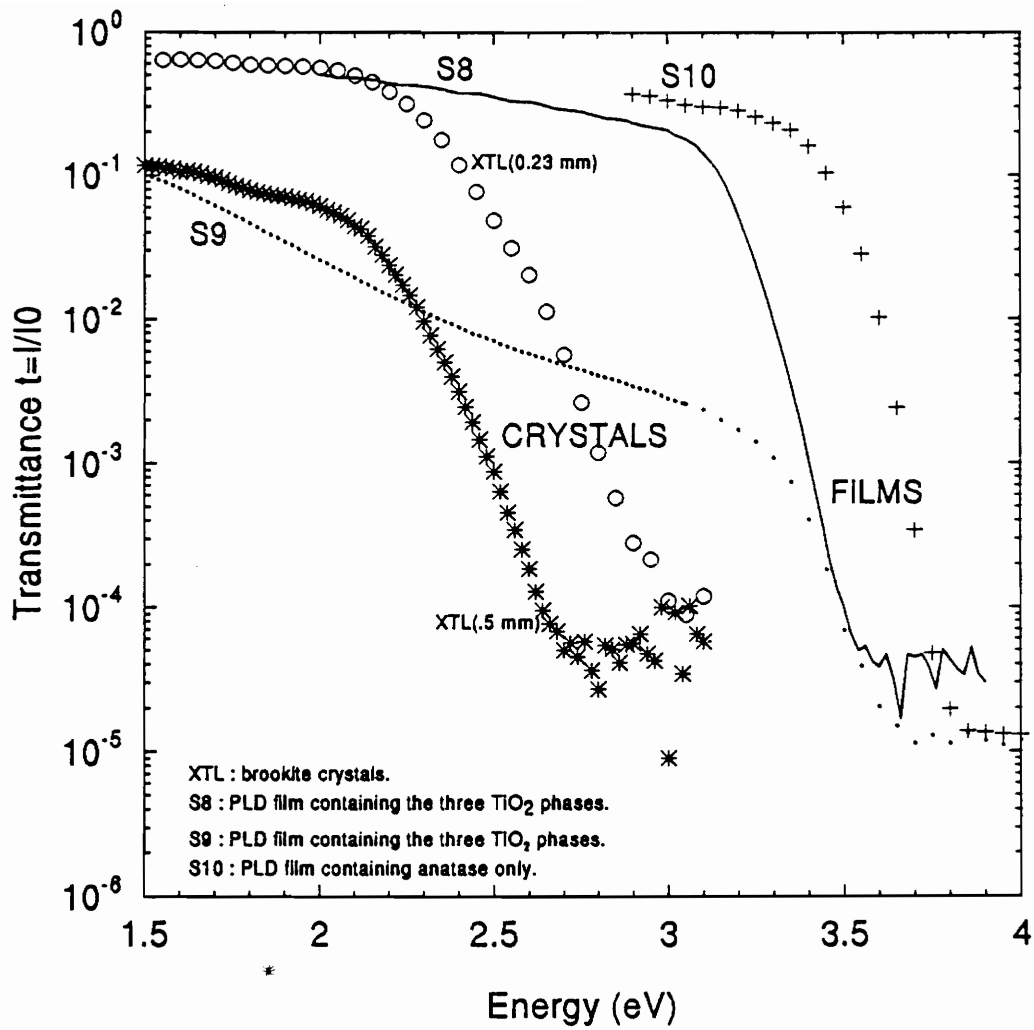

Fig. 3.18 Transmission measurements of the PLD TiO_2 films and brookite crystals.

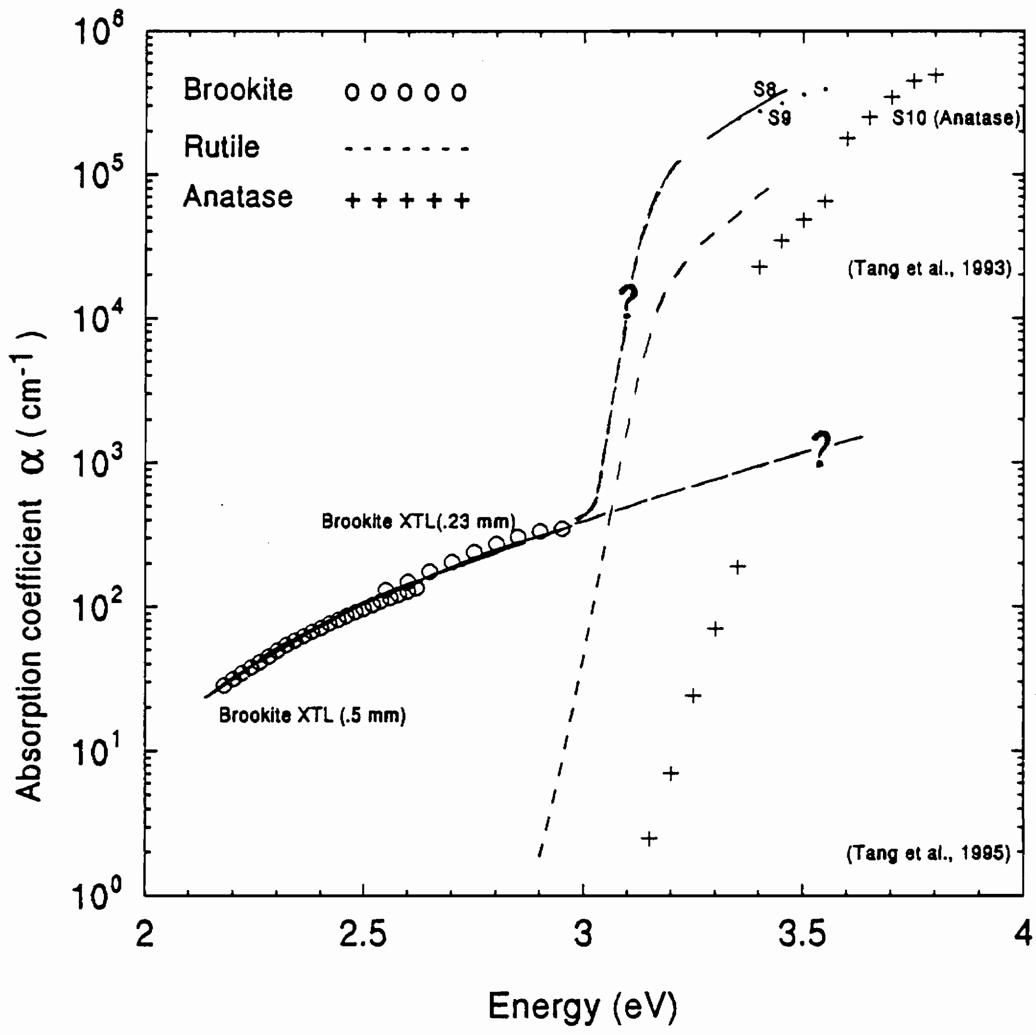

Fig. 3.19 Absorption coefficients for rutile, anatase, and brookite.

REFERENCES

AIP CONFERENCE PROCEEDINGS 288, *"Laser Ablation: Mech. Appl.-II. Int. Conf. 2nd"*, Knoxville, (1993).

AMANUMA K., Hase T., and Yoichi Miyasaka, "Structural and Ferroelectric Properties of $SrBi_2Ta_2O_9$ Thin Films", *Mat.Res.Soc.Symp.Proc.* **361**, (1995).

ARAUJO C.A.P., Cuchiaro J.D., McMillian L.D., Scott M.C., and Scott J.F., "Fatigue Free Ferroelectric Capacitors with platinum Electrodes", *Letters to Nature* **374**, 627-629, (1995).

ARDAKANI H.K., "Electrical and Optical Properties on in situ Hydrogen-Reduced Titanium Dioxide Thin Films Deposited by Pulse Excimer Laser Ablation", *Thin Solids Films* **248**, 234-239, (1994).

ARKHIPENKO D.K., Bobovich Ya.S., Tsenter M.Ya., "Raman Spectra of Natural Brookites (Titanium Dioxide)", *Zh. Prikl. Spektrosk.* **41**, 304-307, 1984.

ARSOV Lj.D., Kormann C., Plieth W., :"Electrochemical Synthesis and *In Situ* Raman spectroscopy of Thin Films of Titanium Dioxide", *J. Raman Spectrosc.* **22**, 573-575, 1991.

AURIVILLIUS B., "Mixed Bismuth Oxides with Layer lattices", *Arkiv for Kemi* **1**, 463-480, (1949).

BARKER A.S. and Hopfield J.J., "Coupled Optical Phonon Mode Theory of the Ir dispersion in $BaTiO_3$, $SrTiO_3$, and KTaO3", *Phys. Rev.*, **135**, A1732-A1737, (1964).

BENNETT J.M., Pelletier E., Albrand G., Borgogno J.P., Lazarides B., Carniglia C.K., Schmell R.A., Allen T.H., Tuttle-Hart T., Guenther K.H., and Saxer A., "Comparison of the Properties of Titanium Dioxide Films Prepared by Variuous Techniques", *Appl. Opt.* **28**, 3303-3317, (1989).

BERREMAN D.W.," Infrared Absorption at Longitudinal Frequency in Cubic Crystal Films", *Phys. Rev.* **130**, 2193,(1963).

BERREMAN D.W. and Unterwald F.C., "Adjusting Poles and Zeros of Dielectric Dispersion to Fit Reststrahlen of $PrCl_3$ and $LaCl_3$", *Phys. Review*. **174**, 791-799, (1968).

BETSCH R.J., Park H.L., and White W.B., "Raman Spectra of Stoichiometric and Defect Rutile.", *Mat. Res. Bull.* **26**, 613-622, (1991).

BRAGG O.B.E. and Claringbull G.F., "Crystal structure of minerals", G.Bell&Sons, (1965).

BURNS G., "Solid-State Physics", Academic Press, (1985).

BURNS G.and Glazer A.M., "Space Groups for Solid-State Scientists", Academic Press, (1978).

CHEN S.Y, Du X.F., and Chen I.W., "Crystallization and Texture of Bi-Containing Layered Perovskite Thin Films", *Mat.Res.Soc.Symp.Proc.* **361**, 15-20, (1995).

CULLITY B.D, Elements of X-Ray Diffraction", 2nd edition, Addison-Wesley Company, Inc., (1978).

ENCYCLOPEDIA OF INDUSTRIAL CHEMISTRY, **B1**, Ullmann's.

FENG G., "Optical Studies of Ion-Bombarded Gallium Arsenide", PhD thesis, Virginia Tech, (1989).

GRAVES P.R., Hua G., Myhra S., and Thompson J.G., "The Raman Modes of the Aurivillius Phases: Temperature and Polarization Dependence", *J. of Solid State Chem.* **114**, 112-122, (1995).

GONZALEZ R.J., Zallen R., and Berger H., "Infrared Reflectivity and Lattice Fundamentals of Anatase TiO_2", *submitted to Phys. Rev. B.*, 1996.

HARSHAVARDAN k.s., Green S.M., Pique A., Patel K., Edwards R., Venkatesan T., Denlinger E., Kalokitis D., Fathy A., Pendrick V., Wu X.D., Bhattacharaya S., and Rajeswari M., "High TC Thin Films Deposited by PLD onto Technologically Important Substrates", *AIP Conf. Proc.* **288**, 607-612, (1993).

HOLTZ M., "Raman Scattering Studies of the Structure of Ion-Implanted Ga-As", PhD thesis Virginia Tech, (1987).

HOPFE V., Korte E.H., Klobes P., and Grählert W., "Optical Data of Rough-Surfaced Ceramics: Infrared Specular and Diffuse Reflectance versus Spectra Simulation", *Appl. Spectros.* **47**, 423-449, 1993.

HUMMEL R.E., K-H, "Handbook of Optical Properties", **VI**, CRC, (1995).

JACKSON J.D, "Classical Electrodynamics", Wiley, 2nd edition, (1975).

LINDE R.K. and DeCarli P.S., "Polymorphic Behavior of Titania under Dynamic Loading", *J. of Chem. Phys.* **50**, 319-325, (1968).

LIU J., Zou G., Yang H., and Cui Q., "The Soft Mode Phase Transition of $SrBi_2Nb_2O_9$", *Solid State Commun.* **90**, 365-367, (1994).

LOBL P., Huppertz, and D. Mergel, "Nucleation and Growth in TiO_2 Films Prepared by Sputtering and Evaporation.", *Thin Solids Films* **251**, 72-79, (1994).

LOBSTEIN N., Millon E., Hachimi A., Muller J.F., Alnot M., and Ehrhardt J.J., "Deposition by Laser Ablation and Characterization of Titanium Dioxide Films on Polyethylene-terephtalate", *Appl. Surf. Sci.* **89**, 307-321, (1995).

MAMMONE J.F., Sharma S.K., Nicol M., "Raman Study of Rutile (TiO_2) at High Pressure.", *Solid State Commun.* **34**, 799-802, (1980).

MAMMONE J.F., Nicol M., and Sharma S.K., "Raman Spectra of TiO2-II, TiO2-III, SnO2, and GeO2 at High Pressure.", *J.Phys.Chem.Solids* **42**, 379-384, (1981).

MILLER, "Laser Ablation Principles and Applications", Springer-Verlag, (1994).

MO S-D. and Ching W.Y., "Electronic and Optical Properties of Titanium Dioxide: Rutile, Anatase, and Brookite.", *Phys. Rev. B* **19**, 13023-13032, (1995).

MURRAY J.L. and Wriedt H.A., "The O-Ti (Oxygen-Titanium) System.", *Bull. Alloy Phases Diagram* **8**, 148-165, (1987).

NEWNHAM R.E, Wolfe R.W., Horsey R.S., Diaz-Colon F.A., and Kay M.I., "Structural Basis of Ferroelectricity in the Bismuth Titanate Family", *Mat.Res.Bul.* **6**, 1029-1039, (1971).

NEWNHAM R.E, Wolfe R.W., Horsey R.S., Diaz-Colon F.A., and Kay M.I,"Crystal Structure of (SrBa) $Bi_2Ta_2O_9$", *Mater. Res. Bull.* **8**, 1183-1196, (1973).

PALIK E.D., "Handbook of optical Constants of Solids", Academic Press Handbook Series, (1985).

PAULING Linus, "The nature of the Chemical Bond", 3rd edition,Cornell University Press, (1960).

PERKOWITZ S., "Optical Characterization of Semiconductors", Academic Press, (1993).

RAE A.D, Thompson J.G, and Whithers R.L, "Structure Refinement of Commensurately Bismuth Strontium Tantalate $Bi_2SrTa_2O_9$", *Acta. Crys.* B**48**, 418-428, (1992).

RYTZ D., Fontana M.D., Servoin J.L., and Gervais F.,"High Temperature Infrared Reflectivity Study of the soft mode in $KTa_{1-x}Nb_2O_3$ for a Nb concentration x=.018", *Phys. Rev. B* **28**, 6041-6050, (1983).

SCOTT J.F., "Ferroelectric Memories", *Phys. World* **February**, 46-50, (1995).

SMOLENSKII G.A. Bokov V.A., Isupov V.A., Krainik N.N., Pasynkov R.E., and Sokolov A.I."Ferroelectrics and Related Materials" **3** , Gordon and Breach Science Publishers, (1984).

TAKAHASHI Y., Wakayama S., Ogiso A., and Sugiyama K., "Selective Deposition of Anatase, Rutile, and Brookite Films by Vapor Phase Decomposition of Alkyl Titanates", *Kinzoku Hyomem Gijutsu* **35**, 584- 589, (1984).

TEMPLE P.A. and Hathaway C.E., "Multiphonon Raman Spectrum on Silicon", *Pys. Rev. B* **7**, 3685-36997, (1973).

VESZELEI M., Andersson K., Ribbing C.-G., Järrendahl K., and Arwin H., "Optical Constants and Drude Analysis of Sputtered Zirconium Nitride Films", *Appl. Opt.* **33**, 1993-2001, (1994).

VIJAY Dilip, "Reliability and Processing Thin Films Capacitors with Emphasis on Fatigue and Etching", PhD thesis Virginia Tech, (1995).

WARREN B.E, "X-Ray Diffraction", Dover Publications, Inc, (1969).

WEINSTEIN B.A. and Piermarini G.J., "Raman Scattering and Phonon Dispersion in Si and GaP at Very High Pressure", *Phys. Rev. B.* **12**, 1172-1186, (1975).

WHITERS R.L., Thompson J.G, and Rae A.D., "The Crystal Chemistry Underlying Ferroelectricity in $Bi_4Ti_3O_{12}$, Bi_3TiNbO_9, and $BiWO_6$.", *J. Solid State Chem.* **94**, 404-417, (1991).

WYCKOFF R.W.G., "Crystal Structures", Vol. 1, 2nd edition, Interscience Publishers, (1963).

ZALLEN R., Unpublished Notes on the Optical Properties of Solids, (1962).

APPENDIX 1

Peaks Listing of the $SrBi_2Ta_2O_9$ Simulated X-ray Pattern

- Input/Output Xtalpow -

SBT Powder Pattern Generated by Xtalpow
(Newnham et al., 1973)

CELL PARAMETERS: 5.5040 5.4880 25.0600 90.000 90.000 90.000
ALTERNATE SETTING FOR SPACE GROUP #: 36

ATOM	X	Y	Z	OCCUPANCY	ISO(B)
Sr	.00000	.25700	.00000	1.000	1.500
Bi	.48000	.77200	.20200	1.000	1.500
Ta	.51600	.74700	.41440	1.000	1.500
O	.58200	.30900	.00000	1.000	1.000
O	.43700	.67600	.34340	1.000	1.000
O	.75800	.01700	.25200	1.000	1.000
O	.76300	.98800	.07170	1.000	1.000
O	.80400	.97900	.58470	1.000	1.000

X-RAY WAVELENGTH: 1.541838
BOUNDS ON TWO THETA: 10.0 70.0
LIMITS IMPOSED ON THE INDICES ARE: +/- 4 +/- 4 +/-18
MAX. ABS. INTENSITY / VOLUME ^{2} : 476.6552025

2-THETA	INTENSITY	D-SPACING	H	K	L
14.14	.38	6.2650	0	0	4
16.54	.16	5.3610	0	1	1
19.35	.84	4.5867	0	1	3
21.27	4.53	4.1767	0	0	6
23.16	5.45	3.8403	1	1	1
24.05	.33	3.7009	0	1	5
25.28	9.14	3.5236	1	1	3
28.49	5.33	3.1325	0	0	8
29.08	100.00	3.0712	1	1	5
29.80	.22	2.9984	0	1	7
32.54	17.87	2.7520	2	0	0
32.63	17.51	2.7440	0	2	0
33.33	1.24	2.6879	2	0	2
33.43	.23	2.6805	0	2	2
34.05	.59	2.6331	1	1	7
35.63	.07	2.5196	2	0	4
35.72	.02	2.5135	0	2	4
35.83	10.44	2.5060	0	0	10
36.17	.03	2.4831	0	1	9
36.59	.22	2.4557	1	2	0
36.71	.02	2.4483	2	1	1
37.31	.68	2.4099	1	2	2
38.14	.38	2.3598	2	1	3
39.20	.30	2.2980	2	0	6
39.29	.11	2.2933	0	2	6
39.41	.33	2.2864	1	2	4
39.83	3.25	2.2634	1	1	9
40.86	.20	2.2084	2	1	5
42.71	.03	2.1169	1	2	6
42.99	.00	2.1041	0	1	11
43.33	.50	2.0883	0	0	12
43.79	2.90	2.0675	2	0	8
43.86	2.67	2.0641	0	2	8
44.70	.09	2.0275	2	1	7
46.19	1.55	1.9654	1	1	11
46.75	16.99	1.9431	2	2	0
47.02	.22	1.9326	1	2	8
47.34	.88	1.9202	2	2	2

SBT Powder Pattern Generated by Xtalpow
(Newnham et al., 1973)

	Ctd				
49.09	.18	1.8559	2	2	4
49.17	8.55	1.8529	2	0	10
49.24	8.59	1.8504	0	2	10
49.44	.03	1.8436	2	1	9
49.99	.05	1.8245	0	3	1
50.16	.02	1.8188	0	1	13
51.02	1.39	1.7900	0	0	14
51.11	.55	1.7870	0	3	3
51.90	1.99	1.7618	2	2	6
52.15	.41	1.7540	1	2	10
52.73	.81	1.7358	3	1	1
52.87	.46	1.7318	1	3	1
53.03	6.72	1.7269	1	1	13
53.31	.20	1.7184	0	3	5
53.82	1.07	1.7034	3	1	3
53.95	.96	1.6996	1	3	3
54.93	.01	1.6715	2	1	11
55.21	.23	1.6636	2	0	12
55.28	.02	1.6618	0	2	12
55.66	2.68	1.6512	2	2	8
55.94	13.20	1.6438	3	1	5
56.06	13.12	1.6404	1	3	5
56.49	.26	1.6290	0	3	7
57.68	.05	1.5983	0	1	15
57.97	.33	1.5909	1	2	12
58.97	.05	1.5663	0	0	16
59.03	.92	1.5650	3	1	7
59.15	.12	1.5620	1	3	7
60.27	7.34	1.5356	2	2	10
60.30	5.33	1.5349	1	1	15
60.56	.02	1.5289	0	3	9
60.72	.06	1.5252	3	2	0
60.92	.09	1.5207	2	3	1
61.07	.02	1.5173	2	1	13
61.22	.14	1.5140	3	2	2
61.83	1.18	1.5005	2	0	14
61.89	1.17	1.4992	0	2	14
61.91	.40	1.4987	2	3	3
62.70	.02	1.4819	3	2	4
62.99	.76	1.4756	3	1	9
63.11	.53	1.4731	1	3	9
63.86	.26	1.4576	2	3	5
64.41	.02	1.4465	1	2	14
65.11	.01	1.4326	3	2	6
65.43	.01	1.4264	0	3	11
65.57	.02	1.4237	0	1	17
65.63	.74	1.4226	2	2	12
66.73	.32	1.4018	2	3	7
67.25	.93	1.3922	0	0	18
67.77	.55	1.3828	3	1	11
67.81	.01	1.3821	2	1	15
67.88	.43	1.3808	1	3	11
68.02	.10	1.3783	1	1	17
68.15	1.86	1.3760	4	0	0
68.37	1.98	1.3720	0	4	0
68.42	.10	1.3713	3	2	8

SBT Powder Pattern Generated by Xtalpow
(Newnham et al., 1973)
Ctd

68.61	.40	1.3678	4	0	2
68.84	.00	1.3638	0	4	2
68.99	.12	1.3612	2	0	16
69.05	.11	1.3603	0	2	16

==

XPOW version 2.0 Copyright 1993 Bob Downs and Kurt Bartelmehs
For reference, see Downs et al. (1993) American Mineralogist 78, 1104-1107.

APPENDIX 2

Peaks Listing of Rutile, Anatase, and Brookite

Simulated X-ray Patterns

- Input/Output Xtalpow -

Rutile Powder Pattern Generated by Xtalpow
(Wyckoff, 1963)

CELL PARAMETERS: 4.5924 4.5924 2.9575 90.000 90.000 90.000
SPACE GROUP: P4_2/mnm

ATOM	X	Y	Z	OCCUPANCY	ISO(B)
Ti	.00000	.00000	.00000	1.000	.800
O	.30499	.30499	.00000	1.000	1.000

X-RAY WAVELENGTH: 1.541838
BOUNDS ON TWO THETA: 10.0 70.0
LIMITS IMPOSED ON THE INDICES ARE: +/- 3 +/- 3 +/- 2
MAX. ABS. INTENSITY / VOLUME ² : 46.49360921

2-THETA	INTENSITY	D-SPACING	H	K	L
27.47	100.00	3.2473	1	1	0
36.12	44.98	2.4865	1	0	1
39.23	6.73	2.2962	2	0	0
41.29	17.79	2.1866	1	1	1
44.09	6.32	2.0538	2	1	0
54.39	52.65	1.6869	2	1	1
56.69	15.50	1.6237	2	2	0
62.84	7.16	1.4788	0	0	2
64.13	7.39	1.4522	3	1	0
65.59	.52	1.4233	2	2	1
69.09	17.69	1.3595	3	0	1
69.90	8.76	1.3458	1	1	2

==

XPOW version 2.0 Copyright 1993 Bob Downs and Kurt Bartelmehs
For reference, see Downs et al. (1993) American Mineralogist 78, 1104-1107.

Anatase Powder Pattern Generated by Xtalpow
(Wyckoff, 1963)

CELL PARAMETERS: 3.7873 3.7873 9.5147 90.000 90.000 90.000
SPACE GROUP #: 141

ATOM	X	Y	Z	OCCUPANCY	ISO(B)
Ti	.00000	.00000	.00000	1.000	.800
O	.00000	.00000	.20660	1.000	1.000

X-RAY WAVELENGTH: 1.541838
BOUNDS ON TWO THETA: 10.0 70.0
LIMITS IMPOSED ON THE INDICES ARE: +/- 2 +/- 2 +/- 7
MAX. ABS. INTENSITY / VOLUME ² : 59.36045253

2-THETA	INTENSITY	D-SPACING	H	K	L
25.31	100.00	3.5188	1	0	1
36.97	5.77	2.4316	1	0	3
37.82	18.94	2.3787	0	0	4
38.58	7.10	2.3337	1	1	2
48.05	26.72	1.8937	2	0	0
53.92	16.93	1.7004	1	0	5
55.07	16.58	1.6675	2	1	1
62.13	2.60	1.4940	2	1	3
62.71	12.17	1.4815	2	0	4
68.80	5.77	1.3645	1	1	6

==

XPOW version 2.0 Copyright 1993 Bob Downs and Kurt Bartelmehs
For reference, see Downs et al. (1993) American Mineralogist 78, 1104-1107.

Brookite Powder Pattern Generated by Xtalpow
(Wyckoff, 1963)

CELL PARAMETERS: 9.1840 5.4470 5.1450 90.000 90.000 90.000
SPACE GROUP #: 61

ATOM	X	Y	Z	OCCUPANCY	ISO(B)
Ti	.12900	.09720	-.13710	1.000	.800
O	.01010	.14860	.18240	1.000	1.000
O	.23040	.11300	-.46290	1.000	1.000

X-RAY WAVELENGTH: 1.541838
BOUNDS ON TWO THETA: .0 70.0
LIMITS IMPOSED ON THE INDICES ARE: +/- 6 +/- 4 +/- 3
MAX. ABS. INTENSITY / VOLUME ^{2} : 20.66247195

2-THETA	INTENSITY	D-SPACING	H	K	L
19.33	.40	4.5920	2	0	0
25.37	100.00	3.5109	2	1	0
25.72	77.62	3.4640	1	1	1
30.83	97.22	2.9000	2	1	1
32.89	4.59	2.7235	0	2	0
34.88	.22	2.5725	0	0	2
36.26	23.86	2.4772	1	0	2
37.36	17.71	2.4071	0	2	1
37.98	7.41	2.3690	3	1	1
38.43	1.85	2.3425	2	2	0
38.67	2.09	2.3284	1	2	1
39.24	4.21	2.2960	4	0	0
39.98	3.61	2.2549	1	1	2
40.18	14.94	2.2443	2	0	2
42.40	15.44	2.1319	2	2	1
42.74	.41	2.1157	4	1	0
43.62	.34	2.0751	2	1	2
46.09	19.97	1.9695	3	0	2
46.40	1.28	1.9567	4	1	1
48.09	32.24	1.8922	3	2	1
48.69	.08	1.8701	0	2	2
49.19	20.20	1.8521	3	1	2
49.76	2.97	1.8325	1	2	2
52.10	3.62	1.7554	4	2	0
52.86	.02	1.7320	2	2	2
53.49	.85	1.7130	4	0	2
54.33	22.51	1.6885	2	3	0
54.52	1.90	1.6832	1	3	1
55.29	31.89	1.6614	4	2	1
55.76	5.62	1.6487	5	1	1
56.30	.48	1.6341	4	1	2
57.20	15.50	1.6105	1	1	3
57.44	1.01	1.6043	2	3	1
57.77	2.10	1.5959	3	2	2
60.04	6.48	1.5410	2	1	3
60.48	.30	1.5307	6	0	0
62.09	11.61	1.4949	5	0	2
62.11	.04	1.4943	3	3	1
63.09	1.50	1.4736	6	1	0
63.53	7.65	1.4644	1	3	2
63.73	10.48	1.4602	5	2	1
64.18	6.48	1.4512	0	2	3

Brookite Powder Pattern Generated by Xtalpow
(Wyckoff, 1963)
Ctd

64.24	.43	1.4500	4	2	2
64.60	4.00	1.4428	3	1	3
64.66	6.85	1.4416	5	1	2
65.07	13.95	1.4335	1	2	3
65.55	.36	1.4242	4	3	0
65.94	8.27	1.4166	6	1	1
66.21	.21	1.4116	2	3	2
67.71	.27	1.3838	2	2	3
68.34	.16	1.3726	4	3	1
68.96	6.86	1.3618	0	4	0

==

XPOW version 2.0 Copyright 1993 Bob Downs and Kurt Bartelmehs
For reference, see Downs et al. (1993) American Mineralogist 78, 1104-1107.

VITA

Born in Besançon, France in August 1972, Mona P. Moret received her first degree (DUT, Diplôme Universitaire Technologique) in Electrical Engineering at the University of Franche Comté in Belfort, France in June 1992. A motivating training period at the company Turbomeca, encouraged her to pursue her studies in applied physics. She received a B.Sc Honours, First Class, in Applied Physics from the University of Portsmouth, England in July 1994. She then enrolled at Virginia Tech, USA to pursue graduate studies. She received her Master's degree in Applied Physics from the Physics Department in July 1996.

M. Moret